



Title	Density-matrix renormalization group study of quantum spin systems with Kitaev-type anisotropic interaction(Dissertation_全文)
Author(s)	Shinjo, Kazuya
Citation	Kyoto University (京都大学)
Issue Date	2016-03-23
URL	https://doi.org/10.14989/doctor.k19479
Right	学位規則第9条第2項により要約公開; 許諾条件により要旨は2016-05-01に公開; 許諾条件により本文は2017-05-01に公開 (2017/05/16全文ファイル追加)
Type	Thesis or Dissertation
Textversion	ETD

Density-matirx renormalization group study of
quantum spin systems with Kitaev-type
anisotropic interaction

Kazuya Shinjo

January 26, 2016

Abstract

The proposal of the Kitaev model and its candidate material Na_2IrO_3 have brought a new playground of quantum spin systems. In this thesis, we theoretically study the effect of the Kitaev-type anisotropic interaction on quantum spin systems by using the unbiased numerical method, density-matirx renormalization group (DMRG) method. Especially, we focus on Na_2IrO_3 with the honeycomb-lattice structure and $\text{Ba}_3\text{IrTi}_2\text{O}_9$ with the triangular-lattice structure. The spin exchange interaction of these materials is dominated by the Kitaev interaction due to the strong spin-orbit interaction in the $5d$ compounds. Thus, these two materials give a strong motivation for the study on quantum spin systems with the Kitaev-type anisotropic interaction. We make clear the effect of the Kitaev interaction on quantum spin systems that is expected to lead to non-trivial phases.

We investigate the extended Kitaev-Heisenberg (KH) model as an effective spin model for Na_2IrO_3 that takes into account the Ir-Ir direct electron hoppings and the trigonal distortion present in Na_2IrO_3 . The KH model is too simple to explain the zigzag antiferromagnetic (AFM) order that has been observed in experiments. We find that the extended KH model naturally explains the zigzag AFM order. In order to obtain the zigzag AFM order, the off-diagonal spin exchange interaction due to the trigonal distortion plays an important role. Other than the zigzag AFM phase, we also find the 120° AFM, FM, and two kinds of incommensurate phases next to the spin-liquid phase.

We further investigate the KH model on the triangular lattice that is expected to describe the physics of $\text{Ba}_3\text{IrTi}_2\text{O}_9$. There is geometrical spin frustration due to the triangular lattice structure. Thus, the model is no longer solvable even at the Kitaev limit point, leading to the high non-trivial quantum phase diagram. By performing DMRG, we find the 120° AFM phase, \mathbb{Z}_2 -vortex crystal phase, dual \mathbb{Z}_2 -vortex crystal phase, nematic phase, \mathbb{Z}_6 FM phase, and its dual phase, which is consistent with the previous studies. Instead of a spin-liquid phase, we find the nematic phase around the AFM Kitaev limit point. The ground-state phase diagrams of the KH models on the honeycomb and

triangular lattices are completely different.

In addition, we examine the entanglement entropy and entanglement spectrum of these models. Although the two quantities do not necessarily show anomaly or jumps at phase boundaries in general, the KH model on the triangular lattice shows the change at the boundaries. In contrast to the triangular lattice, the change of the entanglement entropy and entanglement spectrum of the extended KH model on the honeycomb lattice is obscure. However, we find that phase transitions between the Kitaev spin-liquid state and magnetically ordered states are well characterized by the entanglement spectrum due to its degenerate structure related to the exact-solvability of the Kitaev model.

The results obtained in this thesis show that the effect of the Kitaev interaction emerges in various non-trivial phases in quantum spin systems. This implies that our study on the Kitaev physics opens up a new field in quantum spin systems. Furthermore, our study contributes to the understanding of the physics of the materials with strong spin-orbit interaction, since the quantum spin systems with the Kitaev anisotropic interaction are expected to be relevant to iridate-oxide materials such as Na_2IrO_3 and $\text{Ba}_3\text{IrTi}_2\text{O}_9$.

Acknowledgement

I would like to express my sincerest gratitude to Prof. Takami Tohyama for his guidance, useful discussions and enormous comments during the course of my Ph. D. study.

I am grateful to Dr. Shigetoshi Sota for his collaborations, encouragements, and helpful support for my calculation, and Prof. Seiji Yunoki for his collaborations, kind support, and useful discussions during my stay in RIKEN for two years. I am also grateful to Prof. Keisuke Totsuka for his collaborations, useful discussion and comments.

It is great pleasure to thank Dr. Tsuyoshi Okubo, Dr. Youhei Yamaji, Prof. Naoki Kawashima, and Prof. Masatoshi Imada for their collaborations and useful discussions. I have been happy to share interests in physics with them.

I am thankful to Prof. Ippei Danshita, Prof. Kenji Harada, Prof. Takafumi Suzuki, Prof. Synje Todo, Prof. Ryotaro Arita, Dr. Satoshi Morita, Dr. Ryo Igarashi, Dr. Tatsuya Sakashita, Dr. Takahiro Ohgoe, Dr. Zhao Huihai, and Dr. Tomonori Shirakawa. The discussion with them have been very useful for my study and enjoyable.

My thanks also go to all the members of the laboratory in Yukawa Institute for Theoretical Physics (YITP) and in RIKEN.

I was financially supported from RIKEN as a Junior Research Associate (JRA), and thank to RIKEN for giving me an opportunity to stay at RIKEN. Numerical calculation was partly carried out at the K computer, the RIKEN Advanced Institute for Computational Science, and the supercomputer Center, Institute for Solid State Physics, University of Tokyo.

Lastly, I would like to express the deepest appreciation to my parents, Kazushi and Mariko, for their kind support to my studying physics.

Publication List

This thesis is based on the following original papers.

- “Density-matrix renormalization group study of the extended Kitaev-Heisenberg model” : Chapter 4
Kazuya Shinjo, Shigetoshi Sota, and Takami Tohyama, Phys. Rev. B **91**, 054401 (2015).

submitted manuscript:

- “Density-matrix renormalization group study of Kitaev-Heisenberg model on the triangular lattice” : Chapter 5
Kazuya Shinjo, Shigetoshi Sota, Seiji Yunoki, Keisuke Totsuka, and Takami Tohyama, ArXiv e-prints (2015), arXiv:1512.02334 [cond-mat.str-el].

Contents

1	Introduction	12
1.1	Background	13
1.2	Purpose of this thesis	17
1.3	Organization of this thesis	17
2	Kitaev-Heisenberg Model	20
2.1	Heisenberg model	20
2.1.1	Quantum antiferromagnet	21
2.1.2	Spin frustration and spin liquid	22
2.2	Kitaev model	26
2.2.1	Majorana fermion representation	26
2.2.2	Quadratic Hamiltonian	28
2.2.3	Diagonalization in momentum space	29
2.3	Kitaev-Heisenberg model on honeycomb lattice and its extension	31
2.3.1	Spin-orbital entangled $j = 1/2$ Mott insulator	31
2.3.2	Kitaev-Heisenberg model	32
2.3.3	Atomic limit	33
2.3.4	Hopping processes	33
2.3.5	Experiments on honeycomb-lattice compounds (Na_2IrO_3 , Li_2IrO_3 , and RuCl_3)	38
2.4	Kitaev-Heisenberg model on the triangular lattice	41
2.4.1	Kitaev-Heisenberg model on the triangular lattice	41
2.4.2	Experiments of $\text{Ba}_3\text{IrTi}_2\text{O}_9$	42
3	Numerical method: density-matrix renormalization group (DMRG)	45
3.1	Density-matrix renormalization group (DMRG)	46
3.2	Algorithm of DMRG	48
3.2.1	Infinite system algorithm	48
3.2.2	Finite system algorithm	50

CONTENTS

3.3	Entanglement study in quantum spin systems	51
3.3.1	Entanglement entropy	53
3.3.2	Entanglement entropy in gapped systems	54
3.3.3	Entanglement entropy in gapless systems	55
3.3.4	Entanglement spectrum	55
4	The extended Kitaev-Heisenberg model on the honeycomb lattice	58
4.1	Model and Method	59
4.2	Results and Discussions	60
4.2.1	Phase diagram around spin liquid	60
4.2.2	Physical properties in each phase	62
4.3	Summary and Outlook	68
5	The Kitaev-Heisenberg model on the triangular lattice	71
5.1	Model and Method	72
5.2	Results and Discussions	73
5.2.1	Phase diagram	73
5.2.2	Spin structure factors	75
5.2.3	Entanglement entropy and entanglement spectrum . . .	82
5.3	Summary and Outlook	85
6	Conclusions	88
A	Entanglement Spectrum	92

Chapter 1

Introduction

In this thesis, we discuss the Kitaev-Heisenberg (KH) models on the honeycomb and triangular lattices. The Kitaev model has been originally proposed as the model whose ground states are two kinds of exactly-solvable spin liquid [1]. The Kitaev model is defined on the honeycomb lattice with no geometrical frustration, but the Kitaev-type interaction introduces a new kind of spin frustration breaking $SU(2)$ spin-rotational symmetry. Interestingly, it has been suggested that some iridate materials can be a candidate material for the Kitaev model. In this thesis, we discuss two of such iridate materials: Na_2IrO_3 with honeycomb-lattice structure and $\text{Ba}_3\text{IrTi}_2\text{O}_9$ with triangular-lattice structure.

An effective model suggested for Na_2IrO_3 is the KH model on honeycomb lattice, which is the most simplified effective spin model for Na_2IrO_3 [2–4]. Na_2IrO_3 cannot be described by the pure Kitaev model, but the Heisenberg interaction is needed. The phase diagram of the KH model has already been established [5–11]. However, it has been pointed out that the additional Heisenberg interaction is not enough to describe Na_2IrO_3 , because zigzag antiferromagnetic (AFM) order observed in experiments is not naturally explained by considering the KH model [12, 13]. Therefore, it has been further discussed what kind of effective spin model is appropriate. It has been suggested that further neighbor interactions [13–17] and/or some anisotropic interactions [18–24] should be introduced. However, these interactions did not lead to a final version of an effective model for Na_2IrO_3 .

Recently, more realistic effective spin models have been derived considering the real electronic structure of Na_2IrO_3 [18]. In the models, there are a lot of frustrated spin interactions, thereby the quantum phase diagram is highly non-trivial. Therefore, it is interesting to analyze these models with unbiased quantum mechanical methods. For this purpose, density-matrix renormaliza-

tion group (DMRG) method that can calculate the ground state of large system size with high accuracy is a good method [25].

Furthermore, it has been suggested that the KH model is defined on other lattices such as the triangular lattice [2, 26]. Especially, a candidate material for the KH model on the triangular lattice $\text{Ba}_3\text{IrTi}_2\text{O}_9$ has been proposed. Therefore, the KH model on lattices other than the honeycomb lattice is not necessarily a toy model. Experimentally, a spin-liquid behavior is observed in $\text{Ba}_3\text{IrTi}_2\text{O}_9$, but the physics behind the observation has not yet well known. It is thus interesting to investigate the property of the KH model on the triangular lattice [27–30]. Since the model has the Kitaev-type spin frustration in addition to geometrical frustration due to triangular lattice, the ground state is highly non-trivial. Because of the geometrical frustration, the Kitaev model on the triangular lattice cannot be exactly solved in contrast to the case of the honeycomb lattice. Therefore, we have to resort to numerical calculation such as exact diagonalization and DMRG. We apply DMRG method to the model and investigate its ground-state properties quantum mechanically.

Interestingly, the KH model on the honeycomb lattice and triangular lattice show completely different ground-state phase diagram. At the Kitaev limit points, the KH model on the honeycomb lattice shows a spin-liquid state that is exactly-known, but the KH model on the triangular lattice shows a nematic phase (at AFM Kitaev point) that is not well characterized. Although there is a previous study that suggests a spin-liquid state at the AFM Kitaev limit point on the triangular lattice [31], our DMRG calculation does not show a spin-liquid state, but a nematic phase, which is one of the major differences between the KH models on the honeycomb and triangular lattices. In addition, we find some interesting phases of the (extended) KH model on the honeycomb and triangular lattices, which will be discussed in this thesis.

In this chapter, we introduce the background needed to understand quantum spin systems with Kitaev-type anisotropic interaction. The purpose of this thesis is given at the end of this chapter.

1.1 Background

The AFM Heisenberg model is one of typical models that describe Mott insulators in strongly correlated electron systems. However, the ground states of the Heisenberg model show various kinds of phases, because there are various lattice structures, anisotropic interactions, and further neighbor interactions. Especially, the ground states can be non-trivial when the system stays away

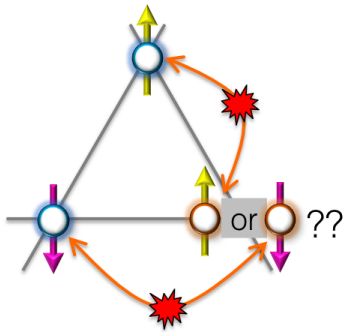


Figure 1.1: Geometrical spin frustration of three spins on a triangular lattice. Yellow and pink arrows show spin of a localized electron. All three spins cannot align antiparallel to their neighbors, so these spins are “frustrated”, preventing from magnetic ordering.

from classical limit with strong quantum fluctuation due to small value of spin S , e.g., $S = 1/2$, low dimensionality, and geometrical spin frustration [32].

Since quantum fluctuation that is strong in low-dimensional systems makes classical ground states unstable, the $S = 1/2$ AFM Heisenberg model in one dimension shows a spin-liquid (Tomonaga-Luttinger-liquid) state [33, 34]. Another example of typical quantum state is a valence-bond solid (VBS) state. For example, if next-nearest neighbor interactions are introduced in spin $S = 1/2$ chain, the ground state changes to the VBS state (or called dimer state) that shows no magnetic order but breaks translational symmetry [35–37]. In general, there is no AFM long-range order in one dimension, since it is impossible to break a continuum symmetry in one-dimensional systems even at zero temperature [38]. Although one-dimensional spin systems are far away from the classical limit, there are powerful approaches such as Bethe’s exact solutions [39], conformal field theory [40], and density-matrix renormalization group (DMRG) that can treat one-dimensional systems with large system size and with high accuracy.

In two-dimensional systems, the ground state of $S = 1/2$ AFM Heisenberg model on square lattice exhibits a Néel state, which is classical, since quantum fluctuations are weaker in two-dimensional case than in one-dimensional case. However, there is a way to destroy such long-range order, for example, by introducing a geometrical spin frustration that exists in the triangular lattice and the Kagomé lattice. As shown in Fig. 1.1, all three spins on a triangular antiferromagnet cannot align antiparallel to their neighbors. Once two of the three spins align antiparallel, the other spin is “frustrated”, because its possible orientations, up and down, give the same energy. Further neighbor interactions

also introduce spin frustration. Such spin frustration puts the system away from the classical limit, and a lot of states compete each other, resulting in highly non-trivial ground states. The ground states can be various kinds of magnetic ordered states and VBS states. When the system is put enough far away from the classical limit, the ground state can be a spin-liquid state that shows neither magnetic order nor broken translational symmetry. By P. W. Anderson, a concept of spin liquid in two-dimensional triangular lattice was proposed as resonating valence bond (RVB) state that is composed of a superposition of various configurations of valence bonds [41], although it has been known now that its ground state is not a spin liquid state but a 120° AFM magnetically ordered state [43, 44]. Motivated by this, some spin liquid states have been proposed theoretically and experimentally on other lattices. For example, the ground state of the Kagomé lattice has been suggested as spin liquid both theoretically and experimentally, although there is a controversy [43, 45–51].

When a geometrical spin frustration exists, quantum Monte Carlo method widely used in condensed matter theory is no longer applicable because of the sign problem. Mean field analysis can give some hints for spin liquids, for example, by using a projective symmetry group analysis [52], but cannot prove the existence of spin liquid. In such a situation, DMRG is able to give great contribution to investigating spin liquids.

Spin-liquid states cannot be characterized by local order parameters related to broken symmetry. This means that spin liquids stay beyond Landau’s symmetry breaking theory that classifies phases by using symmetry breaking [53–55]. The new type of phases is called quantum order. Quantum Hall liquid with topological order is an example of quantum order [52]. As the quantum order is characterized by long-range entanglement, local order parameters are no longer useful to characterize it. Instead, we have to rely on ground-state degeneracy, fractional quasi-particle statistics, and entanglement detecting non-local correlations. Especially, entanglement entropy and its spectrum have been used to detect non-local topological nature. It is easy to calculate them by using numerical calculation such as exact diagonalization and DMRG. The entanglement entropy and spectrum are closely related to the reduced density matrix calculated by DMRG, so that DMRG can play an important role in calculating them. Examining the relationship between DMRG and entanglement has lead to new approaches to many-body quantum system, such as the projected entangled pair states (PEPS) [56–58] and the multi-scale entanglement renormalization ansatz (MERA) [59]. DMRG takes advantage of calculating entanglement spectrum, which is difficult for other

methods.

The Kitaev model on the honeycomb lattice is one of the examples that gives an exactly-solved spin liquid in two dimension [1]. The model is important in the sense that the realization of spin-liquid state is very limited. For the realization, the model introduces a new kind of spin frustration with Kitaev-type anisotropic interaction breaking spin $SU(2)$ rotational symmetry. In the gapped phase of the Kitaev model, Abelian anyon excitation emerges. If time-reversal symmetry is broken in the gapless phase, non-Abelian anyon excitation appears in the phase. By using the non-Abelian anyon, scalable topological computation has been suggested [60, 61]. The Kitaev model is thus closely related to quantum information theory.

Na_2IrO_3 is one of the candidate materials for realizing the Kitaev model on the honeycomb lattice. However, it has been proposed that the Heisenberg interaction in addition to the Kitaev interaction is necessitated [4]. The model with the Kitaev and Heisenberg interactions is the KH model. The phase diagram of the model has been studied, and a FM phase, stripe AFM phase, zigzag AFM phase, and the Kitaev spin-liquid phase have been found [4, 5, 9]. Experimentally, it has been observed that the ground state of Na_2IrO_3 is not a spin-liquid state, but a zigzag AFM ordered state [12, 13]. The zigzag AFM phase appears from the antiferromagnetic Kitaev coupling in the KH model, but the Kitaev coupling in Na_2IrO_3 is expected to be ferromagnetic. Therefore, the zigzag AFM order is not naturally explained by the KH model. This problem has inspired the further investigations of the effective spin model for Na_2IrO_3 . Some groups have suggested effective spin models with further neighbor interactions and/or new anisotropic interactions [6–11, 13–24]. They have discussed the relation between the ground state phase diagram of these models and the ground state of Na_2IrO_3 .

In addition to the honeycomb lattice, it has been proposed that the KH model is defined on other lattices such as on the triangular lattice [26]. The model is no longer exactly solved even at the Kitaev limit because of the geometrical spin frustration present in triangular lattice. Some interesting magnetic ordered states such as a nematic state and incommensurate state with the \mathbb{Z}_2 vortices have been proposed [28, 29, 108]. Moreover, a candidate material for the KH model on triangular lattice $\text{Ba}_3\text{IrTi}_2\text{O}_9$ has been suggested [27, 29, 30], since a spin-liquid behavior has been observed in experiments [27].

1.2 Purpose of this thesis

The purpose of this thesis is to reveal the role of the Kitaev-type anisotropic interactions in quantum spin systems. This is closely related to a clear understanding of the physics of iridate materials. We focus on Na_2IrO_3 and $\text{Ba}_3\text{IrTi}_2\text{O}_9$. The physics of both these materials is dominated by the Kitaev interaction. However, different lattice structures lead to completely different physics, even if the Hamiltonian is the same. Since the models with the Kitaev-type anisotropic interactions introduce complicated spin interactions, a DMRG treatment is very effective. By calculating energy, spin-spin correlation functions, we can investigate quantum spin systems with the Kitaev-type anisotropic interactions. Furthermore, we can discuss entanglement properties of these systems, especially entanglement spectrum that is easily calculated by DMRG.

1.3 Organization of this thesis

This thesis is organized as follows. The KH model is introduced in Chap. 2. The Kitaev model and Na_2IrO_3 as a candidate material for it are briefly reviewed. The KH model was considered as an effective spin model for Na_2IrO_3 , but it could not explain a zigzag AFM order present in Na_2IrO_3 . Thus, we discuss the extension of the KH model for Na_2IrO_3 with additional anisotropic off-diagonal interactions. Taking into account the trigonal distortion present in Na_2IrO_3 is then important. In addition to the honeycomb lattice, the KH model on the triangular lattice is introduced. We review experimental observations in $\text{Ba}_3\text{IrTi}_2\text{O}_9$ that has recently proposed as being described by the KH model on the triangular lattice.

In Chap. 3, we explain the numerical method used in this thesis: density-matrix renormalization group (DMRG). The development of DMRG is closely related to quantum informational study. Quantum entanglement has recently introduced in condensed matter physics to characterize phases with non-local quantum order. Entanglement entropy and entanglement spectrum easily calculated based on DMRG are introduced in this chapter.

In Chap. 4 and Chap. 5, we show our calculation results by the DMRG study of the quantum spin systems with the Kitaev-type anisotropic interactions. In Chap. 4, we show the honeycomb lattice case. We focus on the extended KH model on the honeycomb lattice. The model contains the effect of real electronic structures with a trigonal distortion in Na_2IrO_3 . We determine the phase diagram around the Kitaev spin liquid by examining the ground-

state energy, spin-spin correlation functions, and entanglement entropy. Then, entanglement spectrum in each phase is discussed.

In Chap. 5, we show our results of the triangular lattice case. We focus on the KH model on the triangular lattice. The full-quantum phase diagram for the entire parameter space, and spin structure factors are shown. As in Chap. 4, the energy profile, entanglement entropy, and entanglement spectrum of the model are shown.

Finally, our conclusions are given in Chap. 6.

Chapter 2

Kitaev-Heisenberg Model

In this chapter, we first briefly review the Kitaev model on the honeycomb lattice realizing the Kitaev spin liquids [1]. The Kitaev model is exactly solvable. A candidate material for the Kitaev model, Na_2IrO_3 , was suggested, but it has turned out that Na_2IrO_3 cannot be described by the Kitaev model [12, 13]. The basic prototype of the effective spin model for Na_2IrO_3 is the KH model on the honeycomb lattice [2–4]. However, the KH model is too simple to describe Na_2IrO_3 . Possible effective spin models beyond the KH model should be sought for.

The KH model is not only defined on the honeycomb lattice, but also defined on triangular lattice. The phase diagram of the model on the triangular lattice is much different from that on the honeycomb lattice. Furthermore, $\text{Ba}_3\text{IrTi}_2\text{O}_9$ has been suggested to be a candidate material for the KH model on the triangular lattice [27, 29, 30]. The KH model on the triangular lattice and Ba_3IrO_3 will be introduced.

We start from introducing the Heisenberg model, which is the most basic model for describing magnetism in Mott insulators. One of the most exotic states realized in the model is a spin-liquid state, which will be briefly introduced. After introducing the Heisenberg model, we will consider the Kitaev model and the KH models on the honeycomb and triangular lattices and the corresponding candidate materials.

2.1 Heisenberg model

The Heisenberg model is one of the most basic models in quantum spin systems. When quantum fluctuations are strong because of small spin S , low-dimensionality d , and spin frustration, the ground state of the AFM Heisenberg model shows non triviality and a variety of phases. In this thesis, we mainly

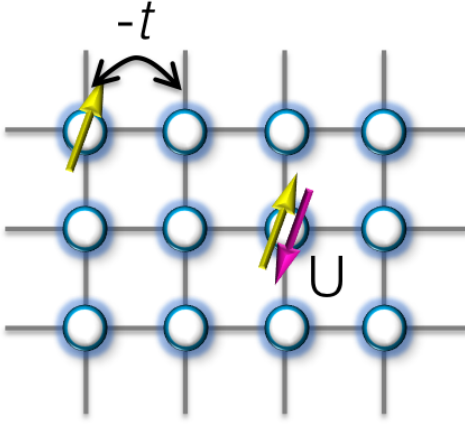


Figure 2.1: The kinetic term $-t$ and potential term U . The yellow and red arrows show electrons on the lattice with up and down spins.

consider $S = 1/2$, $d = 2$ cases, where spin frustration can give rise to a spin-liquid states. These are interesting since spin liquid cannot be described by the Landau's symmetry breaking theory that is useful in characterizing most of the conventional phases in condensed matter physics.

2.1.1 Quantum antiferromagnet

We start with the Hubbard model

$$\mathcal{H} = -t \sum_{\langle l,m \rangle, \sigma} \left(c_{l,\sigma}^\dagger c_{m,\sigma} + c_{m,\sigma}^\dagger c_{l,\sigma} \right) + U \sum_l n_{l\uparrow} n_{l\downarrow}, \quad (2.1)$$

where the creation operator $c_{l\sigma}^\dagger$ creates an electron with spin $\sigma = \uparrow, \downarrow$ at site l . t term denotes electron hopping and U the Coulomb repulsion.

The Hubbard model describes electrons interacting each other only on each site. If we consider a system at half-filling and strong coupling limit $U/t \rightarrow \infty$, the Hubbard model is reduced to the antiferromagnetic Heisenberg model by the second-order perturbation theory given by

$$\mathcal{H} = J \sum_{\langle lm \rangle} \mathbf{S}_l \cdot \mathbf{S}_m, \quad (2.2)$$

where \mathbf{S} is a spin operator at site l .

We first introduce the ground state of AFM Heisenberg Hamiltonian in one

dimension

$$\mathcal{H} = \sum_l^L J \mathbf{S}_l \cdot \mathbf{S}_{l+1} \quad (2.3)$$

$$= \sum_l \frac{J}{2} (S_l^+ S_{l+1}^- + S_l^- S_{l+1}^+) + JS_l^z S_{l+1}^z. \quad (2.4)$$

In the classical limit, we expect that the ground state is the Néel state written by

$$|\text{N\'eel}\rangle = |\uparrow\rangle_1 |\downarrow\rangle_2 \cdots |\uparrow\rangle_{L-1} |\downarrow\rangle_L, \quad (2.5)$$

where L is the number of lattice site. The Néel state is a solution of a mean-field theory. On the other hand, the Bethe's exact solution of the AFM Heisenberg chain has shown that the ground state is not the Néel state [62].

The ground state wave function of the Heisenberg model can be understood as a linear superposition of spin singlets $\frac{1}{\sqrt{2}} (|\uparrow\downarrow\rangle - |\downarrow\uparrow\rangle)$ in one dimension. In fact, the energy per site is $E = -\frac{J}{4} \times \frac{z}{2}$ for the Néel state, and $E = -\frac{3}{8}J = -0.375J$ for spin-singlet dimer state (valence bond solid state), where z is the number of nearest neighbor sites ($z = 2, 4, 6$ for one, two, and three-dimensional hyper cubic lattices, respectively). A schematic view of the valence bond solid state on the honeycomb lattice is shown in Fig 2.2. Furthermore, we can make the energy lower if we make quantum spin liquid state, which is constructed by the superposition of spin singlet dimer. The energy per site is then $E = -(\ln 2 - \frac{1}{4})J = -0.443J$ [39,62]. The spin liquid state breaks neither spin $SU(2)$ rotational symmetry nor translational symmetry. The excitation of the spin-liquid state is considered as fractional excitation with $S = \frac{1}{2}$ called spinon [63]. Due to the strong correlation, the spinons are coupled to emergent gauge field.

The Néel state can be destroyed by quantum fluctuations due to small spin, low-dimensionality, and spin frustration. P. W. Anderson extended the notion of the spin liquid to higher dimensions, introducing the resonance valence bond (RVB) state on the triangular lattice as shown in Fig 2.3, which is one of the candidates of spin liquid [41]. The RVB state has attracted much attention because it is regarded as the playground of high- T_c superconductivity [42].

2.1.2 Spin frustration and spin liquid

Spin-liquid states do not appear usually in $d \geq 2$ systems, since quantum fluctuations are not strong enough in $d \geq 2$. Therefore, spin frustration

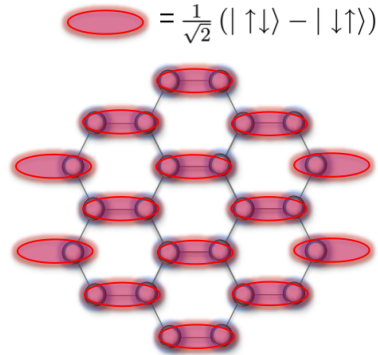


Figure 2.2: Schematic view of singlet pairs (red ellipses) called dimers on the honeycomb lattice. The dimer covers the lattice in the VBS phase.

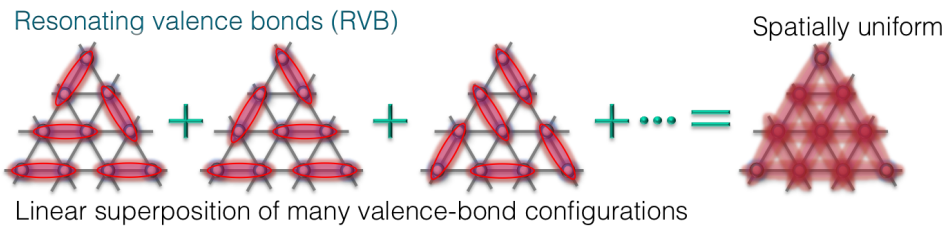


Figure 2.3: Resonating valence bond (RVB) state represented as a superposition of valence bond states with various dimer coverings. The RVB state shows neither magnetic order nor lattice symmetry breaking.

is needed to introduce strong quantum fluctuation realizing spin liquid. A schematic explanation of the spin frustration is given in Fig. 1.1. A candidate of frustration-induced spin-liquid state is firstly suggested on a triangular AFM Heisenberg model by considering the RVB state (see Fig. 2.3). However, it has turned out that the true ground state is not a spin-liquid state, but a magnetically ordered state with 120° AFM order [43, 44]. In general, it is not easy to obtain spin-liquid states from a local microscopic Hamiltonian like the Heisenberg model. It has been pointed out that a spin-liquid state is realized if the four-site ring exchange interactions due to the fourth-order perturbation theory are introduced [64–67]. It is not only theoretically but also experimentally interesting to study such a quantum spin system on triangular lattice. There are candidate materials for the spin system on triangular lattice: organic materials κ -(BEDT-TTF)₂Cu₂(CN)₃ and EtMe₃Sb[Pd(dmit)₂]₂. These materials do not show magnetic long-range ordering down to ~ 20 mK regardless of strong exchange coupling ~ 250 K [68, 69]. It has been reported that κ -(BEDT-TTF)₂Cu₂(CN)₃ has a small energy gap [70, 71]. On the other

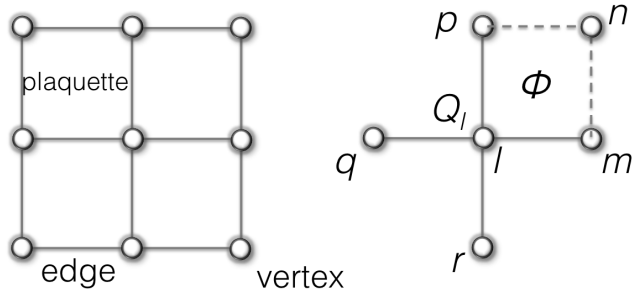


Figure 2.4: The definition of edge, vertex, plaquette, and site indices on the square lattice.

hand, the experiment of $\text{EtMe}_3\text{Sb}[\text{Pd}(\text{dmit})_2]_2$ shows that the spin susceptibility goes to constant, and the specific heat shows a linear T behavior. As both behaviors are characteristic of a metal with a Fermi surface, the experimental data imply that the emergent spinon is fermionic with Fermi surface although the charge degrees of freedom remain frozen [72, 73]. However, the properties of these materials are controversial since these experiments are so complicated.

Although the spin liquid is not characterized by local order parameter, it has been considered that the spin liquid is not only one-type. Several kinds of spin liquids have been suggested: the RVB state [41], the $U(1)$ quantum spin liquid with spinon fermi surface [74, 75], which are gapless spin liquids while chiral spin liquid [76–79], and the short-range RVB state [80, 81], which are gapful spin liquids. The spin liquids are classified by the symmetry group of their gauge structure. In the Landau’s theory, symmetry and its breaking can characterize various phases, phase transitions, and gapless excitations determining low energy physics. However, the spin liquids do not show any breaking of symmetry and are thus beyond the Landau’s theory of symmetry-breaking. Therefore, we need another characterization of the spin liquids.

The spinons in the spin liquid are considered as quasiparticles with fractional quantum number, and are described by the lattice gauge theory that was originally studied as a model of confinement of quarks with fractional quantum number [82–85]. For example, the \mathbb{Z}_2 gauge field theory that is the simplest topological field theory is important for understanding the physical properties of the quantum spin-liquid states. The \mathbb{Z}_2 gauge field is described by

$$\mathcal{H} = -g \sum_{\text{edge}} \sigma_{lm}^x - \frac{1}{g} \sum_{\text{plaquettes}} \sigma_{lm}^z \sigma_{mn}^z \sigma_{np}^z \sigma_{pl}^z, \quad (2.6)$$

where σ^x and σ^z are Pauli matrices [86]. The \mathbb{Z}_2 electric charge $Q_l = \sigma_{lm}^x \sigma_{lp}^x \sigma_{lq}^x \sigma_{lr}^x$

is defined on star at a vertex. Since $[Q_l, \mathcal{H}] = 0$, Q_l is a constant of motion, and classifies the ground state. There are confinement and deconfinement phases in $d = 2$. The confinement phase is at strong gauge coupling region $g \gg 1$, and deconfinement phase is at weak region $g \ll 1$. In the deconfinement phase, the \mathbb{Z}_2 gauge theory is relevant to quantum spin liquids on Kagomé lattices [87–90]. When mean-field solution ansatzs are assumed, gauge fluctuations are gapped out and the spinons are gapped, which is the \mathbb{Z}_2 -gapped spin liquid, corresponding to the short-ranged RVB state. As we will mention below, the gapped- \mathbb{Z}_2 spin liquid corresponds to the gapped Kitaev spin liquid. If other mean-field solution ansatzs are assumed, the \mathbb{Z}_2 -gapless spin liquid can be realized in the same way. The gapless- \mathbb{Z}_2 spin liquid corresponds to the gapless Kitaev spin liquid. The spin liquid has massless Dirac fermions with a small Fermi surface, coupled to the \mathbb{Z}_2 gauge field. As there are no gapless gauge bosons, the gauge fluctuations can only mediate short-range interactions between spinons.

So far, we reviewed the \mathbb{Z}_2 gauge theories as a language of the \mathbb{Z}_2 spin liquids. In addition to the \mathbb{Z}_2 spin liquids, there are various kinds of spin liquids such as the $U(1)$ spin liquids and chiral spin liquids although spin liquids cannot be characterized and classified by Landau’s symmetry breaking theory. The Kitaev spin liquids are two of these various kinds of spin liquids. Spin liquids are not characterized by local order parameters, but by non-local correlations originated in gauge fluctuations. For characterizing spin liquids, projective symmetry group (PSG) that is an extension of a symmetry group is suggested for classifying the mean-field states [52].

However, we cannot know which spin liquid is closer to the ground state of a given Hamiltonian from mean field theories. We, therefore, have to rely on recent advances in density-matrix renormalization group (DMRG), tensor network techniques such as projected entangled pair states (PEPS), and multi-scale entanglement renormalization ansatz (MERA), which have recently made great contributions to our understanding of the stability of spin liquids for a given Hamiltonian.

When the first term of the Hamiltonian of the \mathbb{Z}_2 gauge field is replaced by the sum of vertex terms, the toric code model is obtained [91]

$$\mathcal{H} = -\lambda_v \sum_{\text{stars}} \sigma_{lm}^x \sigma_{lp}^x \sigma_{lq}^x \sigma_{lr}^x - \lambda_p \sum_{\text{plaquettes}} \sigma_{lm}^z \sigma_{mn}^z \sigma_{np}^z \sigma_{pl}^z, \quad (2.7)$$

where λ_v is the coupling constant of the star operator defined on vertex, and λ_p is the coupling constant of the plaquette operator defined on plaquette. The

ground state of the model is the state of the deconfined phase of the \mathbb{Z}_2 gauge theory. This model is a special case of the Kitaev model on the honeycomb lattice, which we will introduce in the next section.

2.2 Kitaev model

The Hamiltonian of the Kitaev model on the honeycomb lattice is given by [1]

$$\mathcal{H} = \sum_{\gamma} \sum_{\langle lm \rangle} \mathcal{H}_{lm}^{\gamma}, \quad (2.8a)$$

$$\mathcal{H}_{lm}^{\gamma} = -J_{\gamma} S_l^{\gamma} S_m^{\gamma} \quad (2.8b)$$

$$= \begin{cases} -J_x S_l^x S_m^x & (\text{on } J_x \text{ bond}) \\ -J_y S_l^y S_m^y & (\text{on } J_y \text{ bond}) \\ -J_z S_l^z S_m^z & (\text{on } J_z \text{ bond}). \end{cases} \quad (2.8c)$$

The interactions in the Kitaev model are shown in Fig 2.5, where there is spin frustration breaking spin rotational symmetry. The model is exactly solved by writing spin operators in terms of Majorana fermions and thus the properties of the ground state are exactly known. The interactions between nearest neighbors are of $S^x S^x$, $S^y S^y$ or $S^z S^z$ type, depending on bond-direction on the honeycomb lattice. The ground state of isotropic Kitaev model is known as a gapless Kitaev spin-liquid state characterized by gapless Majorana fermion excitations with two Dirac cones [92]. The spin-spin correlation of the gapless Kitaev spin-liquid is short-range, showing non-zero value only for the nearest-neighbor sites [93]. In this section, we introduce the way of solving the model based on Kitaev's procedure and the properties of Kitaev spin liquids.

2.2.1 Majorana fermion representation

By representing the spin operators with Majorana fermions as shown in Fig. 2.6, the Kitaev Hamiltonian can be written in quadratic form of Hamiltonian, which can then directly diagonalized. Following Kitaev's solution, the spin operators can now be written in terms of Majorana fermions.

First of all, we assume that every sites on the honeycomb lattice have two fermions labeled by '1' and '2'. Then, the creation and annihilation operators of these two fermions are c_1^\dagger , c_2^\dagger , c_1 , and c_2 . These operators have four-dimensional Fock space written by $|n_1, n_2\rangle = |0, 0\rangle$, $|0, 1\rangle$, $|1, 0\rangle$, and $|1, 1\rangle$, where n_1 and

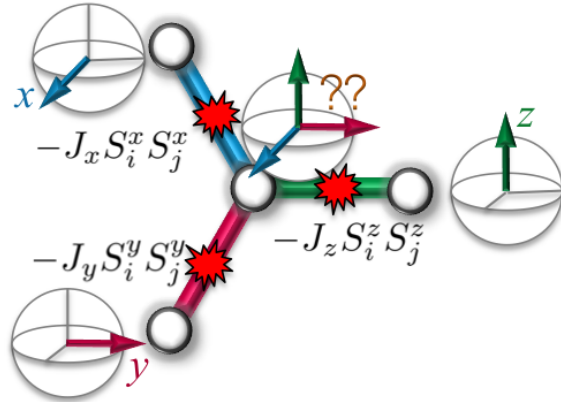


Figure 2.5: Schematic view of spin frustration breaking spin rotational symmetry in the Kitaev model

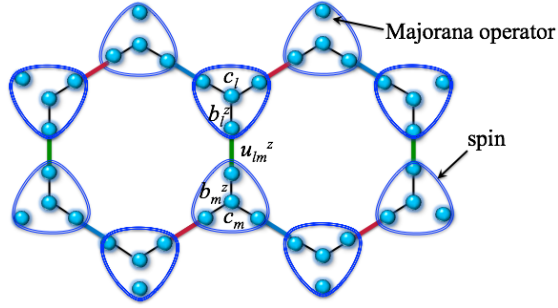


Figure 2.6: Spins on the honeycomb lattice and Majorana Fermions. Spin operator is represented by the Majorana operators.

n_2 show the occupation number of fermion ‘1’ and ‘2’, respectively. Next, we make these fermion operators by using four Majorana fermions

$$c = c_1 + c_1^\dagger, \quad (2.9)$$

$$b^x = \frac{1}{i}(c_1 - c_1^\dagger), \quad (2.10)$$

$$b^y = (c_2 + c_2^\dagger), \quad (2.11)$$

$$b^z = \frac{1}{i}(c_2 - c_2^\dagger). \quad (2.12)$$

The operators $(\gamma_1, \gamma_2, \gamma_3, \gamma_4) = (b_x, b_y, b_z, c)$ satisfy the following relations.

$$\{\gamma_l, \gamma_m\} = \gamma_l \gamma_m + \gamma_m \gamma_l = \delta_{lm}, \quad (2.13)$$

$$\gamma_l = \gamma_l^\dagger. \quad (2.14)$$

Spin-1/2 operators are expressed in terms of the Majorana fermion opera-

tors:

$$\sigma_l^\gamma = i b_l^\gamma c_l, \quad (2.15)$$

where b_l^γ and c_l are Majorana operators. However, these σ_l^γ do not satisfy the Pauli spin algebra. There is a redundancy in the fermionic encoding of the spins. Each spin-1/2 particle has a two-dimensional Hilbert space, but the Majorana operators have a four-dimensional Hilbert space. The condition $\sigma_l^x \sigma_l^y \sigma_l^z = i$ corresponds to the condition $b_l^x b_l^y b_l^z c_l = (2c_1^\dagger c_1 - 1)(2c_2^\dagger c_2 - 1) = 1$ in fermionic language. Then, by imposing the condition $D = 1$, we can eliminate unphysical states with $D = -1$ for $|0, 1\rangle$ and $|1, 0\rangle$, where $D = b^x b^y b^z c$.

2.2.2 Quadratic Hamiltonian

The Kitaev Hamiltonian in the Majorana fermion language is as follows:

$$\mathcal{H} = J_x \sum_{x-link} (ib_l^x b_m^x)(ic_l c_m) + J_y \sum_{y-link} (ib_l^y b_m^y)(ic_l c_m) + J_z \sum_{z-link} (ib_l^z b_m^z)(ic_l c_m). \quad (2.16)$$

While above Hamiltonian is quartic, operators in the parenthesis of each term $u_{lm}^\gamma = (ib_l^\gamma b_m^\gamma)$ commute with the Hamiltonian and commute among themselves. This fact reduces the Hamiltonian to quadratic form in Majorana fermions. The u_{lm}^γ satisfies

$$u_{lm}^\gamma = -u_{ml}^\gamma, \quad (2.17)$$

$$(u_{lm}^\gamma)^2 = 1, \quad (2.18)$$

$$(u_{lm}^\gamma)^\dagger = u_{lm}^\gamma, \quad (2.19)$$

and its eigenvalues take value ± 1 . The Hamiltonian describes tight binding Majorana fermions whose hopping interactions correspond to the \mathbb{Z}_2 gauge fields u_{lm}^γ on each bonds.

In addition, the plaquette operators,

$$\hat{W}_p = \sigma_1^y \sigma_2^z \sigma_3^x \sigma_4^y \sigma_5^z \sigma_6^x = \prod_{l,m,\gamma \in \text{plaquette}} u_{lm}^\gamma, \quad (2.20)$$

are defined on each plaquette. They satisfy

$$\hat{W}_p^2 = 1, \quad (2.21)$$

$$[\hat{W}_p, \hat{W}_{p'}] = 0, \quad (2.22)$$

$$[\mathcal{H}, \hat{W}_p] = 0, \quad (2.23)$$

and have eigenvalue of ± 1 . The gauge-invariant plaquette operators \hat{W}_p can be identified with the Wilson loop operators. The eigenvalue $W_p = -1$ means that a π -flux vortex is living on plaquette p .

The Hamiltonian is classified by the distribution of u_{lm}^γ and can be diagonalized for each sector. The minimum energy distribution is obtained by the vortex-free condition $W_p = +1$ for each plaquette and this is obtained by fixing $u_{lm}^\gamma = +1$ for every links. For the vortex-free state, the Hamiltonian is easily diagonalized to obtain the ground state in the extended space $|\psi\rangle_{ex}$. By projecting out unphysical states with $D = -1$, the ground state belonging to the physical subspace $|\psi\rangle$ is given by

$$|\psi\rangle = \hat{P}|\psi\rangle_{ex}, \quad (2.24)$$

where

$$\hat{P} = \prod_l \frac{1+D_l}{2}. \quad (2.25)$$

2.2.3 Diagonalization in momentum space

Taking the uniform vortex-free configuration of $W_p = +1$ that contains the global minimum of energy by choosing $u_{lm}^\gamma = +1$, the Hamiltonian is written as

$$\mathcal{H} = J_x \sum_{x-link} i c_l c_m + J_y \sum_{y-link} i c_l c_m + J_z \sum_{z-link} i c_l c_m. \quad (2.26)$$

The transformation of the Majorana fermion operators are

$$c_{l,m} = \sum_k \frac{1}{\sqrt{(2N)}} e^{i\mathbf{k}\cdot\mathbf{r}_l} c_k^{l,m}, \quad (2.27)$$

where N is the total number of the unit cells. On the honeycomb lattice, as a unit cell has two sites labeled by l and m , there are two Majorana modes c_k^l

and c_k^m . By using these modes, the Hamiltonian in momentum space reads

$$\mathcal{H} = \sum_k \begin{pmatrix} (c_k^l)^\dagger & (c_k^m)^\dagger \end{pmatrix} \begin{pmatrix} 0 & if_k^* \\ -if_k & 0 \end{pmatrix} \begin{pmatrix} c_k^m \\ c_k^l \end{pmatrix}, \quad (2.28)$$

where

$$f_k = 2(J_z + J_x e^{-i\mathbf{k}\cdot\mathbf{a}_1} + J_y e^{-i\mathbf{k}\cdot\mathbf{a}_2}). \quad (2.29)$$

Primitive vectors are $\mathbf{a}_1 = \left(\frac{1}{2}, \frac{\sqrt{3}}{2}\right)$ and $\mathbf{a}_2 = \left(-\frac{1}{2}, \frac{\sqrt{3}}{2}\right)$. It is easy to diagonalize the Hamiltonian in momentum space as follows,

$$\begin{pmatrix} c_k^l \\ c_k^m \end{pmatrix} = \frac{1}{2} \begin{pmatrix} v_k & -v_k \\ 1 & 1 \end{pmatrix} \begin{pmatrix} \alpha_k \\ \beta_k \end{pmatrix} \quad (2.30)$$

with $v_k = if_k^*/|f_k|$. The diagonalized Hamiltonian is

$$\mathcal{H} = \sum_k |f_k| \left(\alpha_k^\dagger \alpha_k - \beta_k^\dagger \beta_k \right). \quad (2.31)$$

By filling all negative energy states with quasi particles β_k , the ground state with energy $E_k = |f_k|$ is given by

$$|\psi\rangle = \prod_k \beta_k^\dagger |0\rangle, \quad (2.32)$$

where $|0\rangle$ is vacuum satisfying $\alpha_k|0\rangle = \beta_k|0\rangle = 0$. The equation,

$$f_k = 0, \quad (2.33)$$

has two solutions if and only if

$$|J_x| \leq |J_y| + |J_z|, \quad (2.34)$$

$$|J_y| \leq |J_x| + |J_z|, \quad (2.35)$$

$$|J_z| \leq |J_x| + |J_y| \quad (2.36)$$

are satisfied. The low energy excitations are gapless Majorana fermions with linear dispersions. This phase is known as Kitaev's B phase. When the above inequalities are not satisfied, the ground state has an energy gap between the two bands whose dispersion is parabolic. This phase is known as Kitaev's A phase. In the limit of $J_z \gg J_x, J_y$, the Hamiltonian is effectively the same as the toric code Hamiltonian [1,91]. The ground state of Kitaev's A phase is the

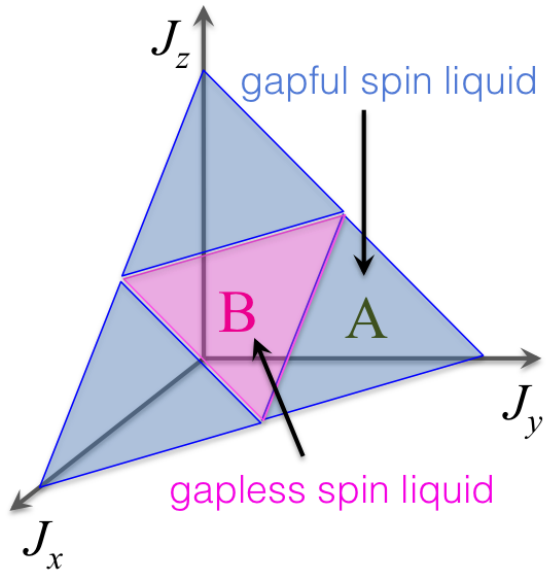


Figure 2.7: Phase diagram of the Kitaev model.

gapped- \mathbb{Z}_2 spin liquid, and that of B phase is the gapless- \mathbb{Z}_2 spin liquid. Spin-spin correlation function is short-range and vanishes beyond nearest neighbor [93]. Dimer-dimer correlation function shows power law behavior in the gapless phase, but decays exponentially in the gapful phase [94]. To summarize, the ground-state phase diagram is shown in Fig. 2.7

2.3 Kitaev-Heisenberg model on honeycomb lattice and its extension

The KH model with both the Kitaev interaction Eq. (2.8a) and the Heisenberg interaction Eq. (2.2) is a proto-type spin model for an iridium-oxide dom-pund Na_2IrO_3 . However, there has been a problem that the zigzag AFM order observed in Na_2IrO_3 cannot be explained by the KH model. In this section, we briefly review the KH model and possible extensions of the model.

2.3.1 Spin-orbital entangled $j = 1/2$ Mott insulator

The typical Ir valence Ir^{4+} has a $5d^5$ configuration. The IrO_6 octahedral crystal field splits these orbitals into e_g and t_{2g} as shown in Fig. 2.8. Then, the strong spin-orbit coupling of Ir simplifies the situation. The spin-orbit coupling further lifts the degeneracy of t_{2g} into $j = 1/2$ and $j = 3/2$. The

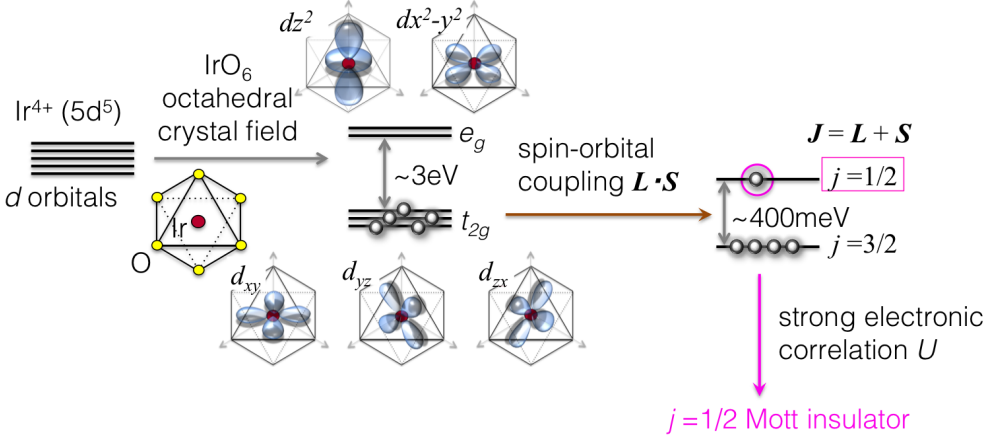


Figure 2.8: Spin-orbital entangled $j = 1/2$ Mott insulator in Na_2IrO_3 .

$j = 3/2$ states are fully occupied and $j = 1/2$ states are half filled. When strong electron correlation is considered, the effective physics is described by the spin-orbital entangled $j = 1/2$ Mott insulator [95].

2.3.2 Kitaev-Heisenberg model

The Mott insulator with orbital degrees of freedom in Na_2IrO_3 has been discussed by Jackeli and Khaliullin [3]. They have shown that the Kitaev interaction can be a relevant interaction in Mott insulators with strong spin-orbit coupling. There are two kinds of common cases of Ir-O-Ir bond geometries: (a) 180° bond and (b) 90° bond. Electrons hop along these Ir-O-Ir bond geometries, and exchange interactions coming from hopping along the 180° bond are simple and yield mainly Heisenberg-type interactions. By considering the honeycomb structure of Na_2IrO_3 , Chaloupka *et.al.* have considered possible exchange processes relevant to the effective Hamiltonian and projected them onto the lowest Kramers doublet. Then, they proposed the KH model as an effective spin model [4]

$$\mathcal{H} = \sum_{\Gamma} \sum_{\langle lm \rangle \in \Gamma} J_K S_l^{\gamma} S_m^{\gamma} + J_H \left(S_l^{\alpha} S_m^{\alpha} + S_l^{\beta} S_m^{\beta} + S_l^{\gamma} S_m^{\gamma} \right) \quad (2.37)$$

$$= \sum_{\Gamma} \sum_{\langle lm \rangle \in \Gamma} J_K S_l^{\gamma} S_m^{\gamma} + J_H \mathbf{S}_l \cdot \mathbf{S}_m, \quad (2.38)$$

where Γ represents a combination of $(\alpha, \beta, \gamma) = (x, y, z), (z, x, y)$, and (y, z, x) on the J_z , J_y , and J_x bond shown in Fig. 2.9, respectively. The second summation is taken over all possible bonds $\langle lm \rangle$ belonging to Γ . The ground state of the model has already been studied in detail by using exact diagonalization

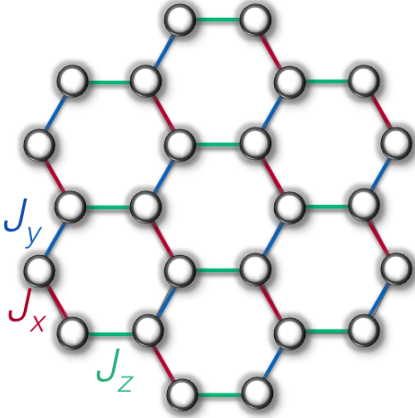


Figure 2.9: The honeycomb lattice with the Kitaev interaction. $S^x S^x$, $S^y S^y$, and $S^z S^z$ interactions are indicated by red, blue, and green lines, respectively.

and DMRG methods [4, 5].

2.3.3 Atomic limit

Calculating exchange interactions coming from electron hopping along the 90° bond is complicated, because many hopping pathways, for example, a direct overlap between d orbitals in addition to oxygen mediated hopping, are allowed. Actually, such a direct overlap introduces off-diagonal exchange interactions into the conventional Kitaev-Heisenberg model, which are essential for Na_2IrO_3 .

We introduce an effective spin model for Na_2IrO_3 different from the KH model based on the discussion given by Rau *et. al.* [19, 20] and Yamaji *et. al.* [18]. We start with atomic limit described by

$$\mathcal{H}_0 = \sum_i \left[\frac{U - 3J_H}{2} (N_i - 5)^2 - 2J_H S_i^2 - \frac{J_H}{2} L_i^2 \right], \quad (2.39)$$

where N_i is the total number operator at site i , S_i is spin operator at site i , L_i is orbital angular momentum operator at site i , U is the Coulomb interaction, and J_H is Hund's coupling. Here, the situation $U, J_H \gg \lambda \gg t$ is assumed, where λ is spin-orbit coupling and t is hopping energy.

2.3.4 Hopping processes

Two kinds of hopping processes between t_{2g} orbitals (d_{xy} , d_{yz} , and d_{zx}) exist. For example, let us consider hoppings along z -bond that lead to a dominant $S^z S^z$ interaction. The hoppings along the remaining bonds are also

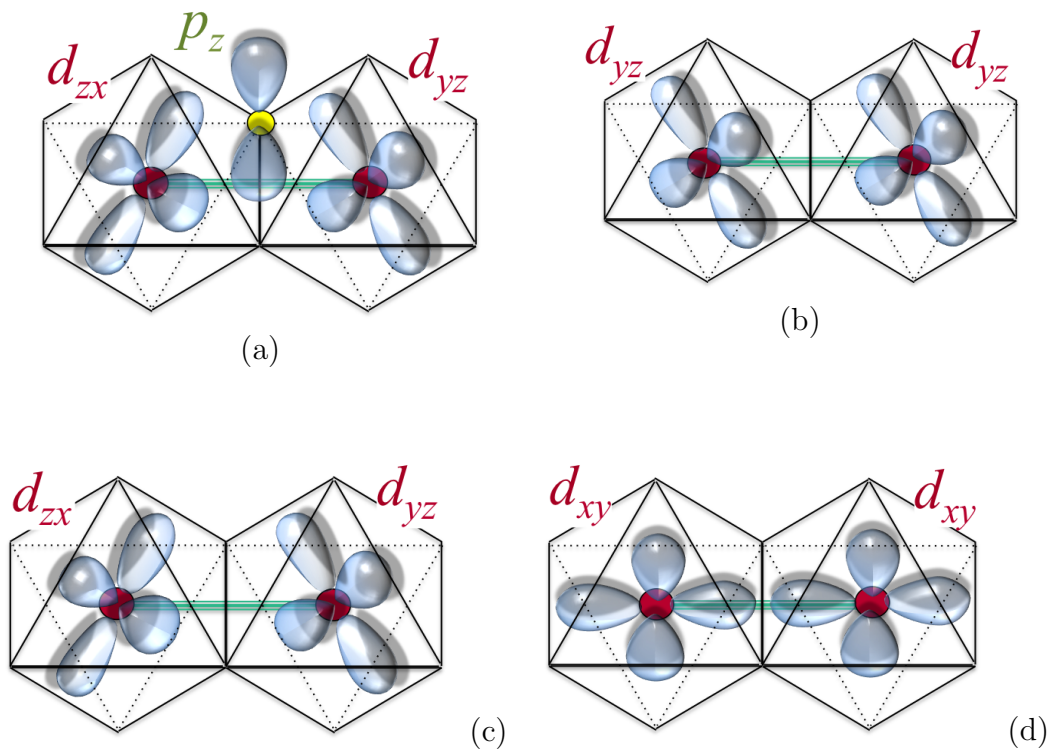


Figure 2.10: The relevant electron hopping process in Na_2IrO_3 . The hopping process along z -bond is shown. (a) The oxygen-mediated Ir-O-Ir hopping that contributes to t_2 . (b) The intra-orbital direct Ir-Ir hopping that contributes to t_1 . (c) The inter-orbital direct Ir-Ir hopping that contribute to t_2 . (d) The intra-orbital direct Ir-Ir hopping that contributes to t_3 .

considered in the same way by permuting x , y , and z cyclically. We define the annihilation operator of t_{2g} electrons at site i as follows.

$$\mathbf{d}_l = \begin{pmatrix} d_{l,yz} \\ d_{l,zx} \\ d_{l,xy} \end{pmatrix} \quad (2.40)$$

Then, the kinetic part of the Hamiltonian on z -bond is

$$\mathcal{H}_{\text{kinetic}} = \sum_{\langle lm \rangle} \mathbf{d}_i^\dagger \hat{t}_z \mathbf{d}_j \quad (2.41)$$

$$\hat{t}_z = \begin{pmatrix} t_1 & t_2 & t_4 \\ t_2 & t_1 & t_4 \\ t_4 & t_4 & t_3 \end{pmatrix}. \quad (2.42)$$

The origin of each component of the hopping matrix \hat{t}_z is explained below. The diagonal part of the hopping matrix shows intra-orbital hopping, and the off-diagonal part shows inter-orbital hopping. The possible orbital overlap contributing to the hopping t_1 , t_2 , and t_3 is shown in Fig. 2.10. The remaining t_4 is a contribution from the trigonal distortion known to be present in Na_2IrO_3 . Fig. 2.10 (a) shows oxygen-mediated d - p - d hopping process, while Fig. 2.10 (b), 2.10 (c), and 2.10 (d) show the direct d - d hoppings. The oxygen mediated hopping shown is given by the overlap of d_{yz} orbital on site i , p_z orbital on oxygen, and d_{zx} orbital on site j . This hopping process is the origin of the inter-orbital contribution to t_2 . The direct orbital overlaps of Fig. 2.10 (b) and 2.10 (d) are between the same orbitals, and contribute to the diagonal parts t_1 and t_3 , respectively. The direct overlap of Fig. 2.10 (c) is between different orbitals and contributes to the off-diagonal part t_2 .

Considering the kinetic Hamiltonian as a perturbation to \mathcal{H}_0 with the basis of $j = 1/2$ states, the nearest-neighbor effective spin Hamiltonian on z -bond is derived by Rau and Kee as follow [20].

$$\hat{\mathcal{H}} = \sum_{\Gamma} \sum_{\langle lm \rangle \in \Gamma} \hat{\mathcal{H}}_{lm} \quad (2.43)$$

$$\begin{aligned} \hat{\mathcal{H}}_{lm} = & KS_l^\gamma S_m^\gamma + J \left(S_l^\alpha S_m^\alpha + S_l^\beta S_m^\beta \right) \\ & + I_1 \left(S_l^\alpha S_m^\beta + S_l^\beta S_m^\alpha \right) \\ & + I_2 \left(S_l^\alpha S_m^\gamma + S_l^\gamma S_m^\alpha + S_l^\beta S_m^\gamma + S_l^\gamma S_m^\beta \right), \end{aligned} \quad (2.44)$$

where

$$J = \frac{4}{27} \left[\frac{6t_1(t_1 + 2t_3) - 9t_4^2}{U - 3J_H} + \frac{9t_4^2 + 2(t_1 - t_3)^2}{U - J_H} + \frac{(2t_1 + t_3)^2}{U + 2J_H} \right. \\ \left. + \sqrt{2} \left(\frac{3\{t_2(4t_3 - 5t_4) + (7t_1 + t_3 - 4t_4)t_4\}}{3J_H - U} \right. \right. \\ \left. \left. + \frac{4t_2(4t_1 - t_3) + t_4(11t_1 + 13t_3) + 3t_4(4t_4 + 5t_2)}{J_H - U} \right. \right. \\ \left. \left. - \frac{4(2t_1 + t_3)(t_2 + 2t_4)}{2J_H + U} \right) \theta \right] \quad (2.45)$$

$$K = \frac{8J_H}{9} \left[\frac{(t_1 - t_3)^2 - 3(t_2^2 - t_4^2)}{(U - 3J_H)(U - J_H)} + \frac{\sqrt{2}\{3(t_2 - t_4)t_4 + (t_3 - t_1)(2t_2 + t_4)\}}{(U - 3J_H)(U - J_H)} \theta \right] \quad (2.46)$$

$$I_1 = \frac{8J_H}{9} \left[\frac{3t_4^2 + 2t_2(t_1 - t_3)}{(U - 3J_H)(U - J_H)} \right. \\ \left. - \frac{\sqrt{2}\{(t_2^2 + (t_1 - t_3)^2 + (t_1 - 3t_2 - t_3)t_4 + 5t_4^2)\}}{(U - 3J_H)(U - J_H)} \theta \right] \quad (2.47)$$

$$I_2 = -\frac{8J_H}{9} \left[\frac{t_4(t_1 - t_3 - 3t_2)}{(U - 3J_H)(U - J_H)} \right. \\ \left. - \frac{\sqrt{2}\{2t_1(t_2 + t_3) - t_1^2 - (t_2 + t_3)^2 + (3t_2 + t_3 - t_1)t_4 - 4(t_2^2 + t_4^2)\}}{2(U - 3J_H)(U - J_H)} \theta \right]. \quad (2.48)$$

Here, the trigonal distortion is treated to be small, and expanded to the first order of θ . The I_2 term represents the contribution from trigonal distortion. The off-diagonal coupling $I_2 < 0$ for trigonal compression, and $I_2 > 0$ for trigonal expansion. By considering the microscopic origins, $K < 0$ and $I_1 > 0$ are expected. When $J_H = 0$, $K = I_1 = I_2 = 0$, the Heisenberg model on the hexagonal lattice is realized. When the trigonal distortion is zero $t_4 = \theta = 0$, direct hopping other than the oxygen-mediated hopping is zero, i.e., $t_1 = t_3 = 0$, and J_H is finite. Then, $J = I_1 = I_2 = 0$ and $K < 0$, so that a ferromagnetic Kitaev model is realized, which is originally proposed by Jackeli and Khaliullin [3]. However, as t_1 , t_2 , t_3 , t_4 , and J_H are finite in Na_2IrO_3 . Thus, the usual KH model only with J and K is not an effective spin model for Na_2IrO_3 , even if ideal crystal structure with no trigonal distortion is assumed.

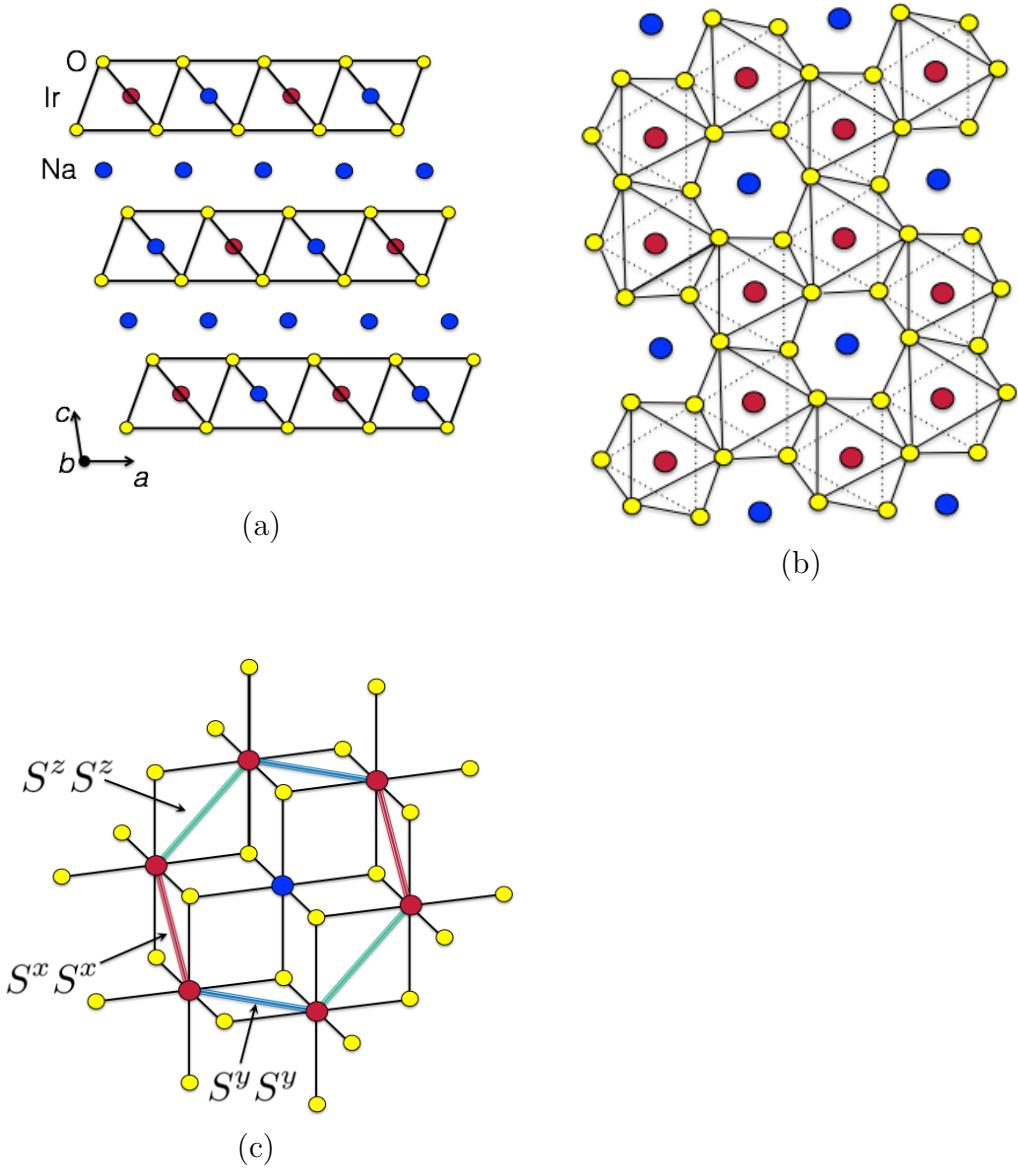


Figure 2.11: Crystal structure of Na_2IrO_3 . Red, yellow, and blue points show Ir , O , Na ions, respectively. (a) Na_2IrO_3 with well-separated layer. (b) IrO_6 cages constructing the honeycomb lattice in the layer. The IrO_6 shares its edge. (c) The dominant interaction in Na_2IrO_3 . The Kitaev interaction with $S^x S^x$, $S^y S^y$, and $S^z S^z$ interactions are indicated by red, blue, and green lines, respectively.

2.3.5 Experiments on honeycomb-lattice compounds (Na_2IrO_3 , Li_2IrO_3 , and RuCl_3)

The crystal structure of Na_2IrO_3 is shown in Fig. 2.11. The red, yellow, blue points indicate Ir, O, Na ions, respectively. Na_2IrO_3 is a layered material consisting of IrO_3 octahedra. These octahedra share their edges and constitute a honeycomb lattice. However, the honeycomb lattice is slightly anisotropic: 3.073\AA along b-axis, and 3.071\AA along the remaining four sides. There is a trigonal distortion in IrO_6 octahedra, which has a large effect on the ground state [12]. As the effective moment is $\mu_{\text{eff}} = 1.79\mu_B$, which is close to the value of the spin-1/2 moments $\mu_{\text{eff}} = g\sqrt{S(S+1)} = 1.73\mu_B$ [96], Na_2IrO_3 is considered to be a spin-1/2 Mott insulator with charge gap $\sim 340\text{meV}$ [97, 98]. In order to work out the spin structure, some experiments have been carried out: the X-ray scattering [99–101] and the neutron scattering experiments [12, 13]. It has been found that the ordered moment is aligned along the a-axis and the ground state is zigzag antiferromagnetic order [12, 13].

The inelastic neutron scattering data of Na_2IrO_3 at 4.6K and 55K are shown in Figs. 2.12 (a) and 2.12 (b), respectively. Fig. 2.12 shows the raw neutron scattering intensity as a function of wave vector $Q = |\mathbf{Q}|$. At 4.6K, an inelastic signal with a sinusoidal-like dispersive boundary below 5meV is clearly observed at low Q which is damped out in the paramagnetic phase at 55K (see Fig. 2.12 (c)) The dispersion boundary extrapolates at the lowest energies to $Q = 0.67\text{\AA}^{-1}$. Fig. 2.12 (d) and Fig. 2.12 (e) are the calculated scattering from spin waves of the Heisenberg model with up to third neighbor interactions $J_{1,2,3}$ with the zigzag AFM order and the stripy AFM order. Fig. 2.12 (f) is the calculated scattering from spin waves of the KH model with the stripy AFM phase. The calculation for the zigzag AFM order can give the observed dispersion at low Q , which is quite different from that for the stripy AFM order shown in Fig. 2.12 (e) and Fig. 2.12 (f).

In addition to Na_2IrO_3 , there are some materials with the honeycomb-lattice structure where the Kitaev-type anisotropic interaction is important. For example, it is considered that the physics of Li_2IrO_3 and RuCl_3 is dominated by the Kitaev interaction. Recent neutron scattering experiments of Li_2IrO_3 have shown a magnetic Bragg peak within the first-Brillouin zone, indicating an incommensurate spiral magnetic order [102]. If the low-energy physics of Li_2IrO_3 is described by the KH model (2.44), the incommensurate spiral magnetic order may correspond to the incommensurate phase in the phase diagram of the extended KH model in Fig. 5.2. In contrast to Na_2IrO_3 , however, it has been considered that the further neighbor interactions

are important in Li_2IrO_3 [17, 103].

Unlike Na_2IrO_3 and Li_2IrO_3 , a 4d-orbital honeycomb compound RuCl_3 has more ideal honeycomb-lattice structure and the AFM Kitaev coupling [104]. In spite of the weaker spin-orbit interaction than in the iridium-oxides, the significant Kitaev interaction appears in RuCl_3 due to electron correlations. While the Kitaev exchange interaction originates from the oxygen-mediated electron hopping in Na_2IrO_3 , such electron hopping paths are not relevant in RuCl_3 , but rather the direct overlap of the *d* orbitals is important. In contrast to Na_2IrO_3 , RuCl_3 has $j = 1/2$ and $3/2$ bands that are not well separated by spin-orbit coupling, but electron correlation opens a gap between them near the Fermi level, leading to the spin-orbital entangled Mott insulator. Although their microscopic nature is different, the zigzag AFM order is expected in both RuCl_3 and Na_2IrO_3 [104, 105].

The interactions relevant to Na_2IrO_3 , Li_2IrO_3 , and RuCl_3 are summarized in Table 2.1. The magnetic orders expected by theoretical and experimental studies are also summarized. The magnetic order in Li_2IrO_3 is basically explained by the KH model with further neighbor interactions with the ferromagnetic Kitaev interaction. The model lead to the incommensurate spiral magnetic order [17] that is consistent with experimental observation [102]. The zigzag AFM order in RuCl_3 is basically stabilized within the KH model with the AFM Kitaev interaction, although the off-diagonal interaction and small long-range interactions are present in RuCl_3 [104, 105]. However, the KH model (with further neighbor interactions) with the ferromagnetic Kitaev interaction cannot explain the zigzag AFM order in Na_2IrO_3 . Thus, in order to explain the zigzag AFM order in Na_2IrO_3 , it is essential to extend the KH model by adding the anisotropic off-diagonal interactions of both I_1 and I_2 terms in Eq. (2.44), which is due to the trigonal distortion present in Na_2IrO_3 [18, 20].

There are experiments investigating the effect of non-magnetic dilution in Na_2IrO_3 and Li_2IrO_3 . The spin-glass behavior has been observed in the diluted compounds, $\text{Na}_2(\text{Ir}_{1-x}\text{Ti}_x)\text{O}_3$ and $\text{Li}_2(\text{Ir}_{1-x}\text{Ti}_x)\text{O}_3$ [106]. The triangular-lattice structure becomes similar to the honeycomb-lattice structure if the system is disordered. Thus, the substitution experiments are interesting in the light of the relation between the Kitaev physics on the honeycomb lattice and that on the triangular lattice.

Table 2.1: Interactions and magnetic order in Na_2IrO_3 , Li_2IrO_3 , and RuCl_3 . F (AF) denotes ferromagnetic (antiferromagnetic) Kitaev interactions. “✓” (–) indicates that the corresponding term (long-range interaction(LRI) and off-diagonal interaction (ODI)) is important in the compound. Magnetic orders expected by theory and experiment are shown by “theory” and “experiment”. The “zigzag” and “IC” indicate that the magnetic order is the zigzag AFM order and the incommensurate spiral order.

compound	Kitaev interaction	LRI	ODI	theory	experiment
Na_2IrO_3	F	–	✓	zigzag	zigzag
Li_2IrO_3	F	✓	✓	IC	IC
RuCl_3	AF	–	✓	zigzag	zigzag

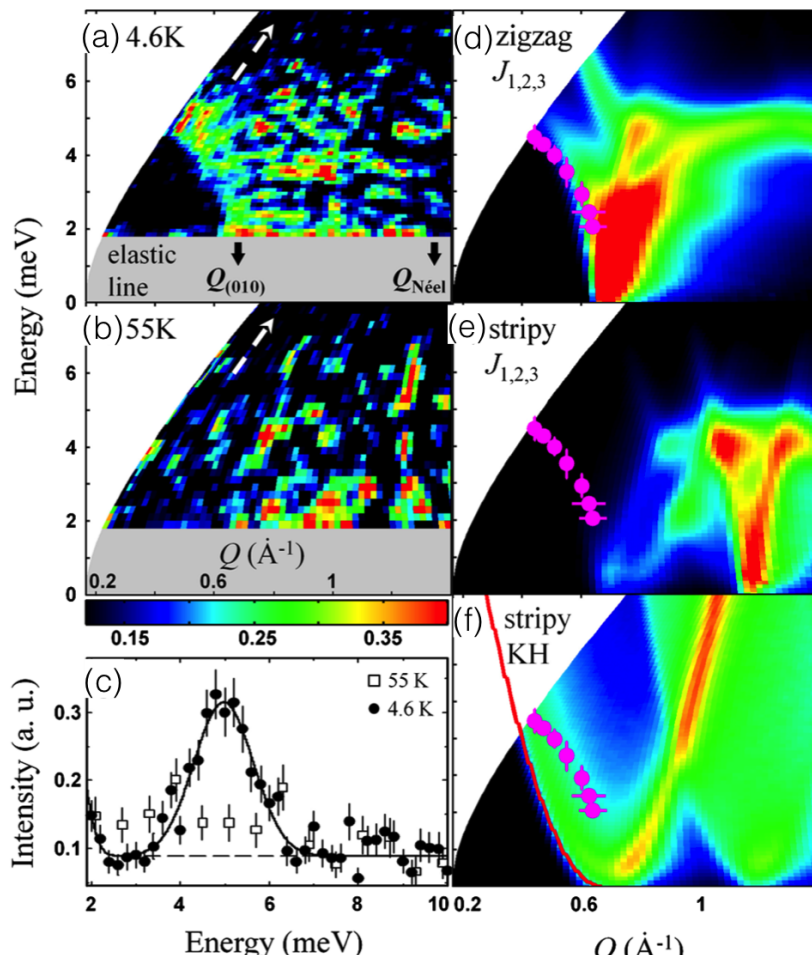


Figure 2.12: (a) Powder neutron scattering data at 4.6K in a zigzag AFM phase. The notable feature is the sharp lower boundary of the scattering at low wave number. (b) Powder neutron scattering data at 55K in a paramagnetic phase. Gray shading shows the inaccessible region close to the elastic line dominated by incoherent elastic scattering. (c) Energy scan along the slanted thick dashed arrow in (a) and (b). Solid points are for 4.6K, and open symbols are for 55K. (d) Calculated spin-wave intensity for the zigzag AFM order of the Heisenberg model with up to third neighbor interactions. (e) Same as (d), but for the stripy AFM order of the Heisenberg model with up to third neighbor interactions. (f) Same as (d), but for the stripy AFM order of the Heisenberg model with up to third neighbor interactions, showing a different perspective.

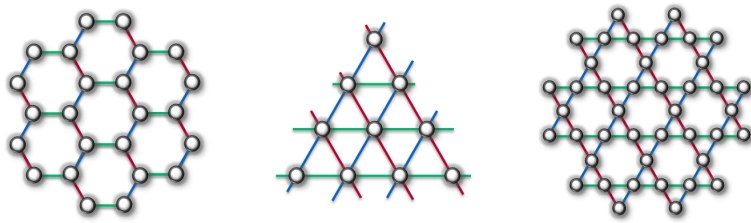


Figure 2.13: The honeycomb, triangular, and Kagomé lattices with the Kitaev interactions. $S^x S^x$, $S^y S^y$, and $S^z S^z$ interactions are indicated by red, blue, and green lines, respectively.

2.4 Kitaev-Heisenberg model on the triangular lattice

In addition to the honeycomb lattice, it has been proposed that the KH model can be realized in other lattices built from edge-sharing IrO_6 octahedra [26] as shown in Fig. 2.13. Kimchi and Vishwanath [26] have given classical phase diagrams of the KH models on triangular, Kagomé, face-centered cubic, pyrochlore, and hyperkagome lattices. The KH model on these lattices cannot be exactly-solved anymore even at the Kitaev limit. In this section, we introduce the KH model (or the quantum compass-Heisenberg model [107]) on triangular lattice and the iridium compound $\text{Ba}_3\text{IrTi}_2\text{O}_9$ that is considered as being described by the KH model. Since there is the Kitaev-type frustration breaking $SU(2)$ spin-rotational symmetry in addition to geometrical frustration, the ground state is highly non-trivial. Therefore, it is interesting to make the phase diagram of the model on triangular lattice by using unbiased numerical methods.

2.4.1 Kitaev-Heisenberg model on the triangular lattice

The Hamiltonian of the KH model on the triangular lattice is the same as that on the honeycomb lattice Eq. (2.38). However, J_z , J_y , and J_x bonds are defined on the triangular lattice shown in Fig. 2.14. The KH model on the triangular lattice was first discussed by Rousouchatzakis *et. al.* [28]. They have found an incommensurate and non-coplanar spin pattern forming a lattice of the \mathbb{Z}_2 vortices near the AFM Heisenberg limit. This magnetic order with the \mathbb{Z}_2 vortices is induced by the Kitaev interaction. The vortices are topologically-stable point defects of $SO(3)$ order parameter [109]. In contrast to the \mathbb{Z} vortices driving the Berezinsky-Kosterlitz-Thouless transitions [110, 111], the clockwise and counter-clockwise vortices of the \mathbb{Z}_2 vortices are topologically

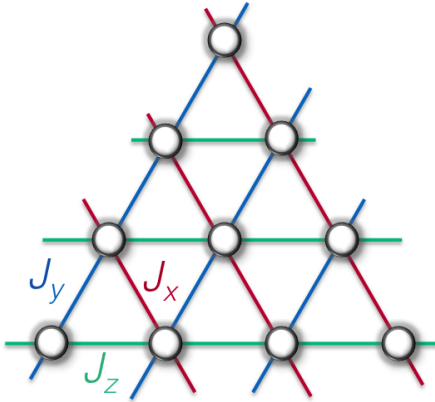


Figure 2.14: The triangular lattice with the Kitaev interaction. J_x , J_y , and J_z bonds are indicated by red, blue, and green lines, respectively.

the same, and thus the vortices are “ \mathbb{Z}_2 ”.

At the FM Heisenberg limit, FM phase appears. The order-parameter space covers the whole sphere of the spin space in the FM phase. However, it has been suggested that the finite Kitaev coupling discretizes the order-parameter space to the \mathbb{Z}_6 , leading to the \mathbb{Z}_6 FM phase [29].

Classically, a nematic state with sub-extensive degeneracy has been suggested at the AFM Kitaev limit point [28]. However, the quantum-mechanical property of the nematic phase was unclear. Becker *et. al.* have discussed the quantum ground state, and have been found out that the sub-extensive degeneracy is partially lifted due to order-by-disorder mechanism [29]. Jackeli and Avella have analyzed the nematic phase, and have obtained the same result [108]. As above, interesting phases have been suggested on the model, and thus it is interesting to study the model systematically by performing DMRG. The phase diagram of the model and property of each phase will be discussed in much more detail in Chap. 5

2.4.2 Experiments of $\text{Ba}_3\text{IrTi}_2\text{O}_9$

There is a candidate material for the KH model on triangular lattice $\text{Ba}_3\text{IrTi}_2\text{O}_9$ [27]. The crystal structure of $\text{Ba}_3\text{IrTi}_2\text{O}_9$ is shown in Fig. 2.15 (a). $\text{Ba}_3\text{IrTi}_2\text{O}_9$ has a layered triangular structure consisted of IrO_6 as shown in Fig 2.15 (b). The magnetic properties are controlled by the $j = 1/2$ state of the Ir^{4+} ion. The Curie-Weisse temperature determined from the temperature dependence of magnetic susceptibility is found to be negatively large with $\theta_{CW} \sim -130\text{K}$ [27]. Therefore, it is considered that a magnetic coupling is strong. However, no magnetic ordering is observed in susceptibility and heat capacity measurements down to 0.35K. Magnetic heat capacity follows a power

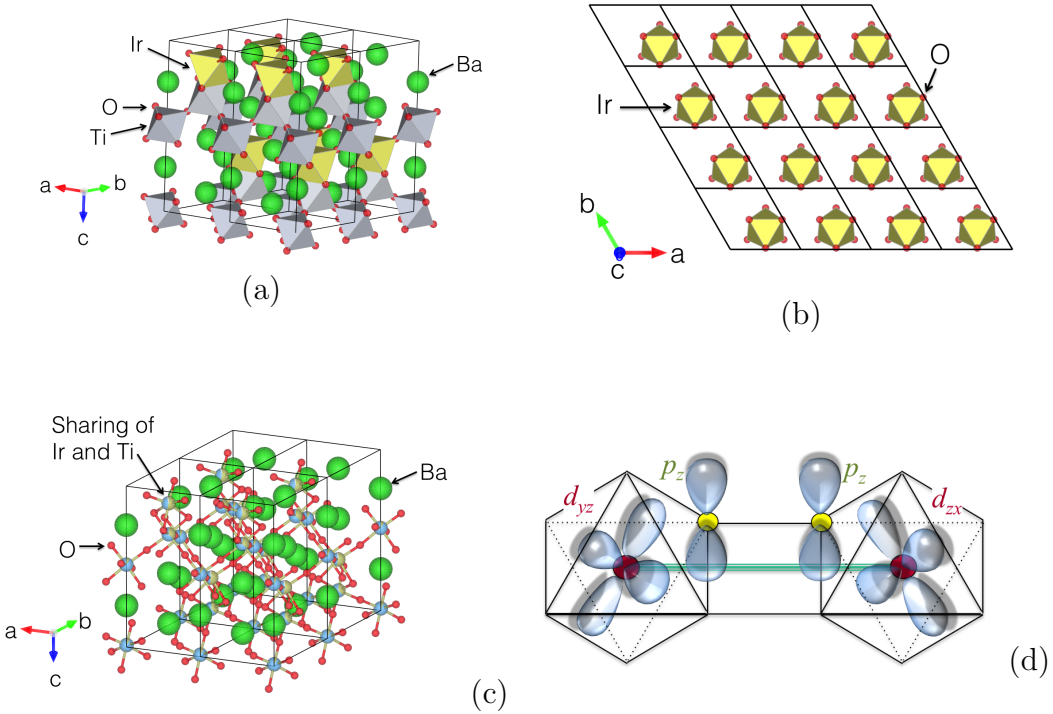


Figure 2.15: The crystal structures of $\text{Ba}_3\text{IrTi}_2\text{O}_9$ [112]. (a) The pure crystal structure of $\text{Ba}_3\text{IrTi}_2\text{O}_9$. Red and green points show O and Ba ions, respectively. Ir and Ti ions are at the center of yellow and gray octahedra, respectively. (b) IrO_6 constructs the triangular lattice. (c) The real crystal structure used in the experiment by Dey *et. al.* [27]. The mixing color of yellow and blue shows the high-rate site sharing of Ir and Ti . (d) The hopping pathways in $\text{Ba}_3\text{IrTi}_2\text{O}_9$, showing oxygen-mediated Ir-O-O-Ir electron hopping that corresponds to Fig. 2.10 (a). Compared to Na_2IrO_3 , the edge of IrO_6 is not directly shared, but the mechanism of hopping process giving rise to the Kitaev interaction is the same.

law at low temperatures, suggesting spin liquid behavior. However, other possibilities are not excluded, because a large number ($37 \pm 10\%$) of site sharing of Ir^{4+} ions with Ti^{4+} ions is reported as shown in Fig 2.15 (c). The site sharing can induce disordered spin-glass-like behavior. Thus, it is desirable to make $\text{Ba}_3\text{IrTi}_2\text{O}_9$ with high purity.

The Kitaev-type interaction in $\text{Ba}_3\text{IrTi}_2\text{O}_9$ can be explained in much the same way as that in Na_2IrO_3 . However, the oxygen-mediated exchange hopping of electrons is slightly different. The Ir-O-Ir exchange paths that make Kitaev interaction in Na_2IrO_3 no longer exist in $\text{Ba}_3\text{IrTi}_2\text{O}_9$. Instead of Ir-O-Ir exchange paths, there are Ir-O-O-Ir exchange paths in $\text{Ba}_3\text{IrTi}_2\text{O}_9$ as shown in Fig. 2.15 (d). These paths still lead to the Kitaev interactions but with smaller magnitude compared to the Heisenberg interactions.

Chapter 3

Numerical method: density-matrix renormalization group (DMRG)

Since Steven White devised numerical-calculation method density-matrix renormalization group (DMRG) method, DMRG has been one of the most reliable and useful methods in strongly correlated electron systems [25, 113]. Using DMRG, it is possible to calculate physical properties of various systems with very large system size. DMRG was firstly applied for only one-dimensional system, but it has recently been applied to two- and three-dimensional systems by using high performance computing technology. The main idea of DMRG is that the flow of renormalization is constructed by using appropriate density-matrix space.

Historically, as DMRG is originated from Noack's real space renormalization group obtaining low-energy effective theory of many-body system, its algorithm is based on the formalization of real space renormalization group. However, the renormalization in DMRG is not a usual renormalization. In the renormalization of DMRG, degrees of freedom are systematically traced out, and the effective Hamiltonian is obtained. However, the renormalization of DMRG is not related to cutting off of ultraviolet or infrared energy. In this sense, the renormalization of DMRG is not the usual renormalization.

By maintaining accuracy in DMRG comparable to the exact diagonalization method, it is possible to investigate the physical properties of large systems. To prevent exponential increase in the Hilbert space due to expansion of the system, the amount of information handled by DMRG is limited to the information that is needed to describe the ground state.

3.1 Density-matrix renormalization group (DMRG)

The whole system treated by DMRG is divided into a “system block” and an “environment block” to take into account the quantum fluctuations of the environment. The entire system composed of system and environment block is called super block. First of all, the super block is a small system that can be easily treated by exact diagonalization. We take the ground state $|\psi\rangle$. A system block with l sites can be represented by the Hilbert space smaller than dimension M^S whose basis is $|m_l^S\rangle$. In the same way, the basis of environment block can be represented by $|m_l^E\rangle$. These bases construct a complete system. The Hamiltonian with site l is represented by \hat{H}_l . Two single sites are added into the system block and environment block to expand the super block as shown in Fig. 3.1. \hat{H}_{l+1} is constructed by the basis $|m_l^S\sigma\rangle \equiv |m_l^S\rangle|\sigma^S\rangle$, where $|\sigma\rangle$ is the basis of added single site with the number of state N_{site} .

\hat{H}_{2l+2} is constructed by using the basis $|m_l^S\sigma\rangle|m_l^E\sigma\rangle$. By diagonalizing \hat{H}_{2l+2} , the ground state is obtained

$$|\psi\rangle = \sum_{m^S=1}^{M^S} \sum_{\sigma^S=1}^{N_{\text{site}}} \sum_{\sigma^E=1}^{N_{\text{site}}} \sum_{m^E=1}^{M^E} \psi_{m^S\sigma^S\sigma^E m^E} |m^S\sigma^S\rangle|m^E\sigma^E\rangle \quad (3.1)$$

$$\equiv \sum_i^{N^S} \sum_j^{N^E} \psi_{ij} |i\rangle|j\rangle \quad (3.2)$$

with

$$\langle\psi|\psi\rangle = 1, \quad (3.3)$$

where $\psi_{m^S\sigma^S\sigma^E m^E} = \langle m^S\sigma^S; \sigma^E m^E | \psi \rangle$, and $|i\rangle \equiv |m^S\sigma^S\rangle$ and $|j\rangle \equiv |m^E\sigma^E\rangle$ are the basis of the system block with added single site and that of the environment block with added single site, respectively. Their dimensions are $N^S = M^S N_{\text{site}}$ and $N^E = M^E N_{\text{site}}$. The dimension can be truncated as $M^S < N^S$ by using reduced density matrix of the ground state as mentioned below.

The ground state written by Eq. (3.2) is approximated as follows by using only $M^S (\leq N^S)$ bases less than N^S bases of the system block. $|u^\alpha\rangle (\alpha = 1, \dots, M^S)$ can be expanded by using basis of the system block as follows:

$$|u^\alpha\rangle = \sum_i u_i^\alpha |i\rangle (u_i^\alpha = \langle i|u^\alpha\rangle). \quad (3.4)$$

The ground state is thus approximated by

$$|\tilde{\psi}\rangle = \sum_{\alpha=1}^{M^S} \sum_{j=1}^{N^E} d_{\alpha,j} |u^\alpha\rangle |j\rangle \quad (3.5)$$

($M^S \leq N^E$). Then, we consider the problem of minimizing

$$S = ||\psi\rangle - |\tilde{\psi}\rangle|^2 \quad (3.6)$$

(variational principle). $|\tilde{\psi}\rangle$ can be written as

$$|\tilde{\psi}\rangle = \sum_{\alpha=1}^{M^S} |u^\alpha\rangle \left(\sum_{j=1}^{N^S} d_{\alpha,j} |j\rangle \right) \quad (3.7)$$

$$= \sum_{\alpha=1}^{N^S} d_\alpha |u^\alpha\rangle |v^\alpha\rangle \quad \left(d_{\alpha,j} = d_\alpha v_j^\alpha, |v^\alpha\rangle = \sum_{j=1}^{N^S} v_j^\alpha |j\rangle \right) \quad (3.8)$$

$$= \sum_{i=1}^{N^S} \sum_{j=1}^{N^E} \sum_{\alpha=1}^{M^S} d_\alpha u_i^\alpha v_j^\alpha |i\rangle |j\rangle. \quad (3.9)$$

S is given by

$$S = \sum_{i=1}^{N^S} \sum_{j=1}^{N^E} \left(\psi_{ij} - \sum_{\alpha=1}^{M^S} d_\alpha u_i^\alpha v_j^\alpha \right). \quad (3.10)$$

The problem of minimization is closely related to the singular value decomposition. When the coefficient of wave function of the exact ground state is (i, j) component of matrix $N^S \times N^E$, matrix $\psi = \{\psi_{ij}\}$ can be decomposed by the singular value decomposition as follows.

$$\psi_{ij} = \sum_{\alpha=1}^{\min(N^S, N^E)} u_i^\alpha d_\alpha v_j^\alpha, \quad (3.11)$$

$$\psi = UDV^*, \quad (3.12)$$

where U is $N^S \times N^S$ unitary matrix, V is $N^S \times N^E$ orthogonal matrix, and D is $N^S \times N^S$ diagonal matrix. The diagonal component of D is the singular value of ψ . Then, we can obtain the optimized solution by replacing the m diagonal components from the largest with d_α , and the corresponding U and V with u and v . The singular value decomposition is closely related to the density matrix

$$\rho = \psi\psi^* = UD(V^*V)DU^* = UD^2U^*. \quad (3.13)$$

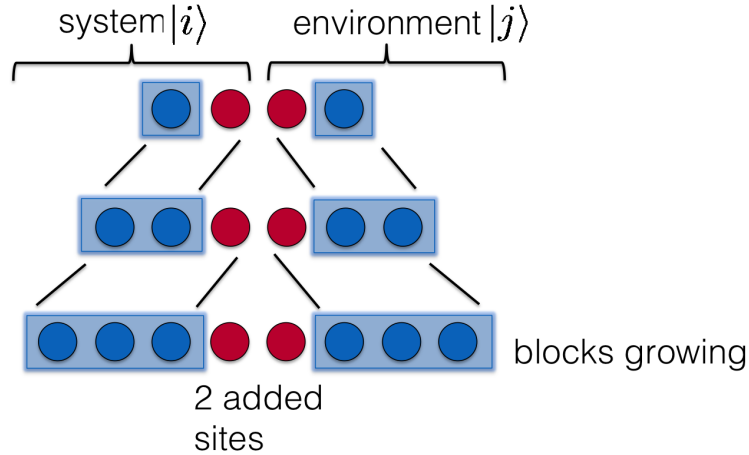


Figure 3.1: Schematic view of expanding the super block in the infinite algorithm of DMRG. Red single sites are inserted between the system and environment blocks.

ρ is thus diagonalized by the unitary matrix U , and the square root of the eigenvalue is a component of D . Now, we consider the density matrix of a ground state ψ , which is called a “target” state. By taking summation of the diagonal component,

$$\text{Tr}\rho = \sum_i \sum_j \psi_{ij} \psi_{ij} = 1 \quad (3.14)$$

$$= \text{Tr}(UD^2U^*) = \text{Tr}(D^2). \quad (3.15)$$

The accuracy of the approximation can be expected as

$$P_m = 1 - \sum_{i=1}^m (D^2)_{ii}, \quad (3.16)$$

which is called the truncation error.

3.2 Algorithm of DMRG

3.2.1 Infinite system algorithm

Step 1.

Make a system block Hamiltonian of the number of sites l . Start from a very small system blocks such as $l = 1$. The number of states of the Hilbert space of the system block is M^S . When the number of states is smaller than M^S , the Hamiltonian is strictly represented, but it becomes

approximate when the number of states exceeds M^S . The Hamiltonian of the environment block is also constructed in the same manner.

Step 2.

Add a single site to both the system block and the environment block as shown in red sites in Fig. 3.1. Since the two sites are added, the size of the super block is expanded. By inserting the two additional sites between the system block and environment block, the accuracy of DMRG becomes higher. The number of states of the new system block with the added single site is $N^S = M^S N_{\text{site}}$, and its basis is constructed by $|M^S \sigma\rangle = |M^S\rangle |\sigma\rangle$. In the same way, the number of states of the new environment block with the added single site is $N^E = M^E N_{\text{site}}$, and its basis is constructed by $|m^E \sigma\rangle = |m^E\rangle |\sigma\rangle$.

Step 3.

Construct the super block Hamiltonian \hat{H}_{2l+2} with $2l + 2$ sites. The number of states of the Hilbert space is $N^S N^E$.

Step 4.

Calculate the ground state by diagonalizing \hat{H}_{2l+2} . Numerical cost is the largest.

Step 5.

Calculate the reduced density matrix $\hat{\rho} = \text{Tr}_E |\psi\rangle \langle \psi|$ of the ground state obtained in Step 4, and sort the eigenvalues in decreasing order after diagonalizing the density matrix. Construct the new basis of the system block by using the $M^S < N^S$ eigen states from the largest. The rectangular matrix $u_{m^S \sigma}^\alpha = \langle m^S \sigma | O | w^\alpha \rangle$ for transformation is made by the eigensate. The environment block is handled in the same way.

Step 6.

By operating $u_{m^S \sigma}^\alpha$ to \hat{H}_{l+1} , a transformed Hamiltonian $\hat{H}_{l+1}^{tr} = (u_{m^S \sigma}^\alpha)^\dagger \hat{H}_{l+1} (u_{m^S \sigma}^\alpha)$ is obtained, the Hilbert space of which is truncated to M^S . The environment block is handled in the same way. After this, go to Step 2, and repeat the same process above. Not only the Hamiltonian but also physical operators we want to know are transformed simultaneously.

Step 7.

When the size of the super block is expanded to that we want, the infinite system algorithm of DMRG is completed.

3.2.2 Finite system algorithm

By using the infinite system algorithm, we find that a large system can be computed by compressing the information of the Hilbert space. However, the algorithm is not sufficient. The ground state of \hat{H}_{2l+2} is obtained by optimizing the ground state of \hat{H}_{2l} , not \hat{H}_{2l+2} . If our system is large enough $l \sim \infty$, it is considered that $\hat{H}_{2l+2} \simeq \hat{H}_{2l}$. Thus, the process mentioned above can be appropriate. However, the system is very small in the initial DMRG steps, so that the infinite system algorithm cannot give accurate results. Therefore, such a renormalization process should be carried out while fixing system size, and should be done in the finite system algorithm. In addition, the finite system algorithm can treat complicated models with long range interactions that is important for applying DMRG to two-dimensional systems.

Before starting the finite system algorithm, the super block is expanded to L sites system by using the infinite system algorithm. Then, the finite system algorithm is carried out after Step 6 as shown in Step 6.5. Note that the system and the environment block are not expanded simultaneously, but when the system (environment) block is expanded, the environment (system) block is contracted maintaining the size of super block fixed. The important point is that we can renormalize the system and environment blocks with the knowledge of full-size Hamiltonian.

Step 6.5

Renormalize and expand the system (environment) block, and update the information of system block. Then, old information of the contracted environment (system) block is used, so the size of the whole system is fixed. All updated information of the system (environment) block should be saved to memory or hard disk drive because the information of the updated system (environment) block is used later as the information of a contracted system (environement) block. After the size of the system (environment) block reaches maximum size, one can renormalize and expand the environment (system) block while the system (environment) block is contracted. The expansion and contraction of the system and environment blocks are repeated again and again. In this step 6.5, the added single site goes to left and right in the super block, and one period of the movement is called “1 sweep” as shown in Fig. 3.2.

We apply DMRG to two-dimensional system by introducing long-range interactions as shown in Fig. 3.3. Two-dimensional system is constructed by introducing long-range interactions into the usual one-dimensional DMRG.

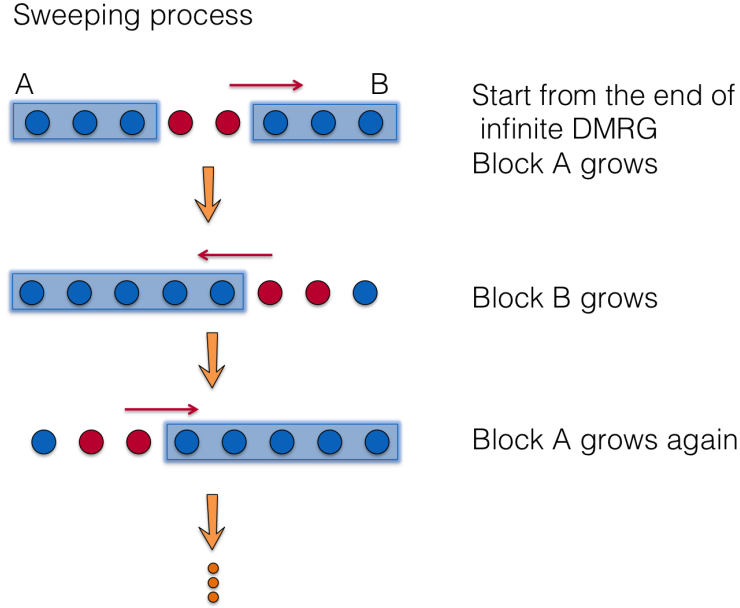


Figure 3.2: Sweeping process in the finite system algorithm in DMRG

The red lines show the interactions in the usual one-dimensional DMRG, and the green lines show long-range interactions. Two added sites are moved along the red snake-like line. The purple and orange regions are the system and environment blocks, respectively. If there are interactions indicated by dashed green lines along the vertical orange arrow with “cylindrical geometry”, the system is periodic along vertical orange arrow, and the lattice forms cylindrical geometry. Furthermore, if there are additional interactions indicated by dashed green lines along the horizontal orange arrow, the system is periodic along both vertical and horizontal orange arrows, forming “toroidal geometry”. The sweeping process is complicated in two-dimensional case. The process of the triangular lattice is shown in Fig. 3.4. The interactions that should be taken into account change with sweeping, so that the algorithm becomes much complicated. In general, the long-range interactions make the convergence of DMRG worse, which need a lot of sweeps, for example 10 times of the sweep.

3.3 Entanglement study in quantum spin systems

The states described by Landau’s theory can be characterized by local correlation and order parameter. However, there are quantum states that are beyond the description of the theory. Such states cannot be characterized

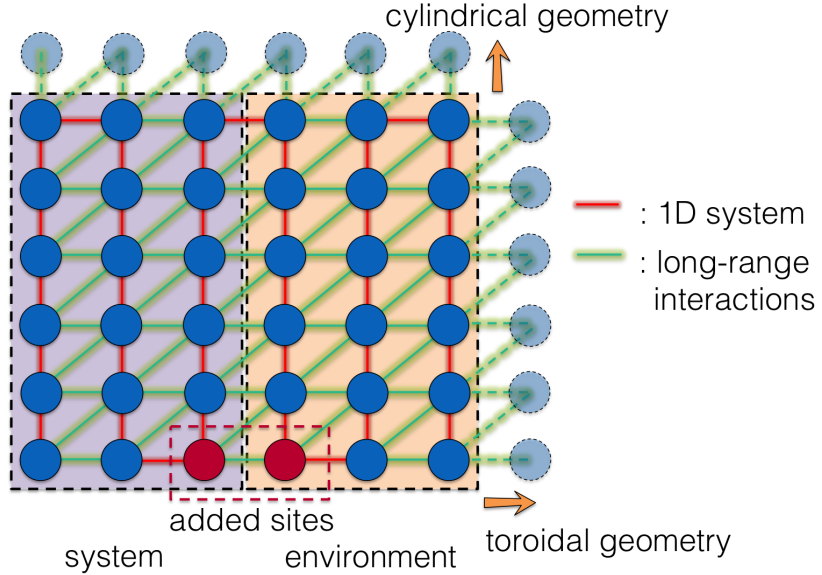


Figure 3.3: The construction of two-dimensional system in DMRG. The usual one-dimensional DMRG is constructed along the red snake-like line. Then, long-range interactions indicated by green lines are introduced and two-dimensional system is constructed. If periodic boundary condition is taken along the vertical orange arrow, the lattice forms cylindrical geometry. If periodic boundary condition is also taken along the horizontal orange arrow in addition to the periodic boundary condition along the vertical direction, then the lattice forms toroidal geometry.

by the local physical quantities. They are, for example, fractional quantum Hall-liquid state and spin-liquid state. When characterizing such states, local order parameters are no longer useful, and it was suggested that entanglement detecting non-local correlations is used to characterize such states [114]. The nature of entanglement is originally studied in quantum informational physics [115, 116]. It has been found that entanglement is useful for studying some unfamiliar and exotic quantum states in condensed matter physics. In this section, we briefly review the application of entanglement in condensed matter physics.

In a system composed of two subsystems A (system block) and B (environment block), the wave function of the system calculated by DMRG can be written as follows by taking the Schmidt decomposition of a many-body state $|\psi\rangle$

$$|\psi\rangle = \sum_i p_i |p_A^i\rangle |p_B^i\rangle = \sum_i e^{-\xi_i} |p_A^i\rangle |p_B^i\rangle, \quad (3.17)$$

where p_i is the eigenvalue of reduced density-matrix $\rho_A = \text{Tr}_B |\psi\rangle\langle\psi| = e^{-\mathcal{H}_E}$ for subsystem A (or $\rho_B = \text{Tr}_A |\psi\rangle\langle\psi|$ for subsystem B). The distribution of ξ_i

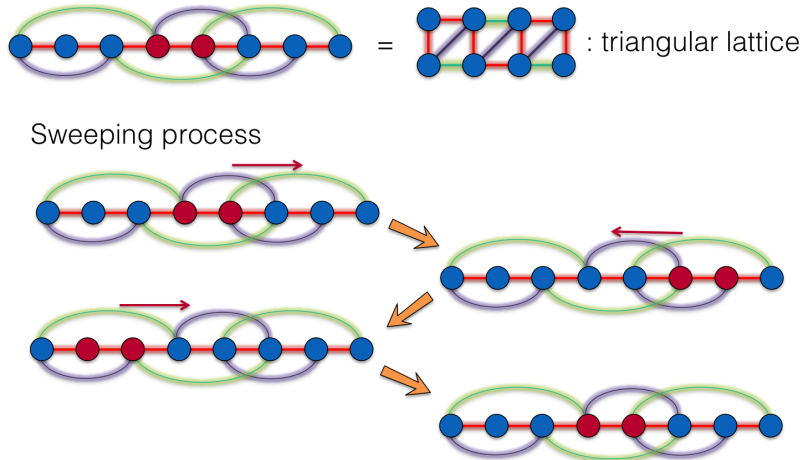


Figure 3.4: The sweeping process with long-range interactions. The sweeping process of the triangular lattice case is shown. The related interactions are different in every step.

is called entanglement spectrum, where ξ_i is the eigenvalue of entanglement Hamiltonian \mathcal{H}_E . The von Neumann entanglement entropy containing non-local topological properties can be written as

$$S_E = - \sum_i p_i \ln p_i = \sum_i \xi_i e^{-\xi_i}. \quad (3.18)$$

When the ground state is calculated based on DMRG, the reduced density matrix appears naturally, leading to the von Neumann entanglement entropy and entanglement spectrum. If we understand the principle of DMRG, we can know the entanglement properties of quantum spin systems.

3.3.1 Entanglement entropy

In one-dimensional systems, the scaling behavior of entanglement entropy is well understood: In the thermodynamic limit, the entropy is finite for gapped systems, while it is logarithmically divergent for gapless systems [117, 118]. The scaling behavior is universal depending on central charge and not on the microscopic detail of the systems. In spite of extensive studies, however, the entanglement structure in high dimensions more than one dimension has not necessarily been resolved. The scaling behavior of entanglement entropy has been studied and the ground state of a local Hamiltonian is generally believed to produce an “area law” scaling [119–126]: the entanglement entropy is proportional to the area of boundary around subsystems. The deviation from the area law indicates the existence of certain long-range or non-local

correlations. There are the subleading corrections to the scaling behavior that are regarded as universal quantities identifying and characterizing quantum phases and phase transitions.

3.3.2 Entanglement entropy in gapped systems

We discuss the scaling behavior of entanglement entropy. We consider local Hamiltonian. If the system is gapped, entanglement entropy satisfies the area law

$$S_A \propto \text{boundary size of } \partial A \quad (3.19)$$

$$\sim \alpha L, \quad (3.20)$$

where L is the size of the boundary $\partial A (= \partial B)$ between A and B. In one-dimensional system, ∂A is a point, so S_A is a constant value [127]. The existence of the area law in many-body entanglement is due to the locality of interactions and the existence of energy gap. In a gapped system, correlations are short-range, so that the system can correlate with the rest of the system only on the boundary. Thus, S_A scales as the size of ∂A . The deviation from the area law and some sub-leading contributions indicate the existence of certain long-range and non-local correlations.

For example, such sub-leading term is due to the existence of topological entanglement entropy that is a sub-leading constant term apart from leading the area law term [128, 129].

$$S_A \sim \alpha L - \gamma \quad (3.21)$$

The topological entanglement entropy $\gamma > 0$ originates from the topological nature of the system with non-local correlation.

DMRG and tensor network make use of the area law. In general, the Hilbert space of quantum many-body state is so huge. However, the states following the area law is only a part of the Hilbert space [130]. By confining candidate states for the ground state to the states obeying the area law, it is possible to reduce computational cost drastically. DMRG and tensor network are produced based on this idea. In fact, the state calculated by DMRG obeys area law in one-dimensional system, which is consistent with the fact that the gapped ground state of one-dimensional system is calculated with low calculation cost and high accuracy.

3.3.3 Entanglement entropy in gapless systems

In gapless or critical system, there is the case that the area law is violated, but entanglement entropy is usually scales as the logarithm of L , showing some universal behavior. For example, the entanglement entropy in one-dimensional system described by conformal field theory scales as

$$S_A \sim \frac{c}{3} \log L, \quad (3.22)$$

where c is the central charge [118, 131]. In the case of gapless system with a Fermi surface in two dimensions, the entanglement entropy scales as [132–135]

$$S_A \sim \alpha L \log L. \quad (3.23)$$

There is the case that shows the area law with some sub-leading terms

$$S_A \sim \alpha L + \gamma \quad (3.24)$$

at conformal quantum critical points in two dimensions [136–140], and

$$S_A \sim aL + b \log L + \gamma(L_x, L_y) \quad (3.25)$$

with Nambu-Goldstone modes in two dimensions [141–143], where $\gamma(L_x, L_y)$ is a function of L_x and L_y showing some universal scaling behavior. In addition to characterizing phases themselves, the entanglement entropy is useful for detecting phase transitions. In fact, it has been found that entanglement entropy exhibits a diverging behavior as phase transition points approach [118]. If the argument is true, there is an advantage of characterizing both symmetry broken and unbroken systems.

3.3.4 Entanglement spectrum

Li and Haldane proposed entanglement spectrum that contains the full set of eigenvalues of density-matrix [144]. Writing the eigenvalues of the density matrix as $e^{-\xi_i}$, where ξ_i is an entanglement level, they have shown that the low-level entanglement spectrum for Laughlin, Moore-Read and Read-Rezayi states exhibit a universal structure related to conformal field theory. The universal structure is separated from a nonuniversal high-level spectrum by entanglement gap that is finite in the thermodynamic limit. This gap itself is proposed to be a “fingerprint” of the topological order. Since the proposal, entanglement spectrum has been studied in various systems including frac-

tional quantum Hall systems [144–147], topological insulators [148, 149], spin chain [150], and Kitaev honeycomb lattice model [151]. Furthermore, it has been realized that the scaling of the Schmidt gap defined by the difference between the two largest eigenvalues of the reduced density matrix is useful for detecting critical points through the studies for one-dimensional Kugel-Khomskii model [152], spin chains [153, 154], and two-dimensional quantum Ising model [155], and spin-1/2 XXZ, and spin-1 bilinear-biquadratic models on triangular lattice [156]. The entanglement spectrum is thus now accepted to be a quantity characterizing not only various phases but also phase transitions.

Chapter 4

The extended Kitaev-Heisenberg model on the honeycomb lattice

Motivated by previous studies reviewed in Sec. 2.3, we examine the extended KH model Eq. (2.44) including anisotropic off-diagonal interactions tailored for Na_2IrO_3 . This extended model takes into account the direct electron hoppings between Ir ions in addition to the oxygen-mediated electron hoppings and the trigonal-distortion effect. We treat the model in a fully quantum-mechanical manner by using DMRG, and make a phase diagram of the model around Kitaev spin-liquid phase. We find a ferromagnetic (FM) phase, a 120° AFM phase, two kind of incommensurate (IC) phases, and zigzag-type AFM phase next to the Kitaev spin-liquid phase. We obtain the zigzag AFM phase at the $K \ll 0$ region that is relevant for Na_2IrO_3 . We find that the anisotropic off-diagonal interactions from the trigonal distortion is important for stabilizing the zigzag AFM ordering. In addition, we confirm that the zigzag phase exhibits spin-spin correlation similar to a model more realistic for Na_2IrO_3 [18], and is continuously connected to the ground state of the more realistic model.

Furthermore, we investigate entanglement entropy and entanglement spectrum of the extended KH model. We find that the lowest level of entanglement spectrum in magnetically ordered states is non-degenerate. This is clearly in contrast to the Kitaev spin-liquid state, where all of entanglement levels form pairs. Such a degenerate structure in the Kitaev spin liquid is due to special nature of the Kitaev model that has gauge structure coming from topological nature, and depends on boundary conditions. As a result, the Schmidt gap defined as the energy difference between the lowest and first excited entanglement levels changes at phase boundary between the Kitaev spin-liquid and

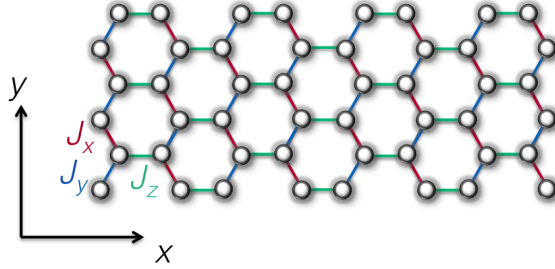


Figure 4.1: Honeycomb lattice with 6×8 sites with periodic boundary condition. Blue dotted, red dashed-dotted, and green solid bonds labeled by \mathcal{J}_x , \mathcal{J}_y and \mathcal{J}_z have $S^x S^x$, $S^y S^y$ and $S^z S^z$ terms in a Kitaev model, respectively. We define the x -axis direction as an armchair-edge direction and the y -axis direction as a zigzag-edge direction.

other magnetically ordered phases. However, we find that the Schmidt gap cannot be a good measure of phase transition between magnetically ordered phases.

This chapter is organized as follows. In Sec. 4.1, the extended KH model we focus on is introduced. The numerical condition of our DMRG simulations are then given. In Sec. 4.2, our results are shown. The phase diagram around the Kitaev spin liquid is shown. This phase diagram gives the relation among the spin-liquid phase, the zigzag AFM phase realized in Na_2IrO_3 , and the other phases. Physical properties such as energy, spin-spin correlations, and entanglement spectrum are also shown. Finally, the summary and outlook of this chapter are given.

4.1 Model and Method

We show the Hamiltonian of the extended KH model introduced in Sec. 2.3 again,

$$\hat{\mathcal{H}} = \sum_{\Gamma} \sum_{\langle lm \rangle \in \Gamma} \hat{\mathcal{H}}_{lm} \quad (4.1)$$

$$\begin{aligned} \hat{\mathcal{H}}_{lm} &= KS_l^{\gamma}S_m^{\gamma} + J \left(S_l^{\alpha}S_m^{\alpha} + S_l^{\beta}S_m^{\beta} \right) \\ &+ I_1 \left(S_l^{\alpha}S_m^{\beta} + S_l^{\beta}S_m^{\alpha} \right) \\ &+ I_2 \left(S_l^{\alpha}S_m^{\gamma} + S_l^{\gamma}S_m^{\alpha} + S_l^{\beta}S_m^{\gamma} + S_l^{\gamma}S_m^{\beta} \right), \end{aligned} \quad (4.2)$$

where Γ represents the set of the three types of bonds $\{J_x, J_y, J_z\}$ (see Fig. 4.1) and $(\alpha, \beta, \gamma) = (x, y, z)$, (z, x, y) , and (y, z, x) on the J_z , J_y and J_x bond,

respectively, and $\langle lm \rangle$ runs over all possible bonds belonging to Γ . For example, $\hat{\mathcal{H}}_{lm}$ is as follows on the J_z bond

$$\begin{aligned}\hat{\mathcal{H}}_{lm} = & KS_l^z S_m^z + J(S_l^x S_m^x + S_l^y S_m^y) \\ & + I_1(S_l^x S_m^y + S_l^y S_m^x) \\ & + I_2(S_l^x S_m^z + S_l^z S_m^x + S_l^y S_m^z + S_l^z S_m^y).\end{aligned}\quad (4.3)$$

We note that the I_1 and I_2 terms are added to the KH model consisting of the K and J terms. The I_1 term mainly originates from a feature of an edge-shared octahedron with total angular momentum $j = 1/2$ and the I_2 term originates mainly from trigonal distortions present in Na_2IrO_3 . This model (4.1) has been studied by Rau and Kee [20] as an effective model describing Na_2IrO_3 .

We calculate the ground state of this model by using DMRG method [25, 113]. The DMRG calculations are carried out under periodic boundary conditions. We take the x -axis direction along the armchair-edge direction and the y -axis direction along the zigzag-edge direction as shown in Fig. 4.1. Unless otherwise noted, we use a system with 8 (along x -axis) \times 6 (along y -axis) sites, i.e., a 48-site system. To perform DMRG, we construct a snake-like one-dimensional chain by combining the eight zigzag lines along y -axis, leading to a spin chain with long-range interactions (see Fig. 3.3). We keep 1000 states in the DMRG block and performed more than 10 sweeps, resulting in a typical truncation error 5×10^{-6} or smaller.

4.2 Results and Discussions

4.2.1 Phase diagram around spin liquid

Setting $I_1 = I_2 = 0$ in the extended KH model (4.1) leads to the KH model (2.38), whose phase diagram has been established [4–11]. In the phase diagram, a Kitaev spin liquid phase (B phase; see Sec. 2.2.3) emerges in the range of $K/J \leq -11$, when $K < 0$ and $J > 0$. An interesting issue of the extended KH model concerning Na_2IrO_3 is to find a zigzag-type AFM phase around the Kitaev spin-liquid phase [20]. Since the zigzag-type AFM phase is next to the Kitaev spin-liquid phase in the parameter region of $K < 0$ and $J > 0$, we use these signs in the rest of this chapter. It is also interesting to investigate the $K > 0$ and $J < 0$ region, but it will be a future issue.

Fixing $K/J = -25$, we find a zigzag-type AFM phase next to the Kitaev spin-liquid phase when $I_1/J > 0$ and $I_2/J < 0$ as shown in Fig. 4.2.

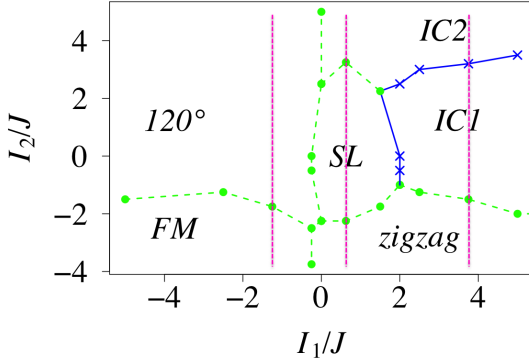


Figure 4.2: Phase diagram of the extended KH model (4.1). There are a ferromagnetic phase (FM), a 120° AFM phase (120°), a Kitaev spin-liquid phase (SL), two incommensurate phases (IC1, IC2), and zigzag-type antiferromagnetic phase (zigzag). The circle and X points are determined by the second derivative of energy with respect to I_2 and connected by lines. The boundaries denoted by blue solid lines are expected to be of first-order transition and those by green broken lines to be of continuous transition. We discuss physical properties in each phase along the dotted pink lines in Sec. 4.2.2

The presence of the zigzag state is confirmed by examining the spin-spin correlation functions for each component between sites i and j , given by $\langle S_i^x S_j^x \rangle = \langle 0 | \hat{S}_i^x \hat{S}_j^x | 0 \rangle$, $\langle S_i^y S_j^y \rangle = \langle 0 | \hat{S}_i^y \hat{S}_j^y | 0 \rangle$, and $\langle S_i^z S_j^z \rangle = \langle 0 | \hat{S}_i^z \hat{S}_j^z | 0 \rangle$, where $|0\rangle$ is the ground-state wave function. Figure 4.3 shows the calculated spin-spin correlation functions for the 48-site cluster at $I_1/J = 3.8$ and $I_2/J = -3.8$ in the zigzag phase. In the figure, the i site is indicated by a brown rhombus point. Upward red arrows and downward blue arrows denote positive and negative values of spin-spin correlation, respectively. The length of the arrows shows the absolute value of spin-spin correlation. We find the same sign within the zigzag line along the y direction in both $\langle S_i^x S_j^x \rangle$ (Fig. 4.3(a)) and $\langle S_i^y S_j^y \rangle$ (Fig. 4.3(b)), indicating the presence of the zigzag order. We note that $\langle S_i^z S_j^z \rangle$ is very short-range.

It is interesting to examine whether the zigzag phase found here smoothly connected to that obtained for a more realistic effective spin model for Na_2IrO_3 . Very recently, Yamaji *et al.* have proposed such a model based on the electronic states obtained by the first-principles calculation [18]. The model generalizes the extended KH model (4.1) with introducing ten independent exchange interactions and further-neighbor anisotropic interactions. By performing DMRG calculations, we have confirmed that the zigzag AFM phase in the effective model [18] exhibits spin-spin correlation similar to that shown in Fig. 4.3 and

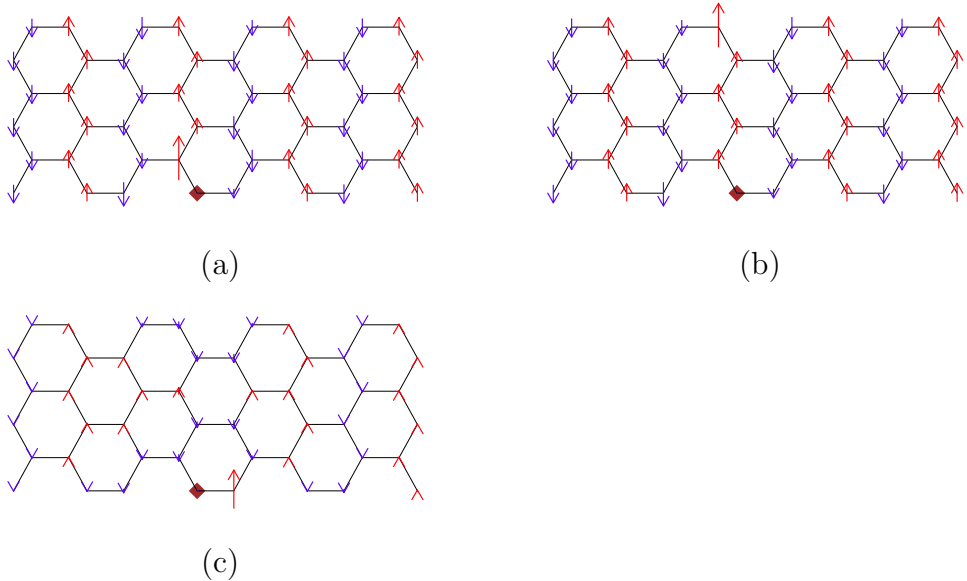


Figure 4.3: (a) $\langle S_i^x S_j^x \rangle$, (b) $\langle S_i^y S_j^y \rangle$, and (c) $\langle S_i^z S_j^z \rangle$ for zigzag-type AFM phase at $I_1/J = 3.8$ and $I_2/J = -3.8$. The i site is indicated by a brown rhombus point. Upward red arrows and downward blue arrows show positive and negative values of spin-spin correlation, respectively. The length of the arrows represents the strength of spin-spin correlation.

a similar value of the nearest neighbor spin-spin correlations.

In addition, by changing parameters continuously, we have checked that there is no phase transition between the zigzag phases of the effective model and our extended KH model. Therefore, we can say that the zigzag phase found for the effective model in Ref. 18 is smoothly connected to the zigzag phase in Fig. 4.2.

In addition to the zigzag phase, we find various magnetic phases surrounding the Kitaev spin liquid in Fig. 5.2, which are similar to those obtained in classical analysis and exact diagonalization calculations [18]. In the following, we discuss the details of each phase and phase boundaries.

4.2.2 Physical properties in each phase

We discuss physical properties in each phase along three dotted pink lines in the phase diagram (Fig. 4.2).

The zigzag, spin-liquid, and IC2 phases

Firstly, we examine the case where $I_1/J = 0.63$. With increasing I_2 , the zigzag-type AFM phase changes to an incommensurate phase denoted by IC2

through the Kitaev spin-liquid phase. Figure 4.4(a) shows the ground-state energy E per site. The second derivative of E with respect to I_2 is shown in Fig. 4.4(b). We can define phase transition points from the second derivative. At $I_2/J = -2.2$, the zigzag phase changes to the spin-liquid phase. The transition seems to be continuous, i.e., of second order. However, there remains a possibility to be of weakly first order. In order to confirm this, we need to examine the energy profile in mode detail. This remains as a future problem.

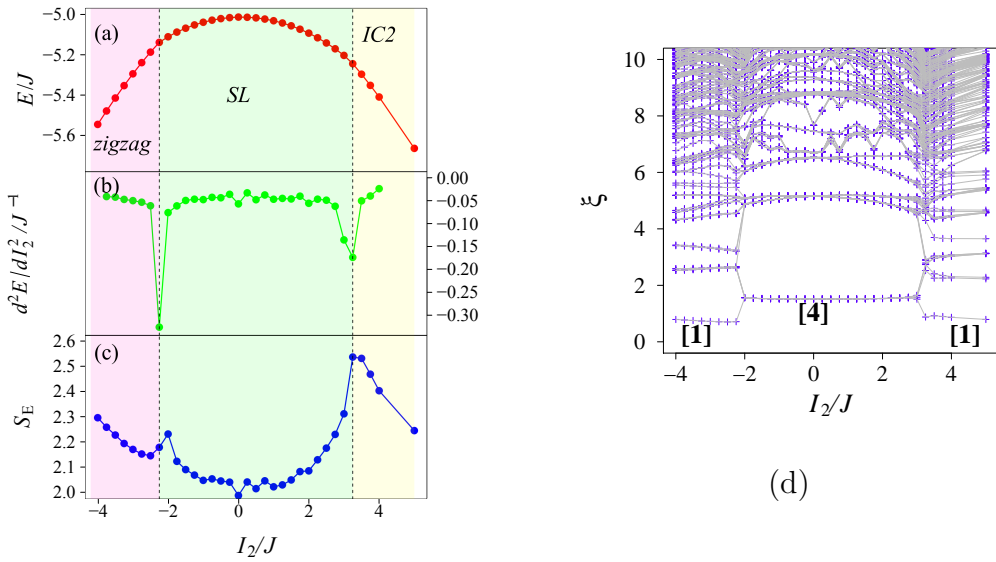


Figure 4.4: (a) The ground-state energy per site, E (red plots), (b) second derivative of E with respect to I_2 , d^2E/dI_2^2 (green plots), and (c) entanglement entropy (blue plots). $I_1/J = 0.63$. The vertical dotted lines denote phase boundary determined by the second derivative of E . (d) Entanglement spectrum for the extended KH model (4.1). $I_1/J = 0.63$. Blue crosses represent entanglement levels and gray lines connect the spectrum belonging to the same entanglement levels. $[n]$ denotes n -fold degeneracy of the lowest entanglement level in each phase.

With further increasing I_2 , the spin-liquid phase changes another phase at $I_2/J = 3.1$. The spin-spin correlation of the phase is shown in Figs. 4.5(a), 4.5(b), and 4.5(c). The correlations of x and y spin components show the same sign for all sites, but the z component exhibits a different behavior where sign depends on distance from the i site. This implies the presence of an incommensurate spin-spin correlation. We cannot clarify its propagation vector, since the system size we use is too small to determine it. We denote this phase as IC2.

Entanglement of wave function can provide useful information on quantum

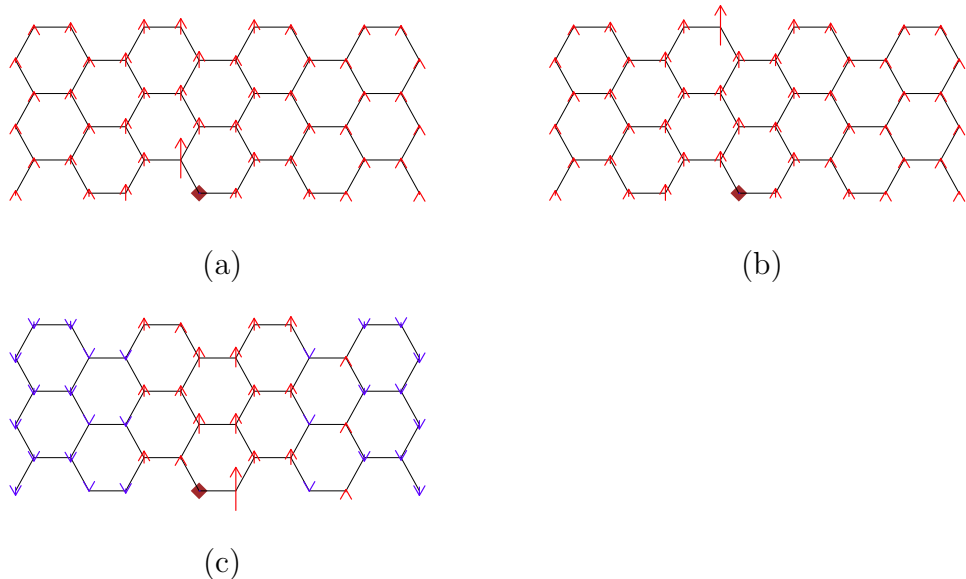


Figure 4.5: (a) $\langle S_i^x S_j^x \rangle$, (b) $\langle S_i^y S_j^y \rangle$, and (c) $\langle S_i^z S_j^z \rangle$ for IC2 phase at $I_1/J = 2.5$ and $I_2/J = 5.0$. The i site is indicated by a brown rhombus point. Upward red arrows and downward blue arrows show positive and negative values of spin-spin correlation, respectively. The length of the arrows represents the strength of spin-spin correlation.

states. It is measured by entanglement entropy and entanglement spectrum as introduced in Chap. 3. We take the A subsystem be half of the whole system. When we consider a system with toroidal geometry coming from periodic boundary conditions, we cut the whole system twice. In cylindrical geometry we divide a system into two subsystems.

In Fig. 4.4(c), S_E for $I_1/J = 0.63$ is shown. S_E shows a peak structure near phase boundary but the peak position is not exactly at the boundary. This is clearly seen at $I_2/J \simeq -2$, where there is the boundary between the zigzag and spin-liquid phases. There have been many studies about the relationship between entanglement entropy and phase transition in one-dimensional systems, [117, 118] showing a diverging behavior in S_E at phase transition points. However, such relationship has not yet been established in two-dimensional systems. Therefore, we need to make clear whether the relationship is applicable for our system or not. For this purpose, entanglement spectrum may be helpful for understanding the behavior of entanglement entropy at phase boundary.

Before discussing entanglement spectrum near the phase boundaries, we show the spectrum for a zigzag-type ordered state ($I_1/J = 3.8$ and $I_2/J = -3.8$) in Fig. 4.6, where entanglement levels are plotted from the smallest

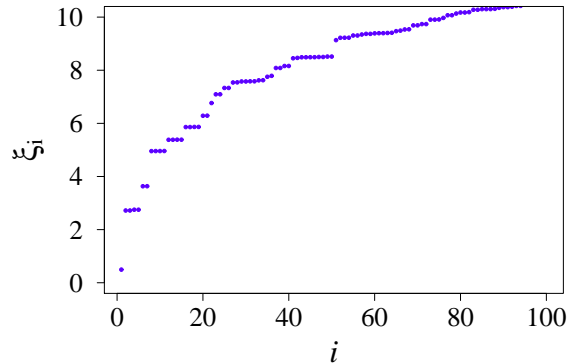


Figure 4.6: Entanglement spectrum for a zigzag-type AFM ordered ground state at $I_1/J = 3.8$ and $I_2/J = -3.8$.

value starting from $i = 1$. The lowest level of the entanglement spectrum ξ_1 is non-degenerate and separated from ξ_2 . In the following, we call the level separation $\xi_2 - \xi_1$ the Schmidt gap. We note that the non-degenerate ξ_1 is clearly in contrast to the Kitaev spin-liquid state, where all of entanglement levels form pairs (See Appendix A).

The spectral distribution of the entanglement spectrum changes with changing parameters. Figure 4.4 (d) shows the entanglement spectrum for the $I_1 = 0.63$ case. We find that the Schmidt gap changes from zero to finite at $I_2/J = -2.2$ ($I_2/J = 3.2$) with decreasing (increasing) I_2 from the spin-liquid phase. These I_2 values are consistent with the transition points obtained by the second derivative of E . Comparing $I_2/J = -2.2$ with the peak position of S_E ($I_2/J = -2.0$), we may speculate that the Schmidt gap is more appropriate than the entanglement entropy for the determination of the phase boundary in two-dimensional systems. Of course, more studies on different systems are necessary to confirm this statement. We also note that there is a different case where the Schmidt gap itself cannot be a measure of phase transition, as will be discussed below.

Here, we comment on the degeneracy of ξ_i in the Kitaev spin-liquid phase, which is located at the middle region of Fig. 4.4. The numbers $[n]$ in this figure show the number of degeneracy of the lowest entanglement level and [4] in the Kitaev spin-liquid phase denotes 4-fold degeneracy. As discussed in Appendix A, this is due to the gauge structure of the Kitaev spin liquid. We consider that the degeneracy is one of the ‘‘fingerprint’’ of the Kitaev spin liquid. Such gauge structure also appears in topological entanglement entropy [151], and thus the degeneracy of entanglement spectrum is useful for

characterizing the nature of spin-liquid phase. We discuss the entanglement spectrum of the Kitaev spin liquid in more detail in Appendix A.

The zigzag, IC1, and IC2 phases

Returning to the phase diagram in Fig. 4.2, we next examine the case where $I_1/J = 3.8$. Figures 4.7(a) and 4.7(b) show E and d^2E/dI_2^2 , respectively. With increasing I_2 , the zigzag-type AFM phase changes to the IC1 phase through a new phase denoted by IC1. The second derivative of E indicates that the phase transition between the zigzag and IC1 phases at $I_2/J = -1.5$ is of continuous and that between the IC1 and IC2 phases at $I_2/J = 3.2$ is of first order. Spin-spin correlation functions in the IC1 phase are shown in Figs. 4.8(a), 4.8(b), and 4.8(c) for $\langle S_i^x S_j^x \rangle$, $\langle S_i^y S_j^y \rangle$, and $\langle S_i^z S_j^z \rangle$, respectively. $\langle S_i^x S_j^x \rangle$ and $\langle S_i^y S_j^y \rangle$ indicate non-commensurate spin arrangement, though $\langle S_i^z S_j^z \rangle$ shows a FM correlation. This pattern of the spin-spin correlation is different from that in IC2 shown in Fig. 4.5. Therefore, we call this phase IC1.

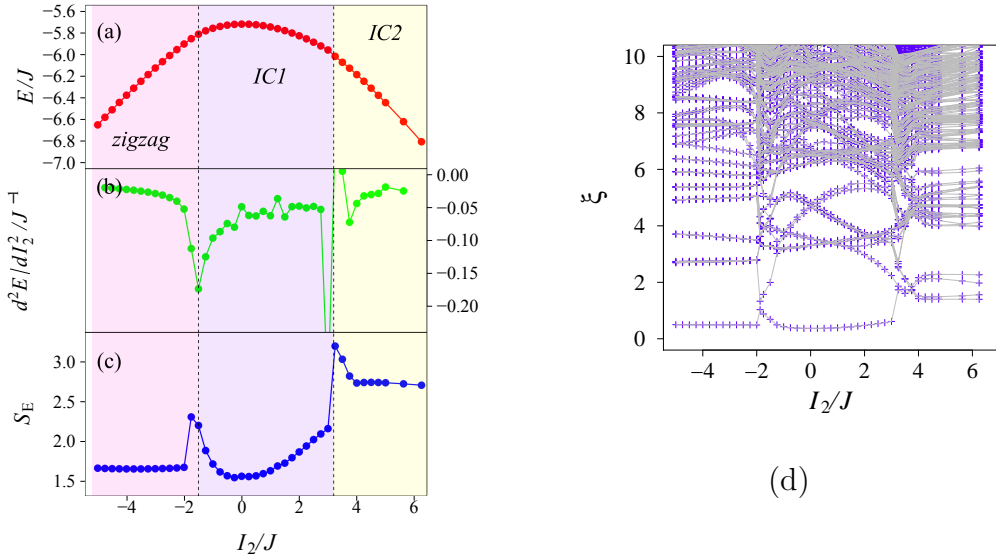


Figure 4.7: Same as Fig. 4.4, but $I_1/J = 3.8$.

The sudden change of S_E at $I_2/J = 3.2$ in Fig. 4.7(c) is consistent with the first-order transition. The entanglement spectrum and the Schmidt gap also show a change at the same value as shown in Fig. 4.7. On the other hand, the phase boundary at $I_2/J = -1.5$ disagrees with the peak position of S_E and also disagrees with the change of the Schmidt gap. Such a disagreement is different from the case of the boundary between the zigzag and spin-liquid phases discussed above.

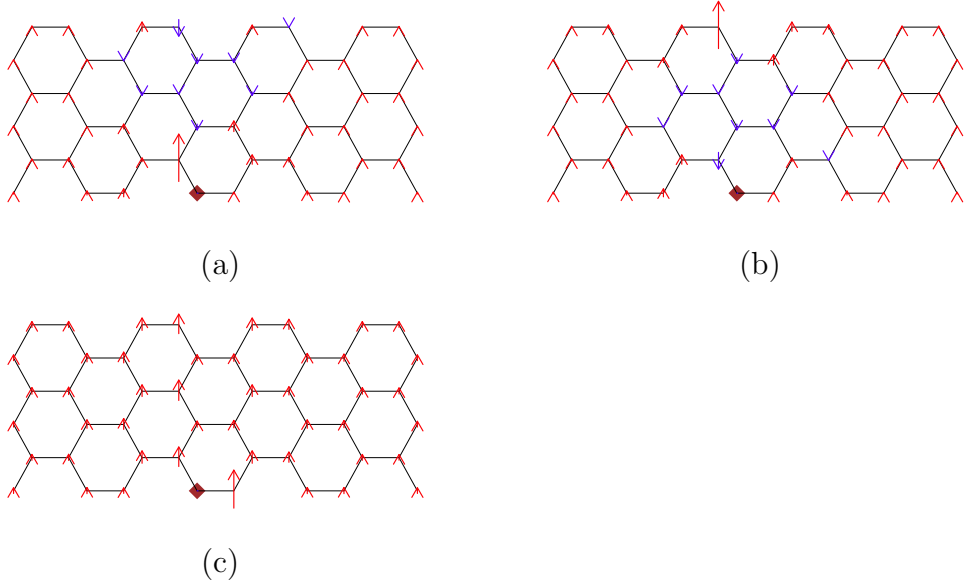


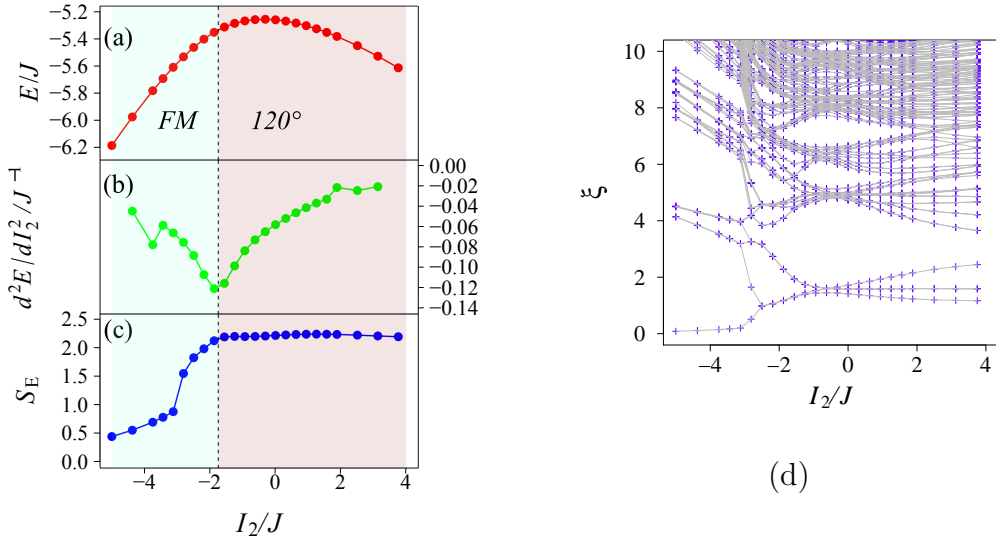
Figure 4.8: Same as Fig. 4.5, but for IC1 phase at $I_1/J = 2.5$ and $I_2/J = 2.5$.

The FM and 120° AFM phases

Thirdly, let us examine the case of $I_1/J = -1.3$. Figures 4.9(a), 4.9(b), and 4.9(c) show E , d^2E/dI_2^2 , and S_E , respectively. With increasing I_2 , phase changes from a FM phase to a 120° phase at $I_2/J = -1.8$ with a continuous transition. This 120° phase has the same spin configuration as presented by Rau and Kee [19, 20]. Entanglement entropy smoothly changes at the phase boundary, in contrast to other cases where a peak structure appears.

Figure 4.9 shows entanglement spectrum as a function of I_2 . We find that the Schmidt gap changes from zero to finite at $I_2/J = -2.8$, but there is no qualitative change at the phase boundary $I_2/J = -1.8$. This means that the Schmidt gap is not a good measure of the phase transition in this case where the FM phase changes to the 120° AFM phase. Recently it has been shown that low-energy entanglement spectrum can exhibit singular changes, even when the physical system remains in the same phase, [157] suggesting less universal information about quantum phases in the low-energy entanglement spectrum.

Therefore, we can say that our case would be such an example in two-dimensional systems, where the Schmidt gap cannot characterize phase transition points.


 Figure 4.9: Same as Fig. 4.4, but $I_1/J = -1.3$.

4.3 Summary and Outlook

We have studied the extended KH model (4.1) by using DMRG and constructed a phase diagram around the Kitaev spin-liquid phase. We have found a FM phase, a 120° phase, two kinds of incommensurate phases (IC1 and IC2), and a zigzag-type AFM phase next to the Kitaev spin-liquid phase (see Fig. 4.2). The zigzag phase exhibits spin-spin correlation similar to what is observed for a more realistic model for Na_2IrO_3 [18]. We have determined phase boundaries by using the second derivative of energy. At the boundaries, entanglement entropy does not necessarily show an anomalous behavior. This means that the entanglement entropy is not a good measure for determining phase boundary in the extended KH model.

Examining entanglement spectrum, we have found that the lowest entanglement level in magnetically ordered states is non-degenerate. This is in contrast to that of the Kitaev spin-liquid phase, where all of entanglement levels appear in pairs. We note that the degeneracy in Kitaev spin liquid is due to gauge structure and the number of its degeneracy depends on boundary condition reflecting topological nature of the Kitaev spin-liquid as discussed in Appendix A. Therefore, phase boundaries between the Kitaev spin-liquid and the magnetically ordered phases is determined by examining entanglement spectrum. In this case, the Schmidt gap, defined as the difference between the lowest and first-excited entanglement levels, is a useful quantity to determine

the boundary.

However, as far as phase transitions between magnetically ordered phases are concerned, we have found that the Schmidt gap is not necessarily a measure of phase transition. For example, the Schmidt gap cannot characterize phase transition between the FM and the 120° AFM phases, between zigzag-type AFM and IC1 phases, and between the IC1 and IC2 phases.

In one-dimensional quantum many-body systems, the Schmidt gap is known to be a novel quantity for identifying and characterizing various phases and phase transitions. In two-dimensional systems, however, the meaning of the Schmidt gap has not yet clarified as far as we know. Therefore, we consider that the present work will provide a starting point for the study of the relation between entanglement spectrum and quantum state in two dimensions. In fact, our present study of entanglement spectrum is closely related to other studies attempting unbiasedly to detect order parameters and/or dominant correlations using reduced density-matrices [158, 159]. We believe that we are able to extract much more information from the structure of entanglement and to identify and characterize various orders more efficiently, once we understand the nature of entanglement in many-body interacting systems.

Chapter 5

The Kitaev-Heisenberg model on the triangular lattice

Motivated by previous studies introduced in Sec. 2.4, in this chapter, we examine the KH model on the triangular lattice using DMRG. We then obtain the ground state phase diagram of the model in a fully quantum mechanical manner. As suggested by the previous studies [28, 29], we find six phases: a 120° AFM phase, a \mathbb{Z}_2 -vortex crystal phase, its dual counterpart, i.e., dual \mathbb{Z}_2 -vortex crystal phase, a nematic phase, a \mathbb{Z}_6 ferromagnetic (FM) phase, and its counterpart, i.e., dual FM phase. By calculating the spin structure factors for each spin component, we determine the magnetic structures. The spin structure factors exhibit discontinuous change at all the phase boundaries, and thus we conclude that all of the phase transitions are of first order. We find that the spin structure factors change their dominant spin component within \mathbb{Z}_6 FM phase (and dual FM phase) across the $SU(2)$ symmetric point, although there is no phase transition. This is due to the fact that quantum fluctuations removing the degeneracies of \mathbb{Z}_6 FM select a FM ordering with a dominant spin component. Furthermore, we investigate the von Neumann entanglement entropy of the model. As in the case of the spin structure factors, the entanglement entropy also discontinuously changes at all the phase boundaries. This is again due to the first-order phase transitions.

This chapter is organized as follows. In Sec 5.1, the KH model on the triangular lattice is introduced. The numerical condition of our DMRG simulations is also given. In Sec. 5.2, our results are shown. The phase diagram in the entire parameter space and physical properties are given. The spin structure factors in each phase and the entanglement spectrum of the KH model are discussed. Finally, in Sec. 5.3, the summary and outlook of this chapter are given.

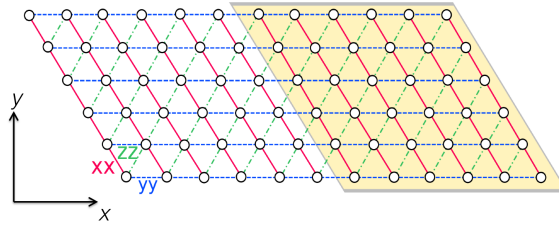


Figure 5.1: Triangular lattice with 12×6 sites. Red solid, blue dashed-dotted, and green dotted bonds labeled by xx , yy and zz have $S^x S^x$, $S^y S^y$ and $S^z S^z$ terms in a Kitaev model, respectively. A half of the system indicated by shaded orange is a subsystem to calculate the reduced density matrix in Sec. 5.2.3

5.1 Model and Method

In the triangular lattice, there are six bonds from a site. In the Kitaev term, each bond has one of the spin components of the nearest-neighbor spin-spin interaction, as shown in Fig. 5.1. The Hamiltonian of the KH model on a given nearest neighbor $\langle ij \rangle$ bond is, thus, given by

$$\mathcal{H}_{\langle ij \rangle}^{(\gamma)} = \left[J_K \hat{S}_i^\gamma \hat{S}_j^\gamma + J_H \hat{\mathbf{S}}_i \cdot \hat{\mathbf{S}}_j \right], \quad (5.1)$$

where $\hat{\mathbf{S}}_i$ is a vector of $SU(2)$ spin operator on site i , and γ represents a combination of spin component $\gamma \in \{x, y, z\}$ on the xx , yy and zz bonds, respectively. The first term is the Kitaev interaction that has $S^\gamma S^\gamma$ on the $\gamma\gamma$ bond on triangular lattice breaking $SU(2)$ spin rotation invariance. The second term is the usual Heisenberg interaction with $SU(2)$ spin symmetry. The total Hamiltonian of the KH model is given by $H_{\text{KH}} = \sum_{\langle ij \rangle} \mathcal{H}_{\langle ij \rangle}^{(\gamma)}$, summing all possible nearest-neighbor pairs.

We calculate the ground state of this model by using DMRG method [25, 113]. The DMRG calculations are carried out under both the cylindrical (i.e., periodic along xx -bond direction, but open along zz -bond direction) and the toroidal (i.e., periodic along both xx and zz -bond directions) boundary conditions. Unless otherwise noted, we use a system with 12 (along zz -bond) \times 6 (along xx -bond) sites, i.e., the 72-site lattice as shown in Fig. 5.1. To perform DMRG, we construct a snake-like one-dimensional chain along xx -bond, and combine the chain with long-range interactions. We keep $1300 \sim 1800$ states in the DMRG block and performed more than 10 sweeps, resulting in a typical truncation error 10^{-5} or smaller.

5.2 Results and Discussions

5.2.1 Phase diagram

For convenience, we take $J_K = \sin \theta$, $J_H = \cos \theta$ in (A.1) using an angle parameter θ ($\theta \in [0, 2\pi]$). Performing DMRG calculations for the 72-site lattice with the cylindrical boundary condition, we construct a phase diagram of the KH model as a function of θ . In Fig. 5.2(a), the ground-state energy per site, E , is plotted, and analyzing the energy, the ground-state phase diagram is obtained as shown in Fig. 5.2(d). The vertical dotted lines in Figs. 5.2(a)-(c) indicate the position of phase transitions determined by the peaks of the second derivative of E with respect to θ in Fig. 5.2(b). The boundaries coincide with the change of spin-spin correlation (not shown). We consider that all the phase transitions are of first order, since the spin-spin correlation discontinuously changes at the boundaries in spite of unclear discontinuity of the first derivative of energy. For example, although a singular behavior in $d^2E/d\theta^2$ is unclear at $\theta = 0.26\pi$, the spin-spin correlation changes discontinuously, and thus we judge that the first phase transition occurs at $\theta = 0.26\pi$.

The phases denoted in Fig. 5.2(a) are identified by the spin-spin correlation functions and the spin structure factors (see Sec. 5.2.2): they are a 120° AFM phase at $\theta = 0$, a \mathbb{Z}_2 -vortex crystal phase for $-0.15\pi < \theta < 0.25\pi$, its dual counterpart, i.e., dual \mathbb{Z}_2 -vortex crystal phase for $0.62\pi < \theta < 0.7\pi$, a nematic phase for $0.25\pi < \theta < 0.62\pi$, a \mathbb{Z}_6 ferromagnetic (FM) phase for $0.7\pi < \theta < 1.5\pi$, and its counterpart, i.e., dual FM phase for $1.5\pi < \theta < 1.85\pi$. The phases are fully consistent with previous studies [28, 29], and no new phase was found at least for systems up to 72 sites.

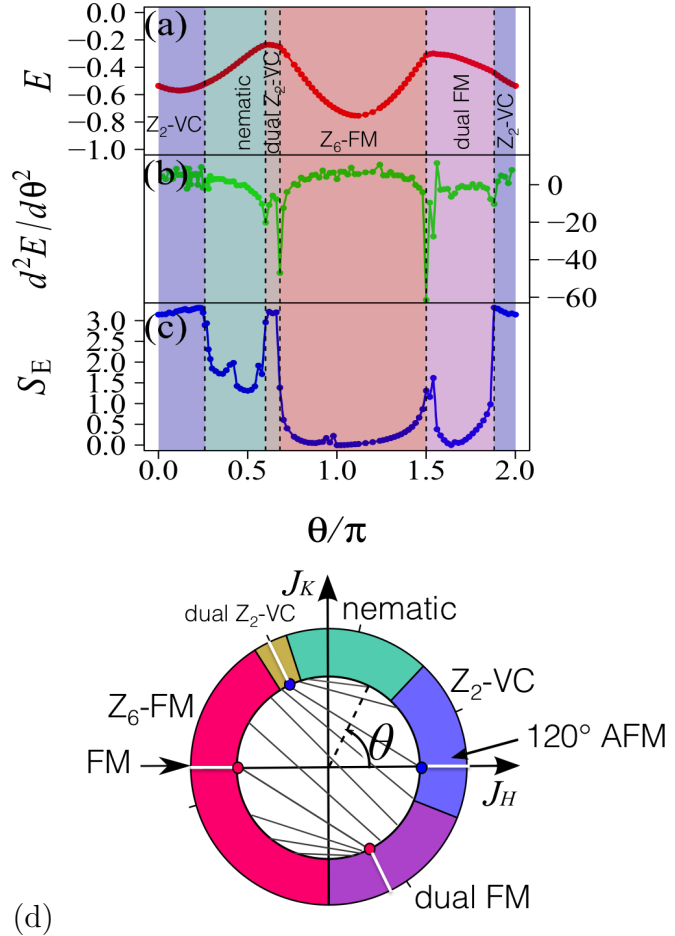


Figure 5.2: (a) The ground-state energy per site, E , of the KH model in Eq. (A.1) (red plots) obtained by DMRG for a 12×6 -site lattice with the toroidal boundary conditions. There are a 120° AFM phase (only at $\theta=0$), \mathbb{Z}_2 vortex crystal phase (\mathbb{Z}_2 VC) and its dual phase (dual \mathbb{Z}_2 VC), a nematic phase (nematic), a \mathbb{Z}_6 ferromagnetic phase (\mathbb{Z}_6 FM) and its dual phase (dual FM). (b) The second derivative of E with respect to θ , $d^2E/d\theta^2$ (green plots). (c) The entanglement entropy (blue plots) for a 12×6 -site lattice with the cylindrical boundary conditions. The vertical dotted lines denote the phase boundary determined by the second derivative of E . (d) Phase diagram of the KH model in Eq. (A.1). The circle parametrization of $J_H = \cos \theta$ and $J_K = \sin \theta$ is used. Green lines inside the inner circle connect parameter space related by the Klein duality. Filled blue and red circles on the inner circle show parameter points with $SU(2)$ spin-rotational symmetry.

5.2.2 Spin structure factors

Next, we discuss the magnetic phases in the phase diagram in detail. We calculate the spin structure factors for each spin component given by

$$S^{\gamma\gamma}(\mathbf{q}) = \sum_{l=0}^{N-1} \langle \hat{S}_0^\gamma \hat{S}_l^\gamma \rangle \cos(\mathbf{q} \cdot \mathbf{r}_l),$$

$$S(\mathbf{q}) = \sum_{\gamma=x,y,z} S^{\gamma\gamma}(\mathbf{q}), \quad (5.2)$$

where N is the number of total sites, and \mathbf{r}_l denotes the position of l -th site, and $\mathbf{q} = (q_x, q_y)$ is wave number defined in the first Brillouin zone (BZ). To calculate spin structure, we use the toroidal boundary condition for the 72-site lattice.

120° AFM and \mathbb{Z}_2 -vortex crystal phases

First, we examine the magnetic structures of the 120° AFM ordered phase ($\theta = 0$) and the \mathbb{Z}_2 -vortex crystal phase ($-0.15\pi < \theta < 0.25\pi$). Figure 5.3 shows the spin structure factors at $\theta = 0$, where the results in the half of the first BZ are plotted and the radius of colored circles represents the intensity of the structure factors. Because of $SU(2)$ symmetry, the three components, $S^{xx}(\mathbf{q})$, $S^{yy}(\mathbf{q})$, and $S^{zz}(\mathbf{q})$ are equivalent to each other. The largest intensity appears at the K points in the first BZ, corresponding to 120° AFM order.

When the Kitaev couplings are introduced, the $SU(2)$ symmetry is broken, which will lead to an anisotropic behavior in the spin structure factors. Such a behavior is actually found in Fig. 5.4, where $\theta = 0.16\pi$. It is clear that $S^{yy}(\mathbf{q})$ and $S^{zz}(\mathbf{q})$ in Figs. 5.4(b) and 5.4(c), respectively, show nonequivalent intensity at the momentum points, A and B (see the figures), where the structure factors are exactly the same at $\theta = 0$ with $SU(2)$ symmetry. On the other hand, $S^{xx}(\mathbf{q})$ exhibits the same intensity at the A and B points. This implies that two of three spin components are asymmetric with respect to the symmetric line connecting the Γ point ($\mathbf{q} = (0, 0)$) and the middle of two equivalent K points, i.e., the M point. More precisely, we find that $S^{yy}(\mathbf{q})$ is larger at A than at B, and vice versa for $S^{zz}(\mathbf{q})$, i.e., $(S^{yy}, S^{zz}) = (0.47, 0.79)$ at A and $(S^{yy}, S^{zz}) = (0.79, 0.47)$ at B. This tendency is also true, for example, at $\theta = 0.08\pi$, where $(S^{yy}, S^{zz}) = (0.53, 0.67)$ at A and $(S^{yy}, S^{zz}) = (0.67, 0.53)$ at B.

The asymmetry with respect to the Γ -M line is consistent with the spin structure factor proposed for the \mathbb{Z}_2 -vortex crystal phase [28, 29], where an

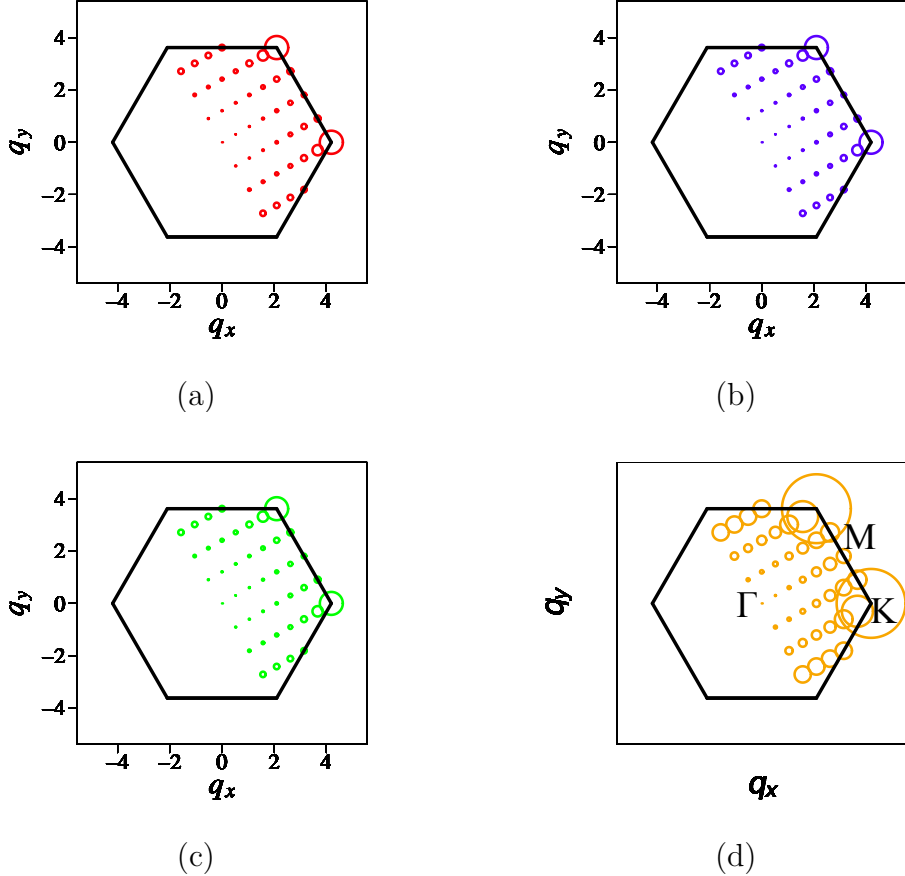


Figure 5.3: Spin structure factors at $\theta = 0$ (120° AFM phase) for a 12×6 -site lattice with the toroidal boundary conditions. (a) $S^{xx}(\mathbf{q})$, (b) $S^{yy}(\mathbf{q})$, (c) $S^{zz}(\mathbf{q})$, and (d) $S(\mathbf{q})$. The radius of the circles represents the intensity of the structure factors at the momentum point defined by the lattice. The results in the half of the first BZ are plotted.

ordering wave vector shifts from the K points with accompanying secondary Fourier components away from K . As a result, a finite Kitaev coupling breaks the 6-fold rotational symmetry of $S^{xx}(\mathbf{q})$, $S^{yy}(\mathbf{q})$, and $S^{zz}(\mathbf{q})$ around the Γ point down into the 2-fold rotational symmetry, although the 6-fold rotational symmetry remains in $S(\mathbf{q}) = S^{xx}(\mathbf{q}) + S^{yy}(\mathbf{q}) + S^{zz}(\mathbf{q})$.

Nematic phase

It has been suggested that there appears a nematic phase around $\theta = 0.5\pi$ [28, 29]. Compared with the phase diagram obtained by exact diagonalization method for the 24-site cluster [29], the region of nematic phase is extended, implying the stability of the nematic phase in the thermodynamic limit. The magnetic order in the nematic phase is known to be AFM Ising-chain-type with

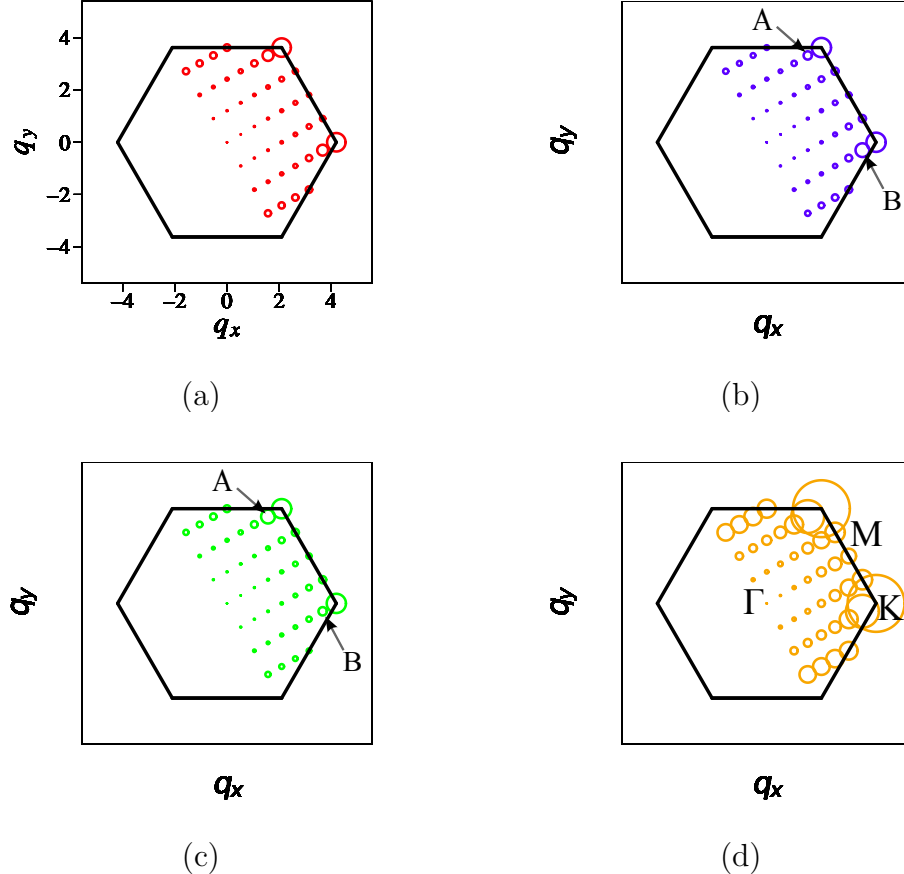


Figure 5.4: Same as Fig. 5.3, but for $\theta = 0.16\pi$ in \mathbb{Z}_2 vortex crystal phase. The symbols A and B in (b) and (c) denote the momenta where an asymmetric behavior with respect to the Γ -M line is clearly seen.

x , y , or z spin component along one of the lattice directions [28]. Since other directions are disconnected in terms of the given spin component, flipping all spins of the Ising chain does not change the energy. This leads to sub-extensive degeneracy of the ground state, which is related to intermediate symmetry lying midway between global symmetries and local gauge symmetries [29, 108]. The intermediate symmetry and dimensional reduction are discussed in the compass model, indicating that a higher dimensional spin system decouples into lower dimensional subsystems. The low-energy states are ordered along only one direction in the system with intermediate symmetry, leading to the degeneracy. Such degeneracy can be lifted by thermal or quantum fluctuations through the so-called order by disorder mechanism [108]. Such a partial order composed of decoupled chains also appears in the compass model on the square lattice.

In the nematic phase at $\theta = 0.5\pi$, i.e., the AFM Kitaev point, it has

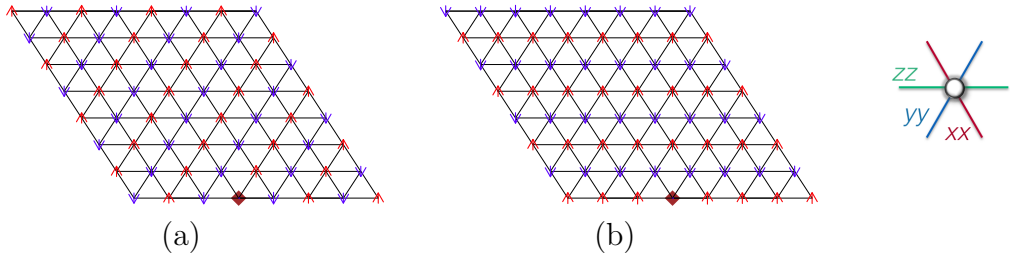


Figure 5.5: $\langle S_i^x S_j^x \rangle$ for the nematic phase at $\theta = 0.5\pi$ in an 8×8 lattice with the toroidal boundary conditions. The energies of (a) and (b) are degenerate. The site i is indicated by a brown rhombus point. Upward red arrows and downward blue arrows show positive and negative values of spin-spin correlation, respectively. The length of the arrows represents the strength of spin-spin correlation. The x component of spins aligns antiferromagnetically and ferromagnetically along the horizontal direction of the lattice in (a) and (b), respectively.

been pointed out that the AFM correlation between next-nearest-neighbor chains, which locks the next-nearest-neighbor spin alignment, reduces the sub-extensive degeneracy of the ground state from 3×2^L to nonextensive value 3×2^2 , where L denotes the total number of chains [29]. This results has been based on DMRG calculations with three-leg and four-leg triangular ladders for L up to 14 [29]. We have confirmed this reduction of the degeneracy to 3×2^2 for a 6×4 lattice. In order to obtain the 2^2 -fold degeneracy for one component, we apply a small external magnetic field at two sites on neighboring chains to force the direction of the neighboring spins to be parallel or antiparallel, and find that the energies of the two cases give the same energy within the numerical accuracy. In contrast to the degeneracy seen in the 6×4 lattice, we find that a larger system of 12×6 does not show such degeneracy: the energy with antiparallel spin alignment for the neighboring chains is always lower than that with parallel spin alignment forced by a small magnetic field. This is probably due to anisotropic geometry of the 12×6 lattice as compared with 6×4 , resulting in the AFM alignment of a given component of spins along the horizontal direction of the 12×6 lattice.

In order to reduce this anisotropic geometry, we additionally examine an isotropic 8×8 lattice under the toroidal boundary conditions. As expected, we find degenerate ground states with the same energy by applying a small magnetic field. Figure 5.5 shows the spin-spin correlation function for the x component between sites i and j of the 8×8 lattice, given by $\langle S_i^x S_j^x \rangle = \langle 0 | \hat{S}_i^x \hat{S}_j^x | 0 \rangle$, where $|0\rangle$ is the ground-state wave function and the site i is chosen

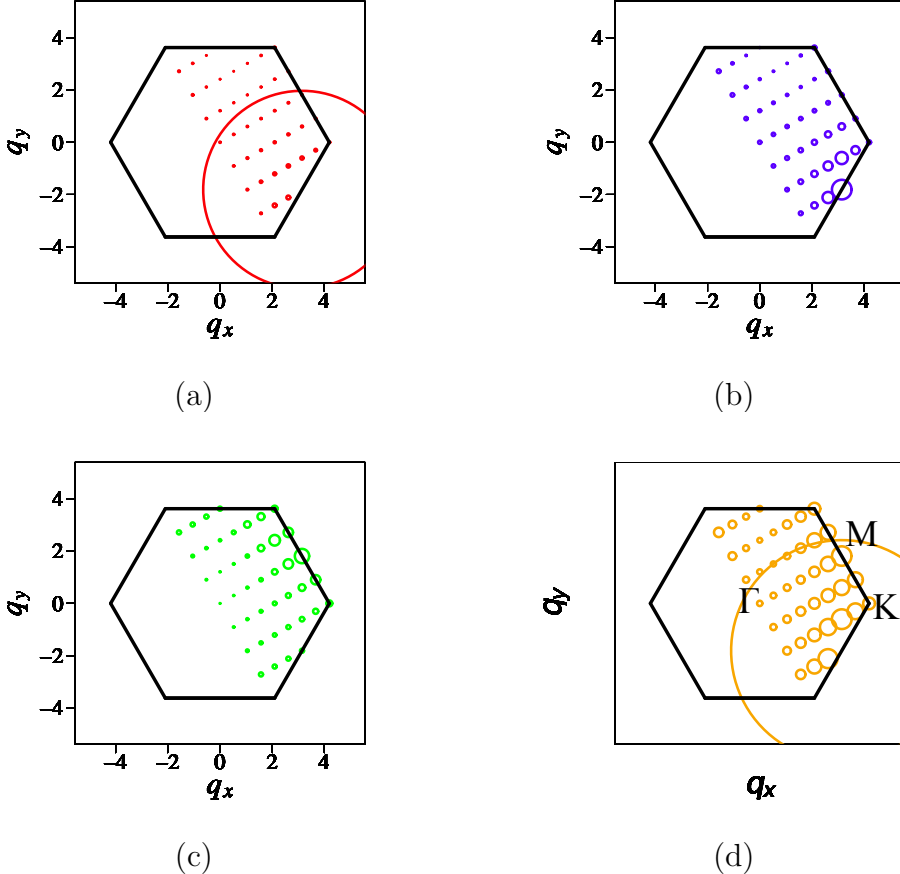


Figure 5.6: Same as Fig. 5.3, but for $\theta = 0.48\pi$ in nematic phase. The center of a large circle in (a) and (d) is located at the M point with negative q_y .

to be the site denoted by rhombus in the figure. In Fig. 5.5(a), we notice that the x component forms a chain-wise AFM order along the xx -bond direction (see Fig. 5.1) and that any pair of closest sites on next-nearest-neighbor chains exhibit the AFM alignment of the x component. These features are the same as Fig. 5.5(b), but the alignment between nearest-neighbor chains is different. In other words, the x component of spins aligns antiferromagnetically along the horizontal direction of the 8×8 lattice in Fig. 5.5(a) but ferromagnetically in 5.5(b). This is consistent with the presence of 3×2^2 -fold degeneracy.

Away from the AFM Kitaev point, it has been pointed out that the degeneracy is further reduced to 3×2 [29] even in the nematic phase. When AFM Heisenberg interaction is added within the nematic phase, i.e., $\theta < 0.5\pi$, it is expected that the ground state with AFM spin alignment between the nearest-neighbor chains such as the one shown in Fig. 5.5(a) will be picked up. The 12×6 lattice actually has such a ground state. The spin structure factors for $\theta = 0.48\pi$ are shown in Fig. 5.6, where the x component is selected in contrast

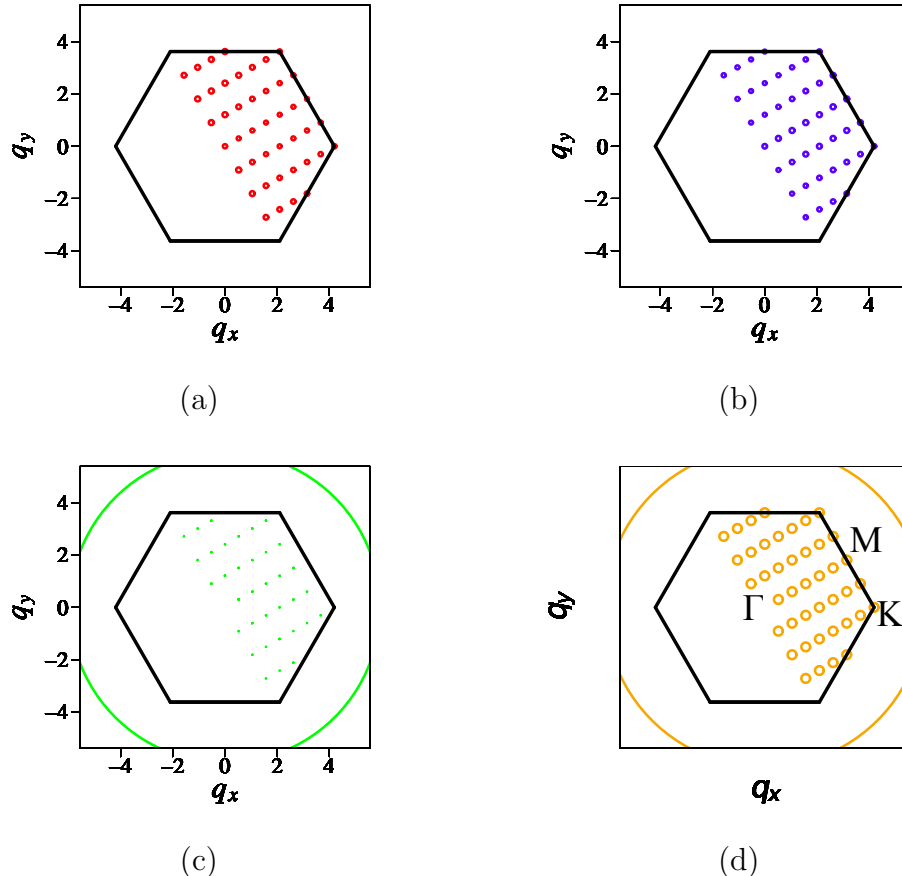


Figure 5.7: Same as Fig. 5.3, but for $\theta = 0.88\pi$ in \mathbb{Z}_6 FM phase. The center of a large circle in (c) and (d) is located at the Γ point.

to other components. The $S^{xx}(\mathbf{q})$ shows the largest value at the M point with negative q_y as expected from the spin structure as shown in Fig. 5.5(a).

\mathbb{Z}_6 ferromagnetic phase

The FM phase is extended from $\theta = 0.68\pi$ to 1.50π . The Heisenberg FM point is at $\theta = \pi$, where the Hamiltonian is $SU(2)$ symmetric and the spin structure factors are equal for the x , y , and z components. The FM phase with finite Kitaev coupling is called \mathbb{Z}_6 FM [29]. Although the order parameter for the $SU(2)$ -symmetric systems takes its value on the whole unit sphere, the Kitaev coupling discretizes it to \mathbb{Z}_6 . Quantum fluctuations are expected to select one of the FM spin configurations out of the \mathbb{Z}_6 space. In our DMRG calculations, the z (x) component of spin configurations is selected when $0.68\pi < \theta < \pi$ ($\pi < \theta < 1.50\pi$). For example, at $\theta = 0.88\pi$ ($\theta = 1.04\pi$) $S^{zz}(0, 0)$ ($S^{xx}(0, 0)$) shows the largest intensity as shown in Fig. 5.7 (Fig. 5.8).

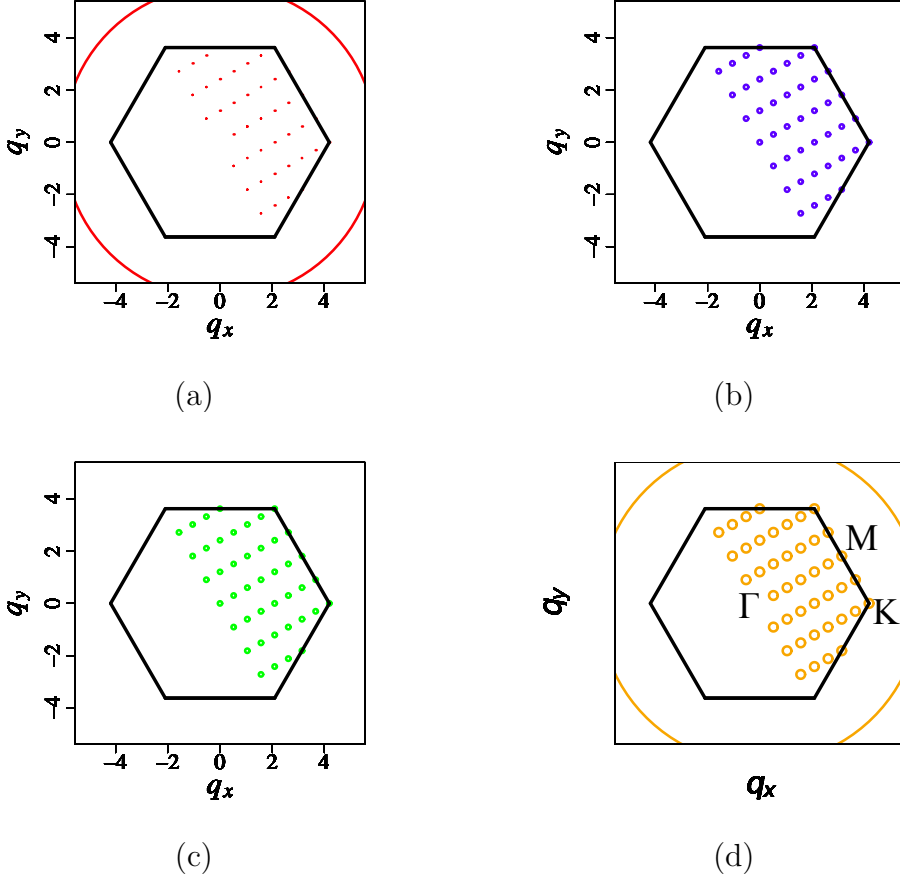


Figure 5.8: Same as Fig. 5.3, but for $\theta = 1.04\pi$ in \mathbb{Z}_6 FM phase. The center of a large circle in (a) and (d) is located at the Γ point.

Duality

It is well-known that there is the Klein duality on the parameter space of the KH model, which is given by $J_H \rightarrow -J_H$ and $J_K \rightarrow 2J_H + J_K$ as shown in Fig. 5.2(d) [22]. The duality is accompanied by the spin rotations depending on sublattices [2]. Accordingly, the two explicit $SU(2)$ -symmetric points at $\theta = 0$ (AFM Heisenberg limit) and $\theta = \pi$ (FM Heisenberg limit) give two hidden $SU(2)$ -symmetric points at $\theta_0 = \arctan(-2) = 0.64758\pi$ and $\theta_\pi = \pi + \arctan(-2) = 1.64758\pi$, respectively.

Around θ_0 , we find the dual \mathbb{Z}_2 -vortex crystal phase ($0.6\pi < \theta < 0.7\pi$) as shown in Fig. 5.2. The structure factors at $\theta = 0.64\pi$ are shown in Fig. 5.9. As in the case of the \mathbb{Z}_2 -vortex crystal phase (see Fig. 5.4), $S^{yy}(\mathbf{q})$ and $S^{zz}(\mathbf{q})$ are asymmetric with respect to the Γ -M line, but symmetric in $S^{xx}(\mathbf{q})$.

The dual FM phase, corresponding to the \mathbb{Z}_6 FM at $0.68\pi < \theta < 1.50\pi$, is located at $1.50\pi < \theta < 1.88\pi$. Figures 5.10 and 5.11 exhibit the spin structure

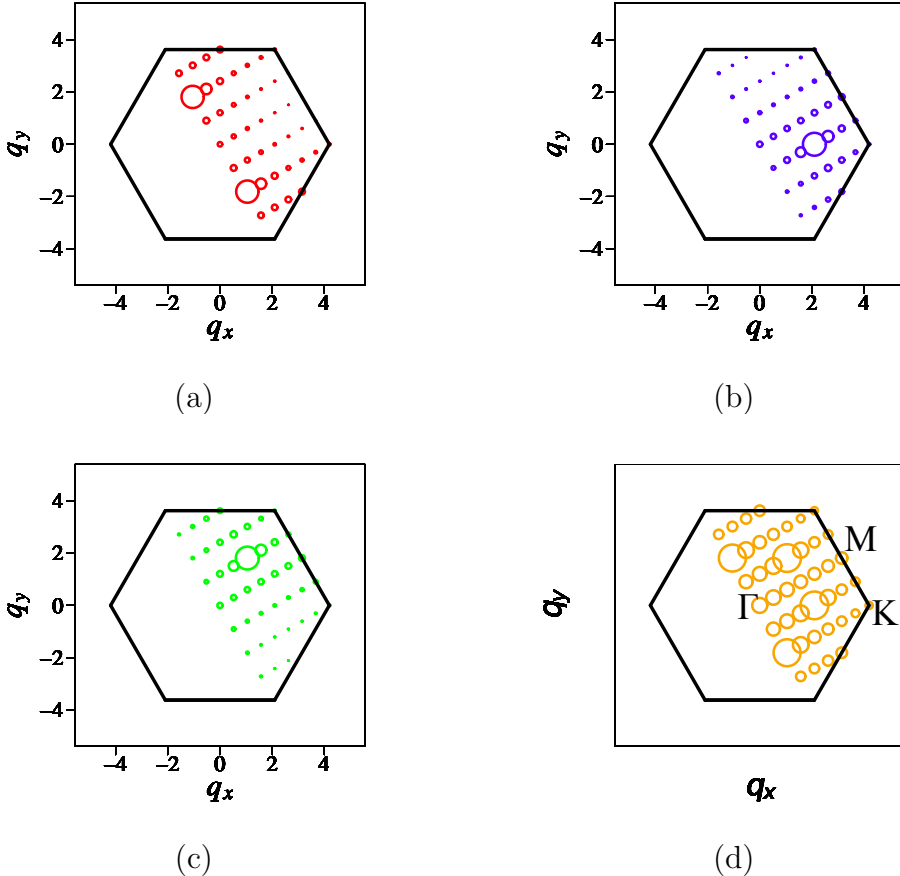


Figure 5.9: Same as Fig. 5.3, but for $\theta = 0.64\pi$ in dual \mathbb{Z}_2 vortex crystal phase.

factors at $\theta = 1.58\pi$ and $\theta = 1.70\pi$, respectively. $S^{xx}(\mathbf{q})$ becomes stripe-type with the largest intensity at the M point with $q_y > 0$ in Fig. 5.10, while $S^{zz}(\mathbf{q})$ becomes largest at another M point with $q_y < 0$ in Fig. 5.11. The difference of spin component of the two cases is understood by considering the spin rotations [29]: When the x (z) component of spin is ferromagnetically ordered, the dual phase becomes a stripe-type AFM phase where x (z) component is ordered. However, the direction of these strips, i.e., the direction of FM chains, are different from each other by angle $\pi/3$.

5.2.3 Entanglement entropy and entanglement spectrum

Figure 5.2(c) shows the θ dependence of the entanglement entropy. At phase transition points, the entanglement entropy discontinuously changes. We note that the slight deviation of the discontinuity from $\theta = 1.5\pi$ is due to finite-size and/or boundary effects, since we obtain the discontinuity at $\theta = 1.5\pi$ for the toroidal boundary conditions (not shown). The discontinuous

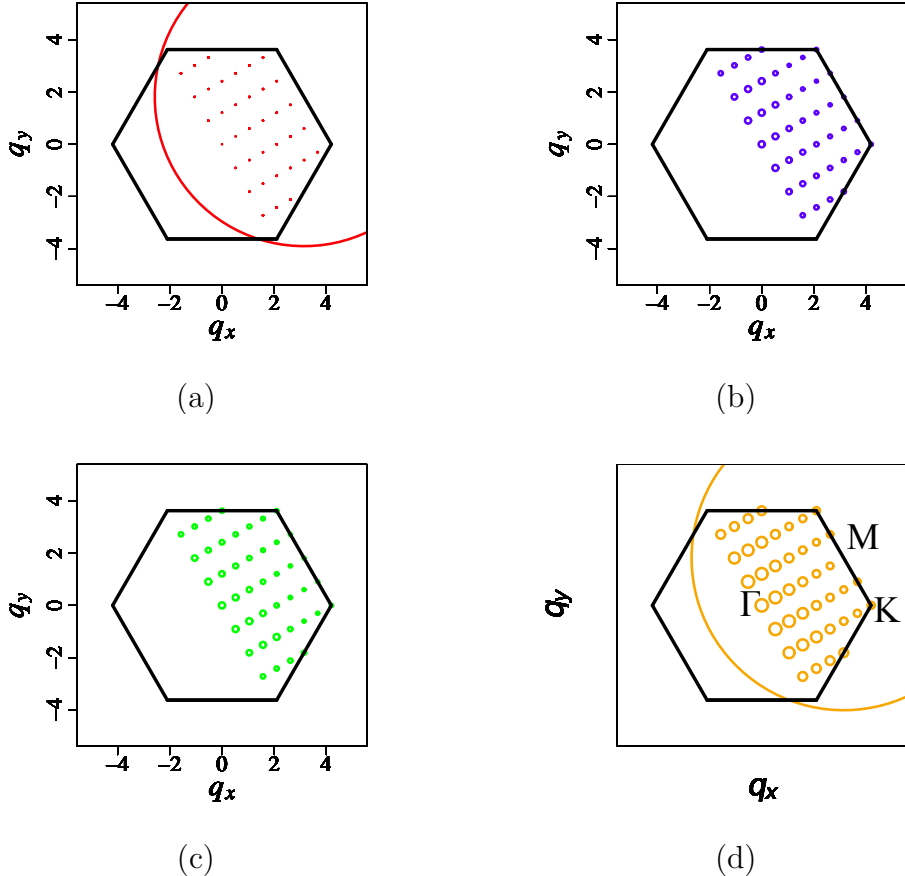


Figure 5.10: Same as Fig. 5.3, but for $\theta = 1.58\pi$ in dual \mathbb{Z}_6 FM phase. The center of a large circle in (a) and (d) is located at the M point.

change is simply due to the fact that all phase transitions appeared in the KH model on the triangular lattice are of first order. At first-order phase transition points, the ground state suddenly changes to another state with different entanglement.

The entanglement spectrum ξ_i is shown in Fig. 5.12, where the low-lying entanglement levels are plotted from the smallest value starting from $i = 1$. The spectral distribution of the entanglement spectrum changes with changing parameter θ . In the case of the KH model on the honeycomb lattice, the degeneracy of entanglement spectrum has been found in the Kitaev spin-liquid phase, which is due to the intrinsic nature of Kitaev spin liquid [151]. In the case of the triangular lattice, however, there is no such a spin liquid phase, and thus the degeneracy of entanglement spectrum is not found except at phase transition points. To locate the phase transition points using the entanglement spectrum, we consider the Schmidt gap $\xi_2 - \xi_1$, where ξ_1 and ξ_2 are the lowest and second lowest levels of the entanglement spectrum, respectively. In

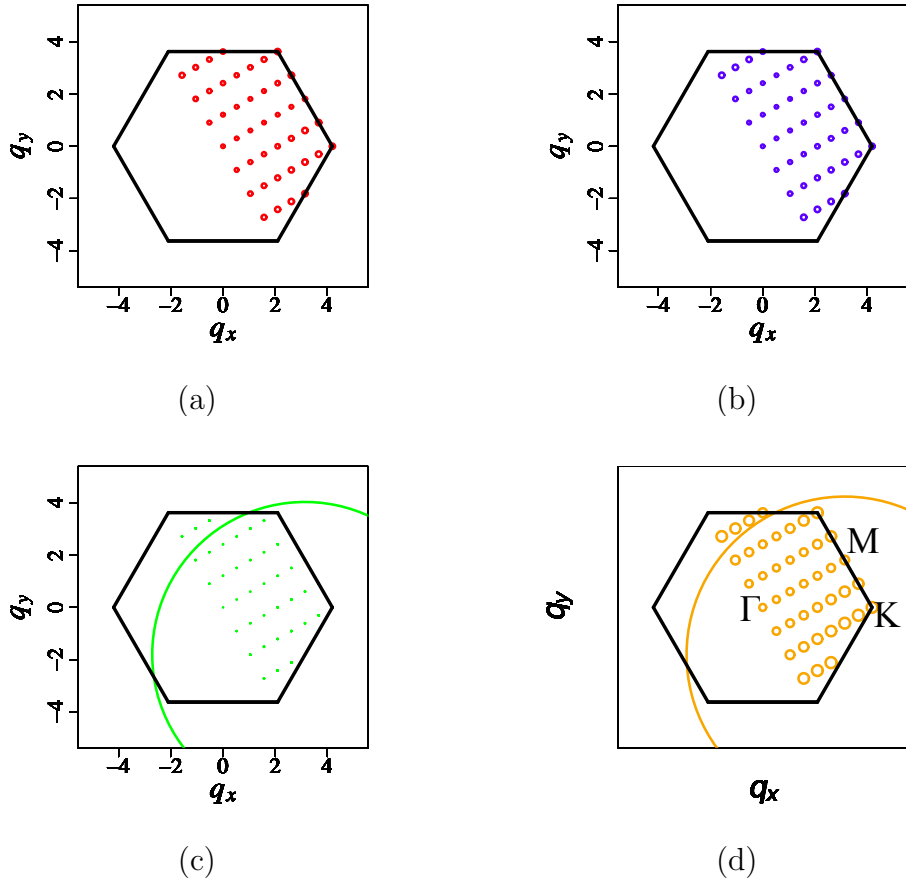


Figure 5.11: Same as Fig. 5.3, but for $\theta = 1.70\pi$ in dual \mathbb{Z}_6 FM phase. The center of a large circle in (a) and (d) is located at the M point with negative q_y .

contrast to the KH model on the honeycomb lattice, the Schmidt gap in each phase is clearly larger than other gaps in the higher levels. This implies that the lowest entanglement level ξ_1 is well separated from the other levels and thus predominately contributes to the ground-state wave function of the total system. The Schmidt gap is closing at the phase boundaries, where the eigenstates of entanglement spectrum cross and exchange each other. The crossing appears only near the boundaries, since the ground state changes to other states with first-order phase transitions. Therefore, the Schmidt gap shows a singularity at phase transition points in the KH model on the triangular lattice.

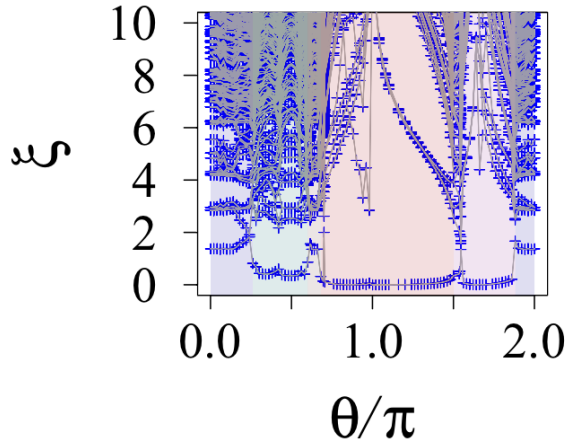


Figure 5.12: The entanglement spectrum for the KH model (A.1) on the triangular lattice. Blue pluses represent entanglement levels and black lines connect the spectrum belonging to the same entanglement levels.

5.3 Summary and Outlook

We have studied the KH model on the triangular lattice by using DMRG and constructed the full-parameter ground state phase diagram. We have used a large cluster with 12×6 sites, and found the 120° AFM phase, \mathbb{Z}_2 vortex crystal phase, dual \mathbb{Z}_2 vortex crystal phase, nematic phase, \mathbb{Z}_6 FM phase, and dual FM phase, in good quantitative agreement with the previous studies [28, 29]. The magnetic structures of these phases have been determined by calculating the spin structure factors for each spin component. The spin structure factors suddenly change at all phase boundaries, and thus we conclude that all phase transitions are of first order.

In the \mathbb{Z}_6 FM phase and its dual FM phase, we have found that the spin structure factors change at the $SU(2)$ symmetric points $\theta = \pi$ and $\theta = 1.64\pi$, respectively. There are no phase transitions, but the major axis of ordering changes. Since the \mathbb{Z}_6 FM phase is generally 6-fold-degenerate, one of them will be picked up by external conditions. In the geometry of our 12×6 -site lattice, the FM orderings with different dominant axes are selected depending on θ across the $SU(2)$ points.

In the \mathbb{Z}_2 -vortex crystal phase, the spin structure factors of y and z spin components become asymmetric with respect to the Γ -M line, as expected from the previous studies [28, 29].

The entanglement entropy drastically changes at all phase boundaries, as is expected from the first order transitions. This is in contrast to the extended KH model on the honeycomb lattice discussed in the previous chapter,

where the topological spin liquid phase exists. By examining the entanglement spectrum, we have found that the Schmidt gap is much larger than the other entanglement gaps. This implies that the lowest entanglement level is crucial for describing the ground-state wave function of the whole system. At the phase transition points, the Schmidt gap closes, and therefore the change of the entanglement structure is clear in the KH model on the triangular lattice.

We have confirmed exotic magnetic phases proposed in the previous studies on the triangular KH model [28, 29]. It is thus interesting to investigate the presence of such phases in a possible candidate material $\text{Ba}_3\text{IrTi}_2\text{O}_9$ [30]. In particular, our results of spin structure factors $S^{\gamma\gamma}(\mathbf{q})$ could be useful for analyzing polarized neutron scattering data that will be taken in the near future.

Chapter 6

Conclusions

Quantum spin systems show various phases, since there are many kinds of lattice structures. Spin frustration due to the further neighbor interactions and geometries of lattice structure puts the system away from the classical limit, and thus a lot of states compete with each other, resulting in a non-trivial ground state. The effect of frustration has been enthusiastically studied for long time, and various phases have been found. Very recently, the Kitaev model and its candidate material Na_2IrO_3 have been proposed as a new playground of quantum spin systems. Therefore, it is important to study quantum spin systems with the Kitaev-type anisotropic interaction in order to search non-trivial ground states.

In order to clarify the role of the Kitaev-type anisotropic interactions in quantum spin systems, we have studied the Kitaev-Heisenberg (KH) model and its extension. We adopted the density-matrix renormalization group (DMRG) method, since the method is one of the most powerful methods currently available for studying two-dimensional systems. We have focused on Na_2IrO_3 with the honeycomb-lattice structure and $\text{Ba}_3\text{IrTi}_2\text{O}_9$ with the triangular-lattice structure. The spin exchange interaction of these materials is dominated by the Kitaev interaction due to the strong spin-orbit interaction in the $5d$ compounds. Thus, these two materials give a strong motivation for the study on quantum spin systems with the Kitaev-type anisotropic interaction. To understand the physics of these materials, we have studied the extended KH model on the honeycomb lattice for Na_2IrO_3 and the KH model on the triangular lattice for $\text{Ba}_3\text{IrTi}_2\text{O}_9$. These results are summarized below for completion of this thesis.

In the case of the honeycomb lattice, we have investigated the extended KH model as an effective spin model for Na_2IrO_3 that takes into account the Ir-Ir direct electron hoppings and the trigonal distortion present in Na_2IrO_3 . The

CHAPTER 6. CONCLUSIONS

KH model is too simple to explain the zigzag antiferromagnetic (AFM) order that has been observed in experiments. As a result, we found that the extended KH model naturally explains the zigzag AFM order. In order to obtain the zigzag AFM order, the off-diagonal interaction due to the trigonal distortion plays an important role. The Kitaev spin-liquid state is not the ground state of Na_2IrO_3 , but the spin-liquid phase lies next to the zigzag AFM phase realized in Na_2IrO_3 . Other than the zigzag AFM phase, we have also found the 120° AFM, FM, and two kinds of incommensurate phases next to the spin-liquid phase.

In the case of the triangular lattice, we have investigated the KH model that is expected to describe the physics of $\text{Ba}_3\text{IrTi}_2\text{O}_9$. The KH model on the triangular lattice has been derived from the original KH model on the honeycomb lattice. The mechanism of the relevant Kitaev interaction in $\text{Ba}_3\text{IrTi}_2\text{O}_9$ is qualitatively the same as in Na_2IrO_3 . However, there is geometrical spin frustration due to the triangular lattice structure. Thus, the model is no longer solvable even at the Kitaev limit point, leading to the highly non-trivial quantum phase diagram. By performing DMRG, we found the 120° AFM phase, \mathbb{Z}_2 -vortex crystal phase, dual \mathbb{Z}_2 -vortex crystal phase, nematic phase, \mathbb{Z}_6 FM phase, and its dual phase, which is consistent with the previous studies. Instead of a spin-liquid phase, we found the nematic phase around the AFM Kitaev limit point. The ground-state phase diagrams of the KH models on the honeycomb and triangular lattices are completely different.

Furthermore, we have examined the entanglement entropy and entanglement spectrum of these models that are easily calculated by using DMRG. Although the two quantities do not necessarily show anomaly or jumps at phase boundaries in general, the KH model on the triangular lattice shows the change at the boundaries. This may be because the phase transition of the KH model is the first-order phase transition among the phases with different structure of entanglement.

In contrast to the triangular lattice, the change of the entanglement entropy and entanglement spectrum of the extended KH model on the honeycomb lattice is obscure. Thus, it is hard to characterize phase boundaries by using them. However, we have found the special nature of the entanglement spectrum of the Kitaev spin liquid, where a degenerate structure emerges in the Kitaev spin-liquid phase. This is due to the special nature of the Kitaev model related to its exact-solvability. In contrast, there is no degeneracy in the magnetically ordered phase. Therefore, by using this property, phase transitions between the Kitaev spin-liquid state and magnetically ordered states are well characterized by the entanglement spectrum. We thus conclude that

CHAPTER 6. CONCLUSIONS

the entanglement spectrum characterizes the phase boundary of the Kitaev spin-liquid state, in addition to the Kitaev spin liquid state itself.

We have made clear the effect of the Kitaev interaction on quantum spin systems by investigating ground-state properties of the (extended) KH model on the honeycomb and triangular lattices. We have performed high-performance computer simulations based on DMRG. The quantum spin systems with the Kitaev anisotropic interaction are expected to be relevant to iridate-oxide materials. Thus, our study contributes to the understanding of the magnetic properties in Na_2IrO_3 and $\text{Ba}_3\text{IrTi}_2\text{O}_9$. Furthermore, we have examined the entanglement properties of the models. The study of the Kitaev physics in quantum spin systems should be pushed forward strongly. We hope that our study can make a bridge among condensed matter physics, quantum informational science, material science, and computational science.

Appendix A

Entanglement Spectrum

In order to make clear the implications of entanglement spectrum in two-dimensional quantum spin systems, we examine entanglement spectrum of the KH model whose ground state is well known.

Kitaev-Heisenberg model

In this section, we defined the KH model as

$$\mathcal{H} = \sum_{\langle i,j \rangle} [-2\alpha S_i^\gamma S_j^\gamma + (1-\alpha) \mathbf{S}_i \cdot \mathbf{S}_j], \quad (\text{A.1})$$

where α is related to J_K and J_H in Eq. (2.38) as $J_H = 1 - \alpha$ and $J_K = -2\alpha$. The ground state at $\alpha = 0$ and $\alpha = 1$ is the Néel and Kitaev spin-liquid state, respectively. In between, there is a strpye-type AFM state.

Figure A.1 shows entanglement spectrum of the 8×6 -site KH model with periodic boundary conditions as a function of α . Hereafter, we call periodic boundary condition toroidal boundary condition. We find that level structure changes at $\alpha \simeq 0.4$ and $\alpha \simeq 0.86$. These values are consistent with phase transition points determined by the second derivative of energy with respect to α .

We find that the Kitaev spin-liquid phase exhibits 4-fold degeneracy in the ground state while the Néel and strpye phases show non-degenerate lowest energy level. The degeneracy of the spin-liquid phase comes from its gauge structure as will be discussed in this Appendix

The Schmidt gap increases drastically at $\alpha \simeq 0.4$ with increasing α . This indicates that a phase transition occurs there. At exactly solvable point $\alpha = 0.5$, the gap diverges, since the ground state can be written by a single product state. With further increasing α , the Schmidt gap closes between $\alpha = 0.85$ and

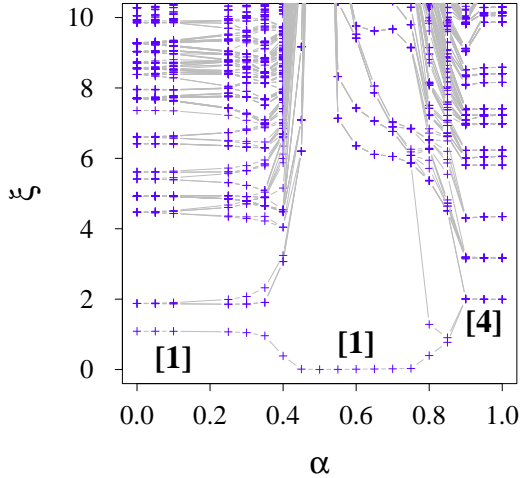


Figure A.1: Entanglement spectrum for the KH model (A.1). Blue crosses represent entanglement levels and gray lines connect the spectrum belonging to the same entanglement levels. $[n]$ in (b) denotes n -fold degeneracy of the lowest entanglement level in each phase.

9.0. This is again consistent with the position of phase boundary. Of course, in order to determine phase boundary precisely, it is important to study finite-size scaling of Schmidt gap.

Kitaev Spin-Liquid State

In this section, we discuss the dependence of entanglement spectrum in the Kitaev spin-liquid state on system size and boundary condition.

First of all, we consider the degeneracy of entanglement spectrum for a $L_x \times 6$ ($L_x \rightarrow \infty$) system by counting the Wilson loops that are cut when the whole system is divided into two subsystems [1, 85, 160]. In our cluster configuration, it is inevitable to have two Wilson loops, for example, W_1 and W_2 defined on two neighboring hexagons as shown in Fig. A.2. The two loops induce 2-fold degeneracy. The number of degeneracy increases as the number of Wilson loop defined on honeycomb lattice increases. We can define more Wilson loops in toroidal boundary condition than in cylindrical boundary condition.

Let us briefly confirm this. Figure A.2 shows a 8×6 -site system, where the number labels sites on honeycomb lattice and vertical lines denote cutting position when we divide the whole system into two subsystems to calculate entanglement spectrum. Note that a system with toroidal boundary condition is cut twice at a middle vertical line and a right or left line, while a system with cylindrical boundary condition is cut only once at middle vertical line. Firstly,

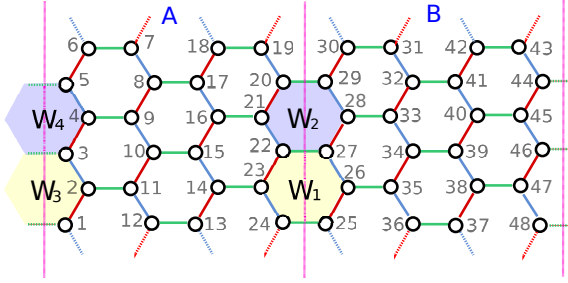


Figure A.2: Cluster configuration of 8×6 sites. The numbers label sites on honeycomb lattice. Vertical dashed lines denote cutting position when we divide the whole system into two subsystems, A and B. For cylindrical boundary condition the system is divided only once at the middle vertical line, while for toroidal boundary condition the system is cut twice at the middle vertical line and the right or left vertical line. W_1 and W_2 show the Wilson loops defined on hexagon on honeycomb lattice, which cross the middle vertical line. W_3 and W_4 show the loops that cross the right or left vertical line.

we consider the case of cylindrical boundary condition. Then, the system is divided into A and B parts. We define the Wilson loops

$$\begin{aligned}\hat{W}_1 &= \hat{\sigma}_{24}^y \hat{\sigma}_{23}^z \hat{\sigma}_{22}^x \hat{\sigma}_{27}^y \hat{\sigma}_{26}^z \hat{\sigma}_{25}^x \\ &= \hat{w}_1^A \hat{w}_1^B, \\ \hat{W}_2 &= \hat{\sigma}_{22}^y \hat{\sigma}_{21}^z \hat{\sigma}_{20}^x \hat{\sigma}_{29}^y \hat{\sigma}_{28}^z \hat{\sigma}_{27}^x \\ &= \hat{w}_2^A \hat{w}_2^B,\end{aligned}$$

where σ_i^x , σ_i^y and σ_i^z are Pauli matrices at i -site and

$$\begin{aligned}\hat{w}_1^A &= \hat{\sigma}_{24}^y \hat{\sigma}_{23}^z \hat{\sigma}_{22}^x, \\ \hat{w}_1^B &= \hat{\sigma}_{27}^y \hat{\sigma}_{26}^z \hat{\sigma}_{25}^x, \\ \hat{w}_2^A &= \hat{\sigma}_{22}^y \hat{\sigma}_{21}^z \hat{\sigma}_{20}^x, \\ \hat{w}_2^B &= \hat{\sigma}_{29}^y \hat{\sigma}_{28}^z \hat{\sigma}_{27}^x.\end{aligned}$$

Note that commutation relation

$$[\hat{W}_1, \hat{W}_2] = 0 \tag{A.2}$$

and anticommutation relations

$$\begin{aligned}\{\hat{w}_1^A, \hat{w}_2^A\} &= 0, \\ \{\hat{w}_1^B, \hat{w}_2^B\} &= 0.\end{aligned}$$

APPENDIX A. ENTANGLEMENT SPECTRUM

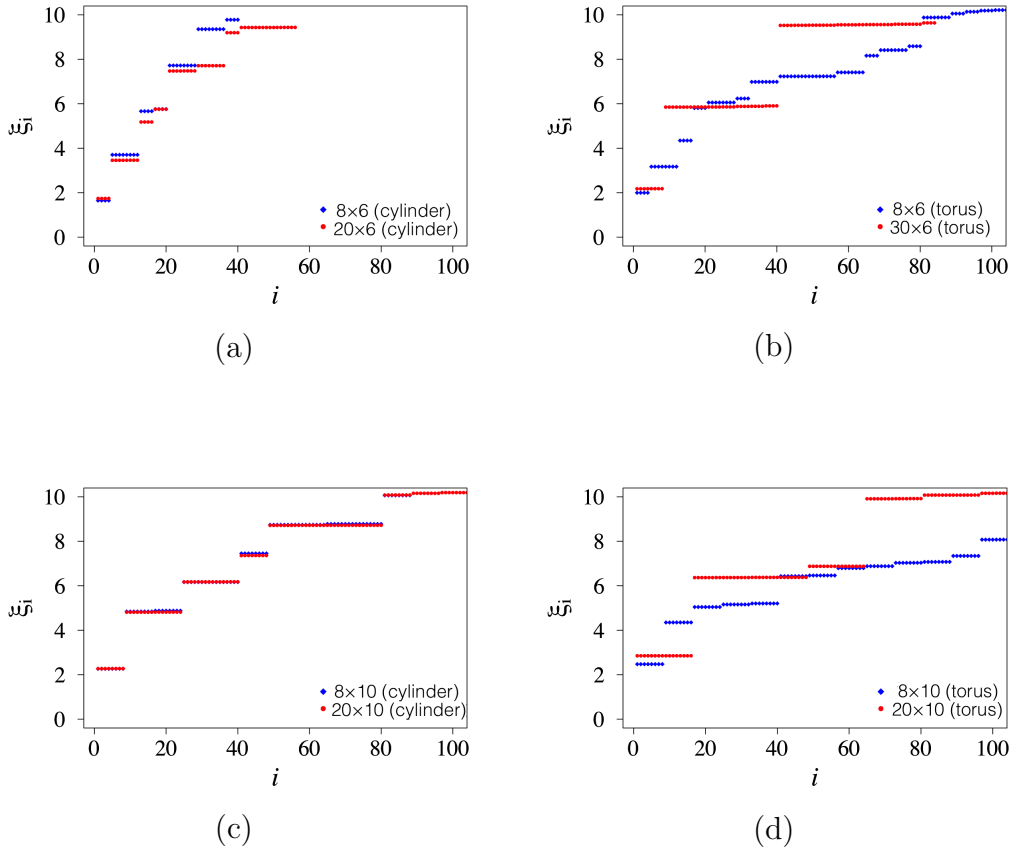


Figure A.3: The dependence of entanglement spectrum ξ_i of the Kitaev spin-liquid on system size and boundary condition. (a) 8×6 -site system (blue rhombuses) and 20×6 -site system (red circles) with cylindrical boundary condition, (b) 8×6 -site system (blue rhombuses) and 30×6 -site system (red circles) with toroidal boundary conditions, (c) 8×10 -site system (blue rhombuses) and 20×10 -site system (red circles) with cylindrical boundary conditions, and (d) 8×10 -site system (blue rhombuses) and 20×10 -site system (red circles) with toroidal boundary conditions.

APPENDIX A. ENTANGLEMENT SPECTRUM

The ground state is vortex free state, so that the ground state should be an eigenstate of \hat{W}_1 with eigenvalue +1:

$$\hat{W}_1|\psi\rangle = +|\psi\rangle.$$

The ground state can be written as

$$|\psi\rangle = |W_1 = +1\rangle \tag{A.3}$$

$$\begin{aligned} &= c_+ |w_1^A = +1, w_1^B = +1\rangle \\ &\quad + c_- |w_1^A = -1, w_1^B = -1\rangle, \end{aligned} \tag{A.4}$$

with

$$\hat{w}_1^{A,B} |w_1^{A,B} = \pm 1\rangle = \pm |w_1^{A,B} = \pm 1\rangle.$$

The eigenstates obey

$$\begin{aligned} \hat{w}_2^A |w_1^A = +1\rangle &= |w_1^A = -1\rangle, \\ \hat{w}_2^A |w_1^A = -1\rangle &= |w_1^A = +1\rangle. \end{aligned}$$

Furthermore, from Eq. (A.2), the ground state $|\psi\rangle$ is simultaneous eigenstate of W_1 and W_2 , so that $|\psi\rangle$ is also eigenstate of W_2 :

$$\begin{aligned} \hat{W}_2|\psi\rangle &= \hat{w}_2^A \hat{w}_2^B |W_1 = +1\rangle \\ &= c_+ \hat{w}_2^A \hat{w}_2^B |w_1^A = +1, w_1^B = +1\rangle \\ &\quad + c_- \hat{w}_2^A \hat{w}_2^B |w_1^A = -1, w_1^B = -1\rangle \\ &= c_+ |w_1^A = -1, w_1^B = -1\rangle \\ &\quad + c_- |w_1^A = +1, w_1^B = +1\rangle \\ &= + |\psi\rangle. \end{aligned} \tag{A.5}$$

Therefore, comparing Eq. (A.4) and Eq. (A.5), we obtain

$$c_+ = c_- \equiv c$$

and

$$|\psi\rangle = c (|w_1^A = +1, w_1^B = +1\rangle + |w_1^A = -1, w_1^B = -1\rangle).$$

APPENDIX A. ENTANGLEMENT SPECTRUM

The reduced density-matrix of subsystem A reads

$$\begin{aligned}
\rho_A &= \text{Tr}_B \rho = \text{Tr}_B |\psi\rangle\langle\psi| \\
&= \langle w_1^B = 1 | \rho | w_1^B = 1 \rangle + \langle w_1^B = -1 | \rho | w_1^B = -1 \rangle \\
&= c (|w_1^A = +1\rangle\langle w_1^A = +1| + |w_1^A = -1\rangle\langle w_1^A = -1|) \\
&= c \begin{pmatrix} 1 & 0 \\ 0 & 1 \end{pmatrix}
\end{aligned}$$

Therefore, we find that the eigenvalues of ρ_A , i.e., entanglement spectra, are 2-fold degenerate.

It is possible to define the third Wilson loop above W_2 , which shares the 24-25 (20-29) edge with W_1 (W_2) loop. However, the same procedure as (A.5) with respect to the third loop will give a result similar to the case of W_2 . This means no additional state for ρ_A , and thus the third loop does not contribute to increasing the number of degeneracy.

Next we consider a system with toroidal boundary condition in a similar way. In this case, we define additional Wilson loops W_3 and W_4 that are located on the pink line at the edge of Fig. A.2. These Wilson loops contribute to additional degeneracy of entanglement spectrum, resulting in 2^2 -fold degeneracy of entanglement spectrum. A similar result with this discussion has been obtained by Yao and Qi, [151] where the number of degeneracy of entanglement spectrum is 2^{L-1} with L being the length of boundary between the A and B subsystems.

Based on the discussion above, we expect that the number of degeneracy in a $L_x \times 10$ -site system is larger than that in a $L_x \times 6$ -site system, since the length of boundary between A and B is longer, i.e., the number of Wilson loops defined on honeycomb lattice is larger in the former than in the latter. We confirm this by our DMRG calculations as shown in Fig. A.3, were we keep 700 states in the DMRG block and performed more than 20 sweeps, resulting in truncation error 10^{-10} or smaller.

Blue rhombuses and red circles in Fig. A.3(a) show low entanglement levels for cylindrical 8×6 -site and 20×6 -site systems, respectively. We find that the levels are at least 4-fold degenerate. The results for the same system but with toroidal boundary condition are shown in Fig. A.3(b), where in contrast with cylindrical boundary condition, the number of degeneracy strongly depends on the system size along the x -axis direction: at least 4-fold degeneracy for 8×6 -site system and at least 8-fold degeneracy for 30×6 -site system. We also examined 12×6 -site and 20×6 -site systems and obtained the same result (not

APPENDIX A. ENTANGLEMENT SPECTRUM

shown). Therefore, we can conclude that 4-fold degeneracy for $L_x \times 6$ with cylindrical boundary condition and 8-fold with toroidal boundary condition as discussed above.

Next, we enlarge system along the y -axis direction. Blue rhombuses and red circles in Fig. A.3 (c) show low entanglement levels for cylindrical 8×10 -site and 20×10 -site systems, respectively. We find that the levels are at least 8-fold degenerate and thus the degeneracy is doubled as compared with $L_x \times 6$ -site system. The results for the same system but with toroidal boundary condition are shown in Fig. A.3(d), where in contrast with cylindrical boundary condition, the number of degeneracy strongly depends on the system size along the y -axis direction: at least 8-fold degeneracy for 8×10 -site system and at least 16-fold degeneracy for 20×10 -site system. Therefore, we can conclude that 8-fold degeneracy for $L_x \times 10$ with cylindrical boundary condition and 16-fold with toroidal boundary condition. All of these numerical results are consistent with an analytical ones mentioned above.

The ground state of the Kitaev spin-liquid state can be regarded as Majorana fermions coupled with \mathbb{Z}_2 gauge field. The gauge field is, thus, the origin of the degeneracy of entanglement spectrum. We note that such a gauge fluctuation also affects topological entanglement entropy [151].

Bibliography

- [1] A. Kitaev, Ann. Phys. (NY) **321**, 2 (2006).
- [2] G. Khaliullin, Prog. Theor. Phys. Suppl. **160**, 155 (2005).
- [3] G. Jackeli and G. Khaliullin, Phys. Rev. Lett. **102**, 017205 (2009).
- [4] J. Chaloupka, G. Jackeli, and G. Khaliullin, Phys. Rev. Lett. **105**, 027204 (2010).
- [5] H.-C. Jiang, Z.-C. Gu, X.-L. Qi, and S. Trebst, Phys. Rev. B **83**, 245104 (2011).
- [6] J. Reuther, R. Thomale, and S. Trebst, Phys. Rev. B **84**, 100406 (2011).
- [7] S. Okamoto, Phys. Rev. B **87**, 064508 (2013).
- [8] R. Schaffer, S. Bhattacharjee, and Y. B. Kim, Phys. Rev. B **86**, 224417 (2012).
- [9] J. Chaloupka, G. Jackeli, and G. Khaliullin, Phys. Rev. Lett. **110**, 097204 (2013).
- [10] C. Price and N. B. Perkins, Phys. Rev. B **88**, 024410 (2013).
- [11] E. Sela, H.-C. Jiang, M. H. Gerlach, and S. Trebst, Phys. Rev. B **90**, 035113 (2014).
- [12] F. Ye, S. Chi, H. Cao, B. C. Chakoumakos, J. A. Fernandez-Baca, R. Custelcean, T. F. Qi, O. B. Korneta, and G. Cao, Phys. Rev. B **85**, 180403 (2012).
- [13] S. K. Choi, R. Coldea, A. N. Kolmogorov, T. Lancaster, I. I. Mazin, S. J. Blundell, P. G. Radaelli, Y. Singh, P. Gegenwart, K. R. Choi, S.-W. Cheong, P. J. Baker, C. Stock, and J. Taylor, Phys. Rev. Lett. **108**, 127204 (2012).

BIBLIOGRAPHY

- [14] I. Kimchi and Y.-Z. You, Phys. Rev. B **84**, 180407 (2011).
- [15] A. F. Albuquerque, D. Schwandt, B. Hetényi, S. Capponi, M. Mambrini, and A. M. Läuchli, Phys. Rev. B **84**, 024406 (2011).
- [16] S. Bhattacharjee, S.-S. Lee, and Y. B Kim, New J. Phys. **14**, 073015 (2012).
- [17] J. Reuther, R. Thomale, and S. Rachel, Phys. Rev. B **90**, 100405(R) (2014).
- [18] Y. Yamaji, Y. Nomura, M. Kurita, R. Arita, and M. Imada, Phys. Rev. Lett. **113**, 107201 (2014).
- [19] J. G. Rau, E. K.-H. Lee, and H.-Y. Kee, Phys. Rev. Lett. **112**, 077204 (2014).
- [20] J. G. Rau and H.-Y. Kee, ArXiv e-prints (2014), arXiv:1408.4811 [cond-mat.str-el]
- [21] Y. Sizyuk, C. Price, P. Wölfle, and N. B. Perkins, Phys. Rev. B **90**, 155126 (2014).
- [22] I. Kimchi, R. Coldea, and A. Vishwanath, Phys. Rev. B **91**, 245134 (2015).
- [23] V. M. Katukuri, S. Nishimoto, V. Yushankhai, A. Stoyanova, H. Kandpal, S. Choi, R. Coldea, I. Rousochatzakis, L. Hozoi, and J. van den Brink, New J. Phys. **16**, 013056 (2014).
- [24] T. Suzuki, T. Yamada, Y. Yamaji, and S. Suga Phys. Rev. B **92**, 184411 (2015).
- [25] S. R. White, Phys. Rev. Lett. **69**, 2863 (1992).
- [26] I. Kimchi and A. Vishwanath, Phys. Rev. B **89**, 014414 (2014).
- [27] T. Dey, A. V. Mahajan, P. Khuntia, M. Baenitz, B. Koteswararao, and F. C. Chou, Phys. Rev. B **86**, 140405(R) (2012).
- [28] I. Rousochatzakis, U. K. Rssler, J. van den Brink, and M. Daghofer, ArXiv e-prints (2012), arXiv:1209.5895. [cond-mat.str-el].
- [29] M. Becker. M. Hermanns, Bela Bauer, M. Garst, and S. Trebst, Phys. Rev. B **91**, 155135 (2015).

BIBLIOGRAPHY

- [30] A. Catuneanu, J. G. Rau, H.-S. Kim, and H.-Y. Kee, Phys. Rev. B **92**, 165108 (2015).
- [31] K. Li, S.-L. Yu, and J.-X. Li, New J. Phys. **17**, 043032 (2015).
- [32] L. Balents, Nature **464**, 199 (2010).
- [33] S. Tomonaga, Prog. Theor. Phys. **5**, 544 (1950).
- [34] J. M. Luttinger, J. Math. Phys. **4**, 1154 (1963).
- [35] C. K. Majumdar and D. K. Ghosh, J. Math. Phys. **10**, 1399 (1969).
- [36] I. Affleck, T. Kennedy, E. H. Lieb, and H. Tasaki, Commun. Math. Phys. **115**, 477 (1988).
- [37] K. Okamoto and K. Nomura, Phys. Lett. A **169**, 433 (1992).
- [38] T. Momoi, J. Stat. Phys. **85**, 193 (1996).
- [39] H. Bethe, Z. Phys. **71**, 205 (1931).
- [40] A. Belavin, A.M. Polyakov, A. Zamolodchikov, Nucl. Phys. B, **241**, 333 (1984).
- [41] P. W. Anderson, Mater. Res. Bull. **8**, 153 (1973).
- [42] P. W. Anderson, Science **235**, 1196 (1987).
- [43] B. Bernu, C. Lhuillier, and L. Pierre, Phys. Rev. Lett. **69**, 2590 (1992).
- [44] L. Capriotti, A. E. Trumper, and S. Sorella, Phys. Rev. Lett. **82**, 3899 (1999).
- [45] V. Elser, Phys. Rev. Lett. **62**, 2405 (1989).
- [46] J. Chalker and J. Eastmond, Phys. Rev. B **46**, 14 201 (1992).
- [47] P. Leung and V. Elser, Phys. Rev. B **47**, 5459 (1993).
- [48] C. Zeng and V. Elser, Phys. Rev. B **51**, 8318 (1995).
- [49] P. Mendels, F. Bert, M. A. de Vries, A. Olariu, A. Harrison, F. Duc, J. C. Trombe, J. S. Lord, A. Amato, and C. Baines, Phys. Rev. Lett. **98**, 077204 (2007).

BIBLIOGRAPHY

- [50] J. S. Helton, K. Matan, M. P. Shores, E. A. Nytko, B. M. Bartlett, Y. Yoshida, Y. Takano, A. Suslov, Y. Qiu, J.-H. Chung, D. G. Nocera, and Y. S. Lee, Phys. Rev. Lett. **98**, 107204 (2007).
- [51] P. A. Lee, Science **321**, 136 (2008).
- [52] X.-G. Wen, “*Quantum Field Theory of Many-Body Systems*”, 1st ed. (Oxford University Press, Oxford, UK, 2004).
- [53] L. D. Landau, JETP **7**, pp. 1 (1937).
- [54] L. D. Landau, JETP **7**, pp. 627 (1937).
- [55] L. D. Landau and E. M. Lifshitz, *Statistical Physics Part 1*, 3rd ed. (Pergamon press, Oxford, England, 1975).
- [56] F. Verstraete and J. I. Cirac, ArXiv e-prints (2004), arXiv:0407066 [cond-mat.str-el].
- [57] J. Jordan, R. Orús, G. Vidal, F. Verstraete, and J. I. Cirac, Phys. Rev. Lett. **101**, 250602 (2008).
- [58] P. Corboz, S. R. White, G. Vidal, and M. Troyer, Phys. Rev. B **84**, 041108(R)(2011).
- [59] G. Vidal, Phys. Rev. Lett. **99**, 220405 (2007).
- [60] C. Nayak, S. H. Simon, A. Stern, M. Freedman, and S. Das Sarma, Rev. Mod. Phys. **80**, 1083 (2008).
- [61] J. K. Pachos, “*Introduction to Topological Quantum Computation*, Cambridge University Press, Cambridge (2012).
- [62] L. Hulthén, Arkiv. Mat. Astron. Fyzik 26A, No. 11 (1938).
- [63] L. Faddeev and L. Takhtajan, Phys. Lett. **85A**, 375 (1981).
- [64] M. Takahashi, J. Phys. C Solid State Phys. **10**, 1289 (1977).
- [65] A. H. MacDonald, S. M. Girvin, and D. Yoshioka, Phys. Rev. B **37**, 9753 (1988).
- [66] G. Misguich, C. Lhuillier, B. Bernu, and C. Waldtmann, Phys. Rev. B **60**, 1064 (1999).
- [67] W. LiMing, G. Misguich, P. Sindzingre, and C. Lhuillier, Phys. Rev. B **62**, 6372 (2000).

BIBLIOGRAPHY

- [68] Y. Shimizu, K. Miyagawa, K. Kanoda, M. Maesato, and G. Saito, Phys. Rev. Lett. **91**, 107001 (2003).
- [69] T. Itou, A. Oyamada, S. Maegawa, M. Tamura, and R. Kato, Phys. Rev. B **77**, 104413 (2008).
- [70] M. Yamashita, N. Nakata, Y. Kasahara, T. Sasaki, N. Yoneyama, N. Kobayashi, S. Fujimoto, T. Shibauchi, and Y. Matsuda, Nat. Phys. **5**, 44 (2009).
- [71] F. L. Pratt, P. J. Baker, S. J. Blundell, T. Lancaster, S. Ohira-Kawamura, C. Baines, Y. Shimizu, K. Kanoda, I. Watanabe, and G. Saito, Nature **471**, 612 (2011).
- [72] S. Yamashita, T. Yamamoto, Y. Nakazawa, M. Tamura, and R. Kato, Nat. Commun. **2**, 275 (2011).
- [73] D. Watanabe, M. Yamashita, S. Tonegawa, Y. Oshima, H.M. Yamamoto, R. Kato, I. Sheikin, K. Behnia, T. Terashima, S. Uji, T. Shibauchi, and Y. Matsuda, Nat. Commun. **3**, 1090 (2012).
- [74] S.-S. Lee, P. A. Lee, and T. Senthil, Phys. Rev. Lett. **98**, 067006 (2007).
- [75] S.-S. Lee, Phys. Rev. B **78**, 085129 (2008).
- [76] V. Kalmeyer and R. B. Laughlin, Phys. Rev. Lett. **59**, 2095 (1987).
- [77] S.-S. Gong, W. Zhu, and D. N. Sheng, Sci. Rep. **4**, 6317 (2014).
- [78] B. Bauer, L. Cincio, B. P. Keller, M. Dolfi, G. Vidal, S. Trebst, and A. W. W. Ludwig, Nat. Comms. **5**, 5137 (2014).
- [79] Y-C. He, S. Bhattacharjee, F. Pollmann, and R. Moessner, ArXiv e-prints (2015), arXiv:1509.03070 [cond-mat.str-el].
- [80] S. A. Kivelson, D. S. Rokhsar, and J. P. Sethna, Phys. Rev. B **35**, 8865(R) (1987).
- [81] D. S. Rokhsar and S. A. Kivelson, Phys. Rev. Lett. **61**, 2376 (1988).
- [82] J. Kogut and L. Susskind, Phys. Rev. D **11**, 395 (1975).
- [83] E. Fradkin and L. Susskind, Phys. Rev. D **17**, 2637 (1978).
- [84] R. Moessner, S. L. Sondhi, and E. Fradkin, Phys. Rev. B **65**, 024504 (2001).

BIBLIOGRAPHY

- [85] E. Fradkin, “*Field Theories of Condensed Matter Physics*”, Cambridge University Press, Cambridge (2013).
- [86] F. Wegner, J. Math. Phys. **12**, 2259 (1971).
- [87] G. Misguich, D. Serban, and V. Pasquier, Phys. Rev. Lett. **89**, 137202 (2002).
- [88] H.-C. Jiang, H. Yao, and L. Balents, Phys. Rev. B **86**, 024424 (2012).
- [89] Y. Wan and O. Tchernyshyov, Phys. Rev. B **87**, 104408 (2013).
- [90] H. Ju and L. Balents, Phys. Rev. B **87**, 195109 (2013).
- [91] A. Kitaev, Ann. Phys. **303** (2003).
- [92] J. Knolle, D. L. Kovrizhin, J. T. Chalker, and R. Moessner, Phys. Rev. Lett. **112**, 207203 (2014).
- [93] G. Baskaran, S. Mandal, and R. Shankar, Phys. Rev. Lett. **98**, 247201 (2007).
- [94] S. Y. ang, S.-J. Gu, C.-P. Sun, and H.-Q. Lin, Phys. Rev. A **78**, 012304 (2008).
- [95] W. Witczak-Krempa, G. Chen, Y. B. Kim, and L. Balents, Ann. Rev. Condensed Matter Phys. **5**, 57 (2014).
- [96] Y. Singh, S. Manni, J. Reuther, T. berlijn, R. Thomale, W. Ku, S. Trebst, and P. Gegenwart, Phys. Rev. Lett. **108**, 127203 (2012).
- [97] Y. Singh and P. Gegenwart, Phys. Rev. B **82**, 064412 (2010).
- [98] R. Comin, G. Levy, B. Ludbrook, Z.=h. Zhu, C. N. Veenstra, J. A. Rosen, Y. Singh, P. Gegenwart, D. Stricker, J. N. Hancodk, D. van der Marel, I. S. Elfimov, and A. Damascelli, Phys. Rev. Lett. **109**, 266406 (2012).
- [99] X. Liu, T. Berlijn, W.-G. Yin, W. Ku, A. Tsvelik, Y.-J. Kim, H. Gretaansson, Y. Singh, P. Gegenwart, and J. Hill, Phys. Rev. B **83**, 220403 (2011).
- [100] H. Grerarsson, J. P. Clancy, Y. Singh, P. Gegenwart, J. P. Hill, J. Kim, M. H. Upton, A. H. Said, D. Casa, T. Gog, and Y.-J. Kim, Phys. Rev. B **87**, 220407 (2013).

BIBLIOGRAPHY

- [101] H. Gretarsson, J. P. Clancy, X. Liu, J. P. Hill, E. Bozin, Y. Singh, S. Manni, P. Gegenwart, J. Kim, A. H. Said, D. Casa, T. Gog, M. H. Upton, H.-S. Kim, J. Yu, V. M. Katukuri, L. Hozoi, J. van den Brink, and Y.-J. Kim, Phys. Rev. Lett. **110**, 076402 (2013).
- [102] S. Manni, “*Synthesis and investigation of frustrated Honeycomb lattice iridates and rhodates*” (the Georg-August University, 2014)
- [103] I. Kimchi, R. Coldea, and A. Vishwanath, Phys. Rev. B **91**, 245134 (2015).
- [104] H.-S. Kim, V. Shanker V., A. Catuneanu, and H.-Y. Kee, Phys. Rev. B **91**, 241110(R) (2015).
- [105] J. A. Sears, M. Songvilay, K. W. Plumb, J. P. Clancy, Y. Qiu, Y. Zhao, D. Parshall, and Y.-J. Kim, Phys. Rev. B **91**, 144420 (2015).
- [106] S. Manni, Y. Tokiwa, and P. Gegenwart, Phys. Rev. B **89**, 241102(R) (2014).
- [107] Z. Nussinov and J. van den Brink, ArXiv e-prints (2013), arXiv:1303.5922 [cond-mat.str-el]; Z. Nussinov, and J. van den Brink, Rev. Mod. Phys. **87**, 1 (2015).
- [108] G. Jackeli and A. Avella, Phys. Rev. B **92**, 184416 (2015).
- [109] H. Kawamura and S. Miyashita, J. Phys. Soc. Jpn. **53**, 4138 (1984).
- [110] V. L. Berezinskii, Sov. Phys. JETP **32**, 493 (1971).
- [111] J M Kosterlitz and D J Thouless, J. Phys. C Solid State Phys. **6**, 1181 (1973).
- [112] K. Momma and F. Izumi, Commission on Crystallogr. Comput., IUCr Newslett., No. 7 (2006) 106-119.
- [113] U. Schollwöck, Rev. Mod. Phys. **77**, 259 (2005).
- [114] B. Zeng, X. Chen, D.-L. Zhou, X.-G. Wen, ArXiv e-prints (2015), arXiv:1508.02595 [cond-mat.str-el].
- [115] A. Einstein, B. Podolsky, and N Rosen, Phys. Rev. **47**, 777 (1935).
- [116] M. Nielsen and I. Chuang, “*Quantum computation and quantum information*”, Cambridge University Press, Cambridge (2000).

BIBLIOGRAPHY

- [117] C. Holzhey, F. Larsen, and F. Wilczek, Nucl. Phys. B **424**, 443 (1994).
- [118] P. Calabrese and J. Cardy, J. Stat. Mech. P06002 (2004).
- [119] L. Bombelli, R. K. Koul, J. H. Lee, and R. D. Sorkin, Phys. Rev. D **34**, 373 (1986).
- [120] M. Srednicki, Phys. Rev. Lett. **71**, 666 (1993).
- [121] S. Ryu and T. Takayanagi, Phys. Rev. Lett. **96**, 181602 (2006).
- [122] S. Ryu and T. Takayanagi, J. High Energy Phys. **0608**, 045 (2006).
- [123] J. I. Latorre, and A. Riera, J. Phys. A **42**, 504002 (2009).
- [124] T. Nishioka, S. Ryu, and T. Takayanagi, J. Phys. A **42**, 504008 (2009).
- [125] J. Eisert, M. Cramer, and M. B. Plenio, Rev. Mod. Phys. **82**, 277 (2010).
- [126] T. Takayanagi, Class. Quant. Grav. **29**, 153001 (2012).
- [127] H. B. Hastings, J. Stat. Mech. P08024 (2007).
- [128] M. Levin and X.-G. Wen, Phys. Rev. Lett. **96**, 110405 (2006).
- [129] A. Kitaev and J. Preskill, Phys. Rev. Lett. **96**, 110404 (2006).
- [130] R. Orús, Ann. Phys. **349**, 117 (2014).
- [131] G. Vidal, J. I. Latorre, E. Rico, and A. Kitaev, Phys. Rev. Lett. **90**, 227902 (2003).
- [132] M. M. Wolf, Phys. Rev. Lett. **96**, 010404 (2006).
- [133] D. Gioev and I. Klich, Phys. Rev. Lett. **96**, 100503 (2006).
- [134] T. Barthel, M.-C. Chung, and U. Schollw'ock, Phys. Rev. A **74**, 022329 (2006).
- [135] M. Cramer, J. Eisert, and M. B. Plenio, Phys. Rev. Lett. **98**, 220603 (2007).
- [136] B. Hsu, M. Mulligan, E. Fradkin and E.-A Kim, Phys. Rev. B **79**, 115421 (2009).
- [137] J.-M. Stéphan, S. Furukawa, G. Misguich and V. Pasquier, Phys. Rev. B **80**, 184421 (2009).

BIBLIOGRAPHY

- [138] M. P. Zaletel, J. H. Bardarson and J. E. Moore, Phys. Rev. Lett. **107**, 020402 (2011).
- [139] J.-M. Stéphan, G. Misguich and V. Pasquier, Phys. Rev. B **84**, 195127 (2011).
- [140] J.-M Stéphan, H. Ju, P. Fendley and R. G. Melko, New. J. Phys. **15**, 015004 (2013).
- [141] H. Ju, A. B. Kallin, P. Fendley, M. B. Hastings and R. G. Melko, Phys. Rev. B **85**, 165121 (2012).
- [142] L. Tagliacozzo G. Evenbly and G. Vidal, Phys. Rev. B **80**, 235127 (2009).
- [143] M. A. Metlitski, C. A. Fuertes and S. Sachdev, Phys. Rev. B **80**, 115122 (2009).
- [144] H. Li and F. D. M. Haldane, Phys. Rev. Lett. **101**, 010504 (2008).
- [145] N. Regnault, B. A. Bernevig, and F. D. M. Haldane, Phys. Rev. Lett. **103**, 016801 (2009).
- [146] A. M. Läuchli, E. J. Bergholtz, J. Suorsa, and M. Haque, Phys. Rev. Lett. **104**, 156404 (2010).
- [147] R. Thomale, A. Sterdyniak, N. Regnault, and B. A. Bernevig, Phys. Rev. Lett. **104**, 180502 (2010).
- [148] A. M. Turner, Y. Zhang, and A. Vishwanath, Phys. Rev. B **82**, 241102 2010.
- [149] L. Fidkowski, Phys. Rev. Lett. **104**, 130502 (2010).
- [150] R. Thomale, D. P. Arovas, and B. A. Bernevig, Phys. Rev. Lett. **105**, 116805 (2010).
- [151] H. Yao and X.-L Qi, Phys. Rev. Lett. **105**, 080501 (2010).
- [152] R. Lundgren, V. Chua, and G. A. Fiete, Phys. Rev. B **86**, 224422 (2012).
- [153] L. Lepori, G. De Chiara, and A. Sanpera, Phys. Rev. B **87**, 235107 (2013).
- [154] S. M. Giampaolo, S. Montangero, F. Dell'Anno, S. De Siena, and F. Illuminati, Phys. Rev. B **88**, 125142 (2013).

BIBLIOGRAPHY

- [155] A. J. A. James and R. M. Konik, Phys. Rev. B **87**, 241103 (2013).
- [156] M. Moreno-Cardoner, S. Paganelli, G. De Chiara, and A. Sanpera, J. Stat. Mech. P10008 (2014).
- [157] A. Chandran, V. Khemani, and S. L. Sondhi, Phys. Rev. Lett. **113**, 060501 (2014).
- [158] S. Furukawa, G. Misguich, and M. Oshikawa, Phys. Rev. Lett. **96**, 047211 (2006).
- [159] C. L. Henley and H. J. Changlani, J. Stat. Mech. P11002 (2014).
- [160] S. Morita, private communications.